Characterization of
2D Antimony Lattices

Dissertation zur Erlangung des
naturwissenschaftlichen Doktorgrades
der Julius-Maximilians-Universität Würzburg

vorgelegt von

Tim Matthias Wagner

aus Groß-Umstadt

Würzburg 2023

Eingereicht am:

bei der Fakultät für Physik und Astronomie

1. Gutachter: Prof. Dr. Jörg Schäfer

2. Gutachter: Prof. Dr. Friedrich Reinert

3. Gutachter:

der Dissertation

Vorsitzende(r):

1. Prüfer: Prof. Dr. Jörg Schäfer

2. Prüfer: Prof. Dr. Friedrich Reinert

3. Prüfer:

im Promotionskolloquium

Tag des Promotionskolloquiums:

Doktorurkunde ausgehändigt:

Abstract

Two-dimensional lattices are in the focus of research in modern solid state physics due to their novel and exotic electronic properties with tremendous potential for seminal future applications. Of particular interest within this research field are quantum spin Hall insulators which are characterized by an insulating bulk with symmetry-protected metallic edge states. For electrons within these one-dimensional conducting channels, spin-momentum locking enables dissipationless transport - a property which promises nothing short of a revolution for electronic devices. So far, however, quantum spin Hall materials require enormous efforts to be realized such as cryogenic temperatures or ultra-high vacuum. A potential candidate to overcome these shortcomings are two-dimensional lattices of the topological semi-metal antimony due to their potential to host the quantum spin Hall effect while offering improved resilience against oxidation.

In this work, two-dimensional lattices of antimony on different substrates, namely Ag(111), InSb(111) and SiC(0001), are investigated regarding their atomic structure and electronic properties with complimentary surface sensitive techniques. In addition, a systematic oxidation study compares the stability of Sb-SiC(0001) with that of the two-dimensional topological insulators bismuthene-SiC(0001) and indenene-SiC(0001).

A comprehensive experimental analysis of the $(\sqrt{3} \times \sqrt{3})R30°$ Sb-Ag(111) surface, including X-ray standing wave measurements, disproves the proclaimed formation of a buckled antimonene lattice in literature. The surface lattice can instead be identified as a metallic Ag_2Sb surface alloy.

Antimony on InSb(111) shows an unstrained Volmer-Weber island growth due to its large lattice mismatch to the substrate. The concomitant moiré situation at the interface imprints mainly in a periodic height corrugation of the antimony islands which as observed with scanning tunneling microscopy. On islands with various thicknesses, quasiparticle interference patterns allow to trace the topological surface state of antimony down to the few-layer limit.

On SiC(0001), two different two-dimensional antimony surface reconstructions are identi-

fied. Firstly, a metallic triangular 1×1 lattice which constitutes the antimony analogue to the topological insulator indenene. Secondly, an insulating asymmetric kagome lattice which represents the very first realized atomic surface kagome lattice.

A comparative, systematic oxidation study of elemental (sub-)monolayer materials on SiC(0001) reveals a high sensitivity of indenene and bismuthene to small dosages of oxygen. An improved resilience is found for Sb-SiC(0001) which, however, oxidizes nevertheless if exposed to oxygen. These surface lattices are therefore not suitable for future applications without additional protective measures.

Zusammenfassung

Zweidimensionale Kristallgitter sind aufgrund ihrer neuartigen, exotischen elektronischen Eigenschaften ein hochaktuelles Thema der modernen Festkörperphysik mit enormen Potential für bahnbrechende zukünftige Anwendungen. Die Klasse der Quanten-Spin-Hall-Isolatoren erfährt in diesem Zusammenhang besondere Aufmerksamkeit in der aktuellen Forschung aufgrund ihrer durch Symmetrie geschützten, metallischen Randkanäle. In diesen ermöglicht das sogenannte "spin-momentum locking" der Elektronen einen verlustfreien Ladungstransport - eine Eigenschaft, die nichts weniger als eine Revolution auf dem Gebiet der Elektronik verspricht. Bisher konnten Quanten-Spin-Hall-Isolatoren allerdings nur unter enormem Aufwand bei kryogenen Temperaturen oder im Ultrahochvakuum realisiert werden. Eine Materialkandidat welcher es ermöglichen könnte diese Unzulänglichkeiten zu überwinden, sind zweidimensionale Gitter des topologischen Halbmetalls Antimon. Diese zeigen zum einen eine erhöhte Widerstandsfähigkeit gegen Oxidation und gelten zum anderen als potentielle Kandidaten für die Realisierung eben jenes Quanten-Spin-Hall-Effekts.

Im Rahmen dieser Arbeit werden zweidimensionale Antimongitter auf unterschiedlichen Substraten, nämlich Ag(111), InSb(111) und SiC(0001), mit komplementären oberflächensensitiven Messmethoden hinsichtlich ihrer atomaren Struktur und elektronischen Eigenschaften untersucht. Zusätzlich wird mittels einer systematischen Oxidationsstudie die Stabilität von Sb-SiC(0001) mit derjenigen der topologischen Isolatoren Bismuthene-SiC(0001) und Indenene-SiC(0001) verglichen.

Eine umfängliche experimentelle Analyse der $(\sqrt{3}\times\sqrt{3})R30°$ Sb-Ag(111) Oberfläche, inklusive stehenden Röntgenwellenfeldern, widerlegt die in der Literatur beschriebene Ausbildung eines gefalteten Antimonene-Gitters. Die Oberflächenstruktur kann stattdessen als metallische Ag_2Sb Oberflächenlegierung identifiziert werden.

Auf InSb(111) zeigt Antimon, bedingt durch den großen Unterschied in der Gitterkonstante, ein unverzerrtes Volmer-Weber Inselwachstum. Die damit einhergehende Moiré Situation an der Grenzfläche spiegelt sich dabei in einer periodischen Wellung der Ober-

fläche wieder. Auf Antimon-Inseln unterschiedlicher Dicke kann der topologische Oberflächenzustand mittels Quasi-Teilchen-Interferenzmustern bis hinab auf Schichtdicken von wenigen Atomlagen beobachtet werden.

Auf SiC(0001) können zwei unterschiedliche zweidimensionale Oberflächenrekonstruktionen von Antimon identifiziert werden. Zum einen ein metallisches 1×1 Dreiecksgitter, dem Antimon-Analogon zum topologischen Isolator Indenene. Zum anderen ein isolierendes asymme-trisches Antimon Kagomegitter - das Erste jemals hergestellte atomare Oberflächengitter mit Kagome-Struktur.

Eine vergleichende systematische Oxydationsstudie von elementaren (Sub-)Monolagenmaterialien auf SiC(0001) zeigt eine hohe Anfälligkeit von Indenene und Bismuthene gegenüber selbst kleinen Dosen an Sauerstoff. Sb-SiC(0001) zeigt eine deutlich stärkere Oxidationsresistenz, oxidiert aber ebenfalls in Kontakt mit Sauerstoff. Die untersuchten Oberflächengitter sind somit ohne zusätzliche Schutzmaßnahmen nicht für zukünftige Anwendungen nutzbar.

Contents

Acronyms

1D one-dimensional

2D two-dimensional

3D three-dimensional

ARPES angle-resolved photoemission spectroscopy

BL bilayer

CEC constant energy contour

DFT density functional theory

DOS density of states

EDC energy distribution curve

GGA generalized gradient approximation

hBN hexagonal boron nitride

IMFP inelastic mean free path

ISB inversion symmetry breaking

LDA local density approximation

LDOS local density of states

LEED low-energy electron diffraction

MBE molecular beam epitaxy

MDC momentum distribution curve

ML monolayer

PBE Perdew-Burke-Ernzerhof

PES photoemission spectroscopy

QAHE quantum anomalous hall effect

QPI quasiparticle interference

QSHE quantum spin hall effect

RT room temperature

SOC spin-orbit coupling

STEM scanning transmission electron microscy

STM scanning tunneling microscopy

STS Scanning tunneling spectroscopy

TI topological insulator

TMDC transition-metal dichalcogenide

TRS time reversal symmetry

TTC tetratetracontane

UHV ultra-high vacuum

XPS X-ray photoelectron spectroscopy

XSW X-ray standing waves

1 Motivation

Since the discovery of graphene in 2004 [1], two-dimensional (2D) materials have been in the focus of research among solid state physicists. The structural confinement of these materials in one dimension strongly alters their physical characteristics compared to their three-dimensional (3D) bulk counterparts giving rise to improved electrical, optical and mechanical properties [2, 3]. Today, a plethora of 2D materials are available ranging from insulators via semiconductors to (semi-)metals such as hexagonal boron nitride (hBN) [4,5], metal oxides [6], transition-metal dichalcogenides (TMDCs) [7,8], black phosphorus [9,10] or mono-elemental compounds (X-enes) [11–13] with potential for versatile applications in the fields of catalysis, optoelectronics or sensors [14]. For fundamental research, 2D materials additionally provide unprecedented possibilities to experimentally explore exotic states of matter, e.g., the quantum spin hall effect (QSHE) [13, 15], quantum anomalous hall effect (QAHE) [16], magneto-electric multiferroics [17] or superconductivity [18].

Besides representing the dawn of 2D materials, graphene was classified in 2005 as a 2D topological insulator (TI) by Kane and Melee [19,20] which, up to that time, represented an unknown state of matter. 2D topological insulators are characterized by an insulating bulk with metallic one-dimensional (1D) edge states if in contact with a trivial insulator [21]. The metallic edges states thereby arise du to a band inversion between topological trivial and non-trivial materials driven by spin-orbit coupling which is resolved at their interface [22], see figure 1.1 a). For electrons propagating inside those 1D channels, the direction of movement is coupled to their spin, as depicted in figure 1.1 b). This so-called *spin-momentum locking* prevents backwards scattering of the electrons as long as time reversal symmetry (TRS) is preserved and thus allows dissipationless, spin-polarized transport with tremendous potential for groundbreaking applications [23]. Graphene itself, however, is no good candidate for the utilization of topological properties as its transport properties are dominated by trivial bulk electrons due to a zero band gap.

To enlarge the topological band gap in a graphene-like hexagonal monolayer lattice, it
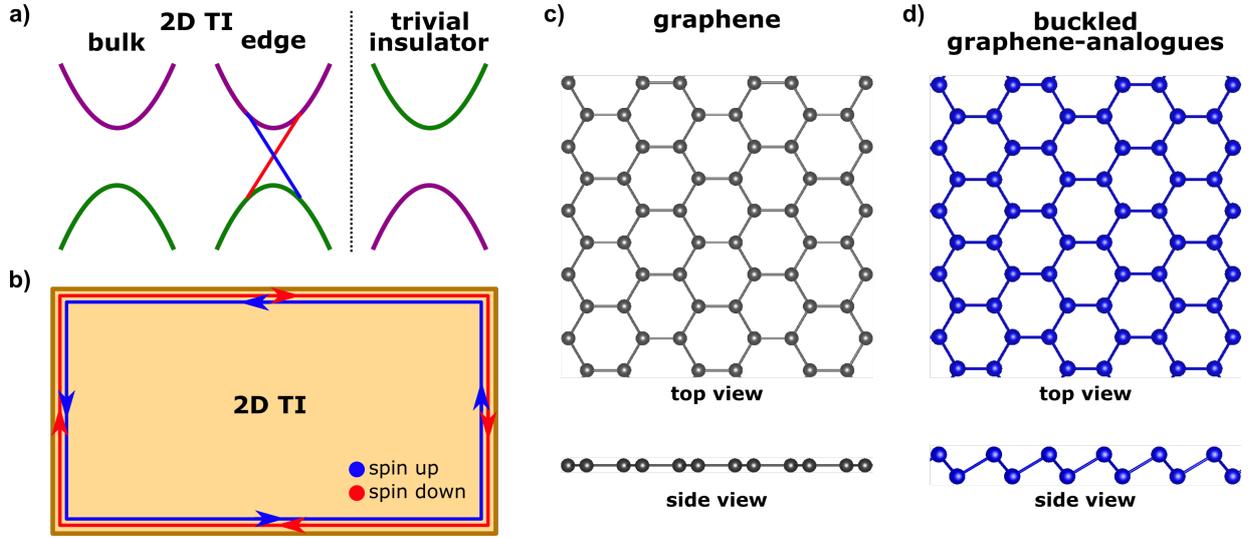
Figure 1.1: a) *Schematic depiction of the band inversion between a trivial and topological insulator and the gapless state at the edge of the TI. b) Due to spin-momentum locking, electrons with opposite spin counter-propagate along the edge of a 2D-TI. c) and d) Atomic models [24] of the flat hexagonal lattice of graphene and the buckled lattice of graphene-analogues of group 14 and 15 elements, respectively.*

requires an increased spin-orbit coupling strength which is naturally provided by heavier elements. For this reason, mono-elemental hexagonal lattices of various elements have been in the focus of extensive research. With the synthesis of plumbene in 2019 [12], all graphene-analogues of group 14 (Si [11], Ge [25], Sn [26], Pb [12]) have been experimentally realized. Albeit isoelectronic to graphene, the structure of their hexagonal lattices are not atomically flat, as it is the case for graphene, but atomically buckled due to larger interatomic distances within their lattices [27], as depicted in figure 1.1 c) and d). Nevertheless, all of them are predicted to be 2D TIs with bulk band gaps that increase with atomic mass up to 200 meV[1] [28, 29]. 2D hexagonal monolayer lattices have additionally been synthesized of group 15 elements ranging from blue phosphorus [30] over arsenene [31] and antimonene [32] to the experimentally proven 2D TI bismuthene [13, 33]. The large topological band gap of 0.8 eV around the Fermi level renders bismuthene an ideal candidate for applications at room temperature (RT) but its lattice lacks stability under ambient conditions [34]. A 2D topological insulator with robust properties for device applications has therefore yet to be found.

In recent years, the synthesis of hexagonal mono- to few layer antimonene was of particular interest [32, 35–42] due to strongly tunable optical, electronic and topological properties [43]

---

[1]plumbene requires electron doping to be topological non-trivial

as well as an excellent stability under atmospheric conditions [38,39]. In combination, these properties make this material class a promising candidate for future device applications. For fundamental research it is of particular interest to investigate the topological properties of mono- to few layer antimonene as antimony is predicted to show various phase transition under tensile strain [44–46] or with reduced thickness [47]. Bulk antimony itself is a topological semi-metal with 2D surface states at its (111) surface that coexist with carriers of the semi-metallic bulk. According to density functional theory (DFT) calculations [47], a global bulk band gap opens up in antimony if the thickness of an Sb(111) crystal is reduced below a thickness of 7.8 nm, rendering the material a 3D TI. Further reducing the thickness below 2.7 nm ($\leq$ 8 bilayer (BL)), enables the coupling of surface states from opposing sides of the crystalline film. This drives another transition to a quantum spin Hall phase with a surface state gap that increases up to about 45 meV. Below 4 BLs, antimony is expected to become a simple trivial insulator. Besides those thickness-dependent phase transitions, a free-standing insulating single hexagonal layer of Sb atoms is predicted to become a 2D TI under tensile strain [44–46]. The critical unit cell size for this transition is predicted to be in the range of 4.5 Å to 4.7 Å, an increase of 4.6% to 9.3% relative to the antimony bulk lattice.

So far, the synthesis of mono- to few layer antimonene has been reported on a variety of substrates including metals (Ag(111) [41, 42, 48], Cu(111) [49]), semiconductors (Bi-modified Si(111) [35], Ge(111) [40]) and 3D TIs (e.g., Bi_2Se_3 [36], Bi_2Te_3 [32]) by means of exfoliation techniques or molecular beam epitaxy (MBE). The presence of a substrate, however, intrinsically alters the electronic properties theoretically predicted for free-standing lattices due to inversion symmetry breaking, the chemical interaction at the interface or by proximity effects [37,50]. Metallic substrates additionally shortcut potential edge states and prevent their utilization. Regarding future applications, an adequate semiconducting substrate for antimonene that preserves or even enhances its topological properties, as observed for bismuthene on SiC(0001) [51], has yet to be found.

The main scope of this work is to investigate the structural and electronic properties of novel and established Sb lattices of mono- to few-layer thicknesses on different substrates, namely Ag(111), InSb(111)A and SiC(0001). This includes a comparative analysis on the stability of Sb-SiC(0001) and the related group 15 materials indenene/SiC(0001) and bismuthene/SiC(0001) under oxygen exposure.

Chapter 2 introduces the main experimental and theoretical methods used for sample analysis within this work. In chapter 3 to 5, 2D surface lattices of antimony on various substrates are analyzed regarding their structural and electronic properties. Firstly, chapter 3 focuses on the metallic Ag(111) substrate and resolves a discrepancy in literature about the structural properties of the Sb-induced surface. Secondly, chapter 4 highlights the unstrained growth of Sb layers with various thicknesses on InSb(111)A featuring an unusual moiré situation at the interface. Thirdly, chapter 5 introduces two novel Sb surface reconstructions on SiC, a triangular Sb-(1×1) and an asymmetric surface kagome lattice. At last, elemental 2D materials of Sb, Bi and In on SiC(0001) are investigated regarding their structural stability during oxygen exposure in chapter 6.

2 Experimental Methods

Surface sensitive analysis techniques are - as their name already suggests - predominantly probing the surface layers of a material. They are therefore well-suited for the investigation of 2D materials grown on single crystal substrates, the main scope of this thesis. This chapter will give a brief overview over the main techniques used for data acquisition, namely scanning tunneling microscopy (STM), photoemission spectroscopy (PES) and low-energy electron diffraction (LEED). The last section summarizes the concept of density functional theory, a first principles technique that allows to theoretically investigate the electronic structure of many-body systems. With exhaustive literature available for each of these techniques, only basic concepts are introduced.

2.1 Scanning Tunneling Microscopy and Spectroscopy

First STM measurements were performed 1982 by its inventors Binnig and Rohrer [52] on $CaIrSn_4$(110) and Au(110). They demonstrated that is possible to obtain atomically resolved images of an electrically conductive surface by scanning a pointy metallic probe closely spaced to the sample. This invention drastically improved the capability of sample characterization on atomic length scales and was awarded with the Nobel Prize in 1986.

2.1.1 Basic principle and theoretical description

To obtain images with a sublime resolution, the STM utilizes the quantum mechanical tunneling effect of electrons through a potential barrier. A constant bias is applied between probe and sample which generates a tunneling current if the distance between both components is small enough, schematically depicted in figure 2.1. In 1D, the transmission

coefficient T of an electron with mass m_e through a potential barrier with an effective height Φ and width s can be expressed as [53]

$$T \propto exp(-2\chi s) \qquad \text{with} \qquad \chi = \frac{1}{\hbar}\sqrt{2m_e\Phi}. \tag{2.1}$$

The exponential dependence of the transmission coefficient on the barrier width s allows to perceive height differences of the investigated surface in picometer resolution [54]. Laterally, a sub-nanometer resolution is obtained by employing an atomically sharp tip in combination with high-precision piezoelectric elements for the scanning motion [55]. For image acquisition, an STM can be operated in two different modes. In *constant current mode*, the tunneling current is stabilized at a certain setpoint by a feedback loop that adjusts the probe-sample distance. In this case, the signal is extracted from the feedback-controlled z-movement of the respective piezoelectric element. In *constant height mode*, the tip is scanned parallel to the surface while the variation of the tunneling current contains information about the surface topography.
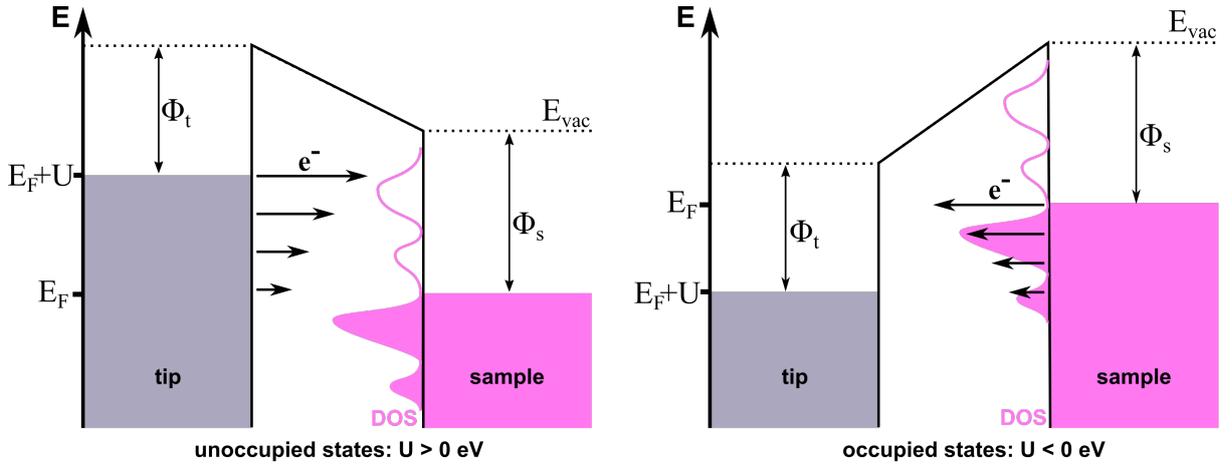
Figure 2.1: *Schematic depictions of the tunneling processes of a STM for positive (a) and negative (b) tunneling bias under the assumption of a constant density of states of the tip. The arrow length illustrates energy-dependent contributions to the tunneling current. Reproduced from [56]. Used with permission of Annual Reviews, Inc., 2022, permission conveyed through Copyright Clearance Center, Inc..*

Following a generalized Tersoff and Hamann model for a finite tunneling bias U and neglecting bias-distorted wave functions of tip and sample, the tunneling current I can be expressed as

$$I \propto \int_0^{eU} n_t(\pm eU \mp E)n_x(E)T(E, eU)dE \tag{2.2}$$

with the density of states (DOS) n_t and n_s of tip and sample, respectively [53]. The energy- and bias-dependent transmission coefficient $T(E, eU)$ is thereby given by

$$T(E, eU) = exp \left\{ -2d \left[\frac{2m_e}{\hbar^2} \left(\frac{\Phi_t + \Phi_s}{2} + \frac{eU}{2} - E \right) \right]^{\frac{1}{2}} \right\} \qquad (2.3)$$

with the tip-sample separation d and the work functions Φ_t and Φ_s for tip and sample, respectively. For a positive bias $U > 0$ eV, the transmission coefficient is largest at $E = eU$ and the tunneling current thus dominated by the DOS of the sample $n_s(eU)$ at the chosen tunneling bias, assuming a constant n_t. For $U < 0$ eV, the transmission maximum is always at $E = E_F$ and the tunneling current therefore less sensitive to $n_s(eU)$. This energy-dependence of the tunneling current is additionally indicated by the arrows shown in figure 2.1. Due to the dependence of the tunneling current on the DOS of the sample n_s, STM images do not solely depict the topography of the surface but rather a combination of structural and electronic properties. In experiment, this often exacerbates to determine unambiguous root causes for unknown features, e.g., if a protrusion is caused by the presence of an atom or simply due to high local density of states (LDOS).

2.1.2 Scanning Tunneling Spectroscopy

Scanning tunneling spectroscopy (STS) can be used to disentangle topographic and electronic features by selectively probing the LDOS of the sample. Under the assumption of an energy-independent DOS of the tip $n_t = const.$, which is justified after a proper preparation of the tip on a reference sample, the derivation of equation 2.3 gives

$$\frac{dI}{dU}(U) \propto e n_t(0) n_s(eU) T(eU, eU) + \int_0^{eU} n_t(\pm eU \mp E) n_s(E) \frac{dT(E, eU)}{dU} dE. \qquad (2.4)$$

Due to a smooth and monotonic energy dependence of the transmission coefficient [53], all structures apparent in the differential conductivity dI/dU can be attributed to variations in the LDOS of the sample

$$\frac{dI}{dU}(U) \propto n_s(eU). \qquad (2.5)$$

Experimentally, the differential conductivity is typically obtained via a Lock-in method. For this, a small sinusoidal voltage ΔU is modulated on top of the constant tunneling bias U_T at a frequency above the cut-off frequency of the feedback loop. The high frequency

bias signal generates a periodic modulation of the tunneling current which can be detected via the Lock-in amplifier. In first order, it can be expressed in a Taylor expansion around U_T as

$$I(U_T + U_{mod}sin(\omega t)) \propto \int_0^{e(U_T + U_{mod}sin(\omega t))} n_s(E)dE$$
$$\approx \underbrace{\int_0^{eU_T} n_s(E)dE}_{I(U_T)} + \underbrace{\frac{dI(U)}{dU}\bigg|_{U_T} U_{mod} \cdot sin(\omega t)}_{\Delta I} \quad (2.6)$$

The amplitude of the sinusoidal variation of the tunneling current ΔI is proportional to the differential conductivity and thus allows to directly access information about the LDOS structure of the sample.

2.1.3 STM Instrumentation

Within this work, all STM and STS results were obtained at a temperature of 4 K with a commercially available LT-STM from Omicron NanoTechnology GmbH in combination with an attached lock-in amplifier from SRS, if not stated otherwise. The instrument was attached to a ultra-high vacuum (UHV) chamber with a base pressure $< 5 \cdot 10^{-11}$ mbar and an attached load lock enabling *in-situ* transfers to other UHV setups.

2.2 Photoelectron Spectroscopy

The beginnings of photoelectron spectroscopy date back to the end of the 19th century with first observations of the photoelectric effect by Hertz [57] and Hallwachs [58] that were later explained by Albert Einstein in 1905 [59]. Nowadays, PES is a widely used technique in condensed matter physics in order to study the electronic properties of solids and surfaces. PES utilizes that excited photoelectrons carry information about their initial state inside the solid which can be extracted experimentally by measuring their momentum and energy distribution. Among a plethora of applications, angle-resolved photoemission spectroscopy (ARPES) and X-ray photoelectron spectroscopy (XPS) are most common and enable the investigation of momentum-resolved valence band states and material-characteristic core level information, respectively. Due to the finite beam spot of light sources, PES is considered a spatially averaging measurement technique.

2.2.1 Photoelectric effect

The photoelectric effect is based on the interaction of light with electrons insides a solid. A photon thereby transfers its energy $h\nu$ to an electron and ejects it from the solid. The maximum kinetic energy of the escaping electrons is given by the simple relation

$$E_{kin,max} = h\nu - \Phi_0 \tag{2.7}$$

with the work function of the solid Φ_0 [59]. Electrons with finite binding energy E_B below the Fermi level of the solid additionally require an equivalent amount of energy to escape and therefore have a lower kinetic energy. The photoelectric process can be schematically depicted as it is done in figure 2.2 a). Simply spoken, the energy distribution of the photoelectrons represents the eigenstates of the electrons inside the solid.

A common, yet simplified, description of photoelectron excitation is the so-called three-step model. It separates the entire process into steps that can be considered separately [60]:

   i) Excitation of the photoelectron

  ii) Transport of the photoelectron to the surface

 iii) Escape of the photoelectron from the surface

Excitation of the photoelectron

The transition probability between the initial (Ψ_i^N) and final (Ψ_f^N) N-particle state of an electron for a small perturbation H_{per} is given by Fermi's Golden rule

$$\omega \propto \frac{2\pi}{\hbar} |\langle \Psi_f^N | H_{per} | \Psi_i^N \rangle|^2 \cdot \delta(E_f^N - E_i^N - h\nu). \tag{2.8}$$

where energy conservation is ensured by the delta function taking into account initial and final state energies $E_{i/f}^N$ and the photon energy $h\nu$. If two photon processes are neglected $(\vec{A}^2 \to 0)$ and the translational symmetry of the solid is taken into account $(\vec{\nabla}\vec{A} = 0)$, the perturbation can be expressed as

$$H_{per} = \frac{e}{mc}\vec{A}\vec{p} \tag{2.9}$$

with the vector potential $\vec{A}$ of the photon and the momentum $\vec{p}$ of the electron. The initial and final state of the system can be factorized if one assumes (Ψ_i^N) to be a single Slater
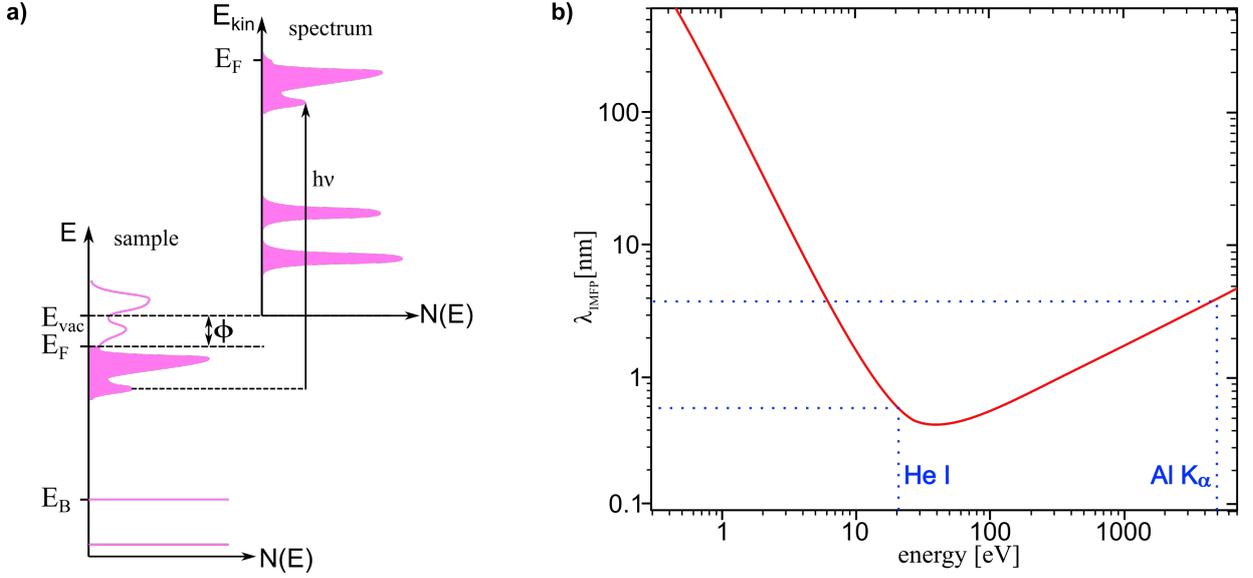
Figure 2.2: a) *Energetic depiction of the photoemission process with photons of energy $h\nu$. The energy-resolved measurement depicts the distribution of eigenstates of the electrons in the sample. Reproduced with permission from SNCSC [60]. b) Universal curve of the mean free path of electrons within a solid. Reproduced with permission from [61]. Copyright ©1979 Heyden & Son Ltd*

determinant and the photoemission process to be *sudden*, i.e., there is no interaction of the excited photo electron with the remaining $N-1$ particle system, respectively.

$$\Psi_i^N = A\Phi_i^k\Psi_i^{N-1} \quad \text{and} \quad \Psi_f^N = A\Phi_f^k\Psi_m^{N-1} \tag{2.10}$$

The antisymmetric operator A thereby ensures the compliance with the Pauli principle. $\Phi_{i,f}^k$ depicts the initial and final state photoelectron wave functions with momentum k and Ψ_i^{N-1} the wave function of the initial system minus the future photoelectron. The wave function of the final state is here expressed as an excited state with wave function Ψ_m^{N-1}. Equations 2.9 and 2.10 allow to write the total photoemission intensity as

$$I(k, E_{kin}) \propto \sum_{f,i} |\underbrace{\langle\Phi_f^k|H_{per}|\Phi_i^k\rangle}_{M_{f,i}^k}|^2 \sum_m |\underbrace{\langle\Phi_m^{N-1}|\Phi_i^{N-1}\rangle}_{c_{m,i}}|^2 \delta(E_{kin} + E_m^{N-1} - E_i^N - h\nu) \tag{2.11}$$

with the one-electron dipole matrix element $M_{f,i}^k$ and the probability $|c_{m,i}|^2$ that the $N-1$ particle system remains in the excited state m. While dipole matrix elements take into account parameter of the excitation process, such as photoelectron momentum, final state, light polarization and experimental geometry, the transition probability considers many

body effects. In uncorrelated systems, the photoemission spectrum is given by a single delta function at the binding energy E_B^k of the electron. For correlated systems, however, $|c_{m,i}|^2$ has multiple non-zero entries and the spectrum additionally contains satellite features besides the main line. Within this work, ARPES measurements solely focus on the shape of the band structure - the momentum- and energy-dependent distribution of electrons. Correlation effects are hence not considered.

Transport of the photoelectron to the surface

After excitation, photoelectrons propagate through the crystal lattice and travel to the surface. Their kinetic energy thereby determines the inelastic mean free path (IMFP). For typical laboratory light sources, i.e., He I: 21.22 eV (ARPES) and Al K$_\alpha$: 1.49 keV (XPS) the IMFPs are about 0.6 nm and 4 nm, respectively, see figure 2.2 b). The photoelectron signal therefore mainly originates from near-surface atomic layers and makes this technique particularly surface sensitive. Those electrons that are inelastically scattered, e.g. by exciting plasmons in the crystal lattice, loose the information about their initial state and generate a continuous background in measured spectra at lower kinetic energies. In chapter 6, this additional intensity is considered for XPS spectra by subtracting the renowned Shirley background [62]. Satellite features due to plasmon excitations are accounted for in the respective fitting procedures.

Escape of the photoelectron from the surface

Photoelectrons only escape the surface if they are able to overcome the work function Φ of the solid. This requires a sufficient kinetic energy of

$$E_{kin} \geq h\nu - E_B - \Phi. \tag{2.12}$$

Due to the translational invariance in the plane of the surface, the parallel momentum component of a photoelectron at an emission angle of θ

$$k_{||} = \frac{1}{\hbar}\sqrt{2m_e E_{kin}} \cdot sin(\theta) \tag{2.13}$$

is conserved during the escape process. This momentum conversation does not hold for the perpendicular momentum component as it depends on the typically unknown inner

potential V_0 of the solid.

$$k_\perp = \frac{1}{\hbar} \sqrt{2m_e(E_{kin}cos^2(\theta) + V_0)} \cdot sin(\theta) \tag{2.14}$$

A complete image of the band structure $E(k)$ is therefore only possible if the inner potential is approximated theoretically oder elaborately measured [63]. For this work, $k_\perp$ can be neglected as the band structure of 2D systems does not disperse perpendicular to the surface. This allows to determine the entire band structure $E_{2D}(k) = E(k_{||})$ with the parallel momentum component.

2.2.2 ARPES & XPS Instrumentation

ARPES and XPS measurements were performed with a Phoibos 100 hemispherical analyzer from SPECS Surface Nano Analysis GmbH. The surface could be illuminated either with a He duoplasmatron lamp (21.22 eV) for ARPES or an X-ray gun with Al K_{alpha} anode (1.49 keV) for XPS measurements. The setup is attached to a UHV chamber with a base pressure $< 5 \cdot 10^{-10}$ mbar and an attached load lock enabling *in-situ* transfers to other UHV setups.

2.3 Low Energy Electron Diffraction

Besides PES, low-energy electron diffraction is another spatially averaging surface sensitive measurement technique. It allows to characterize a single-crystalline surfaces regarding prevailing periodic structures by utilizing the material-wave duality of electrons [64]. In a typical LEED setup, schematically shown in figure 2.3 a), a parallel beam of electrons is directed onto a crystal surface and the interference pattern of the diffracted beam is detected with a fluorescent screen. As the observed diffraction pattern directly pictures the reciprocal lattice of the sample surface, LEED is a powerful tool to investigate 2D adatom lattices. The surface sensitivity is thereby attributed to the low energy of the electrons typically used $(30 - 200$ eV$)$ which limits the IMFP of the electrons involved to the surface layers of the sample, see figure 2.2 b).

Due to the low penetration depth of the electrons, the reciprocal lattice probed by the electrons can be considered two-dimensional. It therefore consists of rods perpendicular to
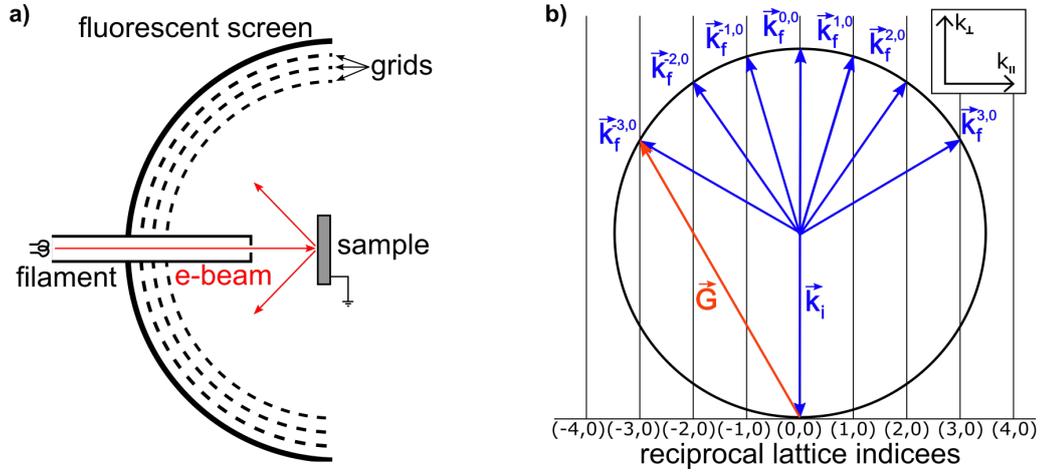
Figure 2.3: a) *Schematic illustration of a typical LEED setup. A collimated electron beam is directed onto a sample surface and its resulting interference pattern is observed with a fluorescent screen. b) Ewald construction that allows to visualize at which angle the Laue condition is met and constructive interference is achieved.*

the sample plane that follow the surface symmetry with reciprocal lattice vectors $\vec{G}$ [65]. Constructive interference of elastically scattered electrons is achieved if the wave vectors of the incoming $(\vec{k_i})$ and diffracted electrons $(\vec{k_i})$ fulfill the Laue condition

$$\Delta\vec{k} = \vec{k_i} - \vec{k_f} = \vec{G} \quad \text{with} \quad |\vec{k_i}| = |\vec{k_f}|.$$

It is easily visualized using the so-called Ewald construction, depicted in figure 2.3 b) for a two dimensional sample. Whenever a sphere with radius $|\vec{k_i}|$, centered around the base of $\vec{k_i}$, intersects a reciprocal lattice rod, the Laue condition is met and constructive interference is observed.

2.4 Density Functional Theory

The basic premise of density functional theory is that ground state properties of many-body systems can be derived solely from the knowledge of their electron density distribution. This idea was first mentioned by Thomas [66] and Fermi [67] in 1927, but a credible formalism was not found until the seminal papers by Hohenberg and Kohn in 1964 [68,69].

Hohenberg and Kohn [68] proofed that there exists a unique electron density ρ, that de-

termines the ground state energy E_0 of a many-body system

$$E_0 = T(\rho) + V_{ee}(\rho) + \int \nu_{ext}\rho \leq T(\rho') + V_{ee}(\rho') + \int \nu_{ext}\rho' \qquad (2.15)$$

with the kinetic energy of the electrons T, the total Coulomb interaction V_{ee} and the external potential of the atomic lattice ν_{ext}. This allows to determine the ground state energy of a system by minimizing the density functional representation of the total energy [70]

$$E(\rho) = T(\rho) + V_{ee}(\rho) + \int \nu_{ext}\rho. \qquad (2.16)$$

Kohn and Sham [69] provided a practical implementation of this approach by approximating V_{ee} with the classical Coulomb self energy

$$V_{ee} \approx J(\rho) = \frac{1}{2} \int \int \frac{\rho(1)\rho(2)}{r_{12}} d1d2, \qquad (2.17)$$

and the total kinetic energy with that of independent, non-interacting electrons with orthonormal orbitals Ψ_i

$$T(\rho) \approx T_0(\rho) = \frac{1}{2} \sum_i 2 \int \Psi_i * \nabla^2 \Psi_i. \qquad (2.18)$$

To compensate for errors of these approximations, they introduced the so-called exchange-correlation energy $E_{XC}(\rho)$ which itself depends on ρ. Equation 2.16 can then be expressed in the form of the Kohn-Sham total energy functional [70]

$$E(\rho) = T_0(\rho) + \int \nu_{ext}\rho + J(\rho) + E_{XC}(\rho). \qquad (2.19)$$

Minimization of the total energy then gives the Kohn-Sham orbital equations [70]

$$-\frac{1}{2}\nabla^2\Psi_i + \nu_{KS}\Psi_i = \epsilon_i\Psi_i \qquad (2.20)$$

with the effective Kohn-Sham potential

$$\nu_{KS} = \nu_{ext} + \nu_{el} + \frac{\delta E_{XC}}{\delta \rho}. \qquad (2.21)$$

in which ν_{el} contains the Hartree-type Coulomb interaction. Besides the exchange correlation functional $E_{XC}(\rho)$ and its derivative, all terms of the relatively simple equations 2.19 and 2.20 are given exactly. The theoretical description of the total energy of many-body

systems, including interactions and correlations, therefore depends only on an adequate approximation of the exchange correlation functional which is in general unknown.

Kohn-Sham [69] already gave a first approximation of the exchange correlation functional in 1965, the local density approximation (LDA), which is solely dependent on the electron density ρ

$$E_{XC}^{LDA} = \int \rho e_{XC}^{UEG}(\rho) \tag{2.22}$$

in which $e_{XC}^{UEG}(\rho)$ represents the exchange-correlation energy, per unit volume, of a uniform electron gas [70]. While this model gives good results for systems with a slowly varying electron density, more complex systems require sophisticated approaches for the exchange correlation functional such as the generalized gradient approximation (GGA) or hybrid functionals [70]. The first additionally considers -as the name already suggests - the gradient of the electron density

$$E_{XC}^{GGA} = \int \rho e_{XC}(\rho, \nabla \rho). \tag{2.23}$$

This exchange correlation functional can have many different forms depending on the respective implementation of the density gradient. Within this thesis, the popular GGA approach from Perdew-Burke-Ernzerhof (PBE) [71] was used by co-workers from the research group of Giorgio Sangiovanni, if not stated otherwise.
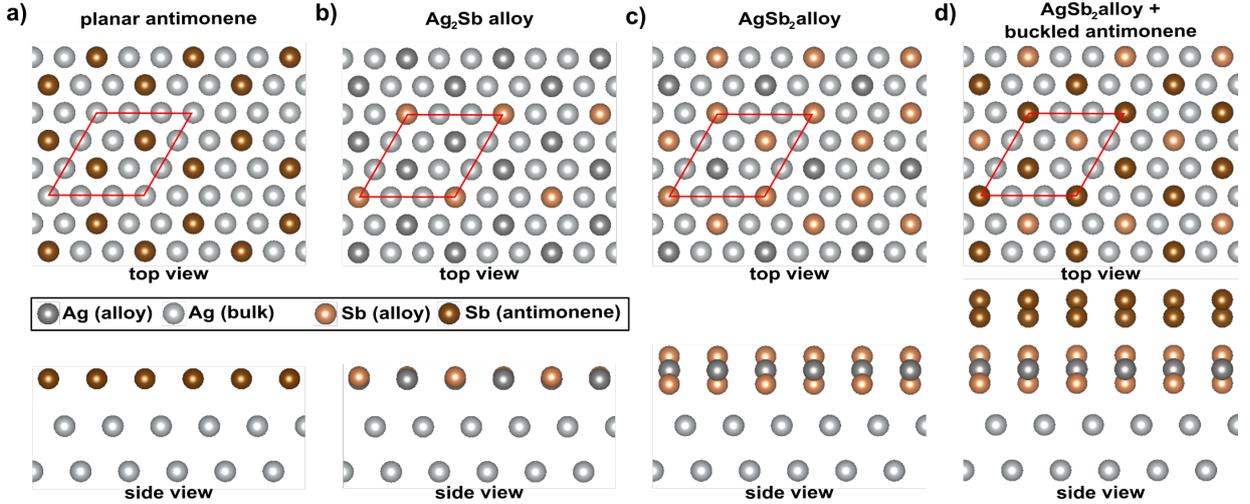
3 The $(\sqrt{3} \times \sqrt{3})R30°$ surface of Sb-Ag(111)

Silver has recently been reported as an appropriate substrate for the growth of a hexagonal monolayer lattice of Sb, so called antimonene, by two different groups [41, 42]. Both publications focus on STM experiments and report on the formation of an Sb-induced $(\sqrt{3} \times \sqrt{3})R30°$ surface reconstruction on the Ag(111) surface. The unit cell size of 5.0 Å implies the formation of an antimonene layer with a tensile strain of more than 16%. According to theoretical publications on strain-induced electronic properties of antimonene [44–46], such a large strain is supposed to cause a band inversion in the antimonene band structure which renders the film topologically non-trivial.

Despite both groups reporting on the same Sb-induced lattice periodicity and the formation of an antimonene monolayer, they propose different atomic lattice structures. On the one hand, Shao *et al.* [42] conclude on the formation of a flat Sb honeycomb lattice, alike graphene, that shows little interaction with the substrate, see figure 3.1 a). On the other hand, Mao *et al.* [41] report on the initial formation of a AgSb$_2$ alloy at the substrate surface that is subsequently covered with a buckled Sb honeycomb layer, see figure 3.1 c) and d). Both groups base their proposed atomic lattices primarily on a comparison of STM topography images with energetically stable atomic models obtained from DFT calculations. Their publications, however, lack an investigation of the electronic structure of their sample, e.g., by means of STS or ARPES. Thus, no experimental data of the antimonene band structure has yet been published to confirm the proposed lattices and their potential non-trivial topology.

Within this work, the $(\sqrt{3} \times \sqrt{3})R30°$ Sb-Ag(111) surface was investigated regarding its atomic and electronic structure with a combined study of LEED, STM, ARPES and X-ray standing waves (XSW) measurements. STM results reproduce the surface structures reported by Mao *et al.* [41], but no indications for the formation of such a complex atomic

Figure 3.1: *Atomic models [24] of different Sb-induced $(\sqrt{3} \times \sqrt{3})R30°$ surface structures Ag(111) reported in literature. The $(\sqrt{3} \times \sqrt{3})R30°$ unit cell is depicted in red for each lattice. a) Antimonene, a planar Sb honeycomb lattice with little substrate interaction [42]. b) A Ag_2Sb alloy, that shows a strong Rashba-splitting of its surface state [72, 73]. c) A $AgSb_2$ alloy with d) a buckled Sb honeycomb lattice on top, both reported by Mao et al. [41].*

structure could be observed with ARPES or XSW measurements. Instead, our data supports the formation of an Ag_2Sb surface alloy that has been known in literature since 1992 [74–76], see figure 3.1 b) for the corresponding atomic model. Our data therefore refutes the assertion made by Mao *et al.* [41] that claims the growth of a buckled antimonene layer.

3.1 Preparation and topographic characterization of Sb-Ag(111)

The sample used within this chapter was a Ag(111) single crystal provided by Tien-Lin Lee from I09 beamline at Diamond Light Source[1]. The sample was cleaned *in-situ* by repeated cycles of argon sputtering followed by a short annealing until a clean Ag(111) surface was obtained. Throughout the study, the sample was kept in UHV with a base pressure below 5×10^{-10} mbar. Highly pure Sb (99.9999%) was evaporated using a commercial Knudsen cell with the substrate held at room temperature. The sample was subsequently annealed to about 300°C to remove excess Sb and achieve an atomically flat surface with

---

[1] Diamond Light Source Ltd, Didcot, Oxfordshire, UK

local point defects, see figure 3.2 a). LEED and close-up STM measurements shown in 3.2 b) and c), respectively, indicate the formation of a well-ordered six-fold symmetric $(\sqrt{3} \times \sqrt{3})R30°$ surface structure identical to that reported by Mao *et al.* [41]. The STM image is thereby independent from the applied tunneling parameters (voltage, current) and can only reproduce the appearance of a honeycomb lattice, as reported by Shao *et al.*, in the case of a misshaped STM probe.
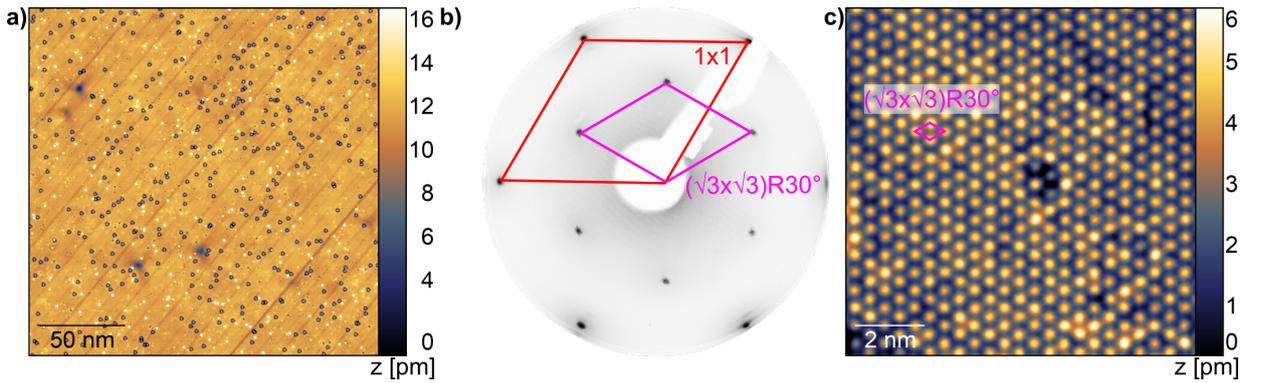
Figure 3.2: *Characterization of a Ag(111) surface after Sb growth. a) STM overview image (1.0 V, 20 pA) with large, atomically flat terraces with randomly distributed point defects. b) LEED (45eV) indicates the formation of a well-ordered $(\sqrt{3} \times \sqrt{3})R30°$ lattice besides the 1×1 spots of the Ag(111) substrate. c) STM zoom-in into a) (−0.1 V, 250 pA) shows a well-ordered lattice with a $(\sqrt{3} \times \sqrt{3})R30°$ reconstruction.*

The surface structure obtained after Sb evaporation was found to be independent of the post-annealing temperature ranging from a low-temperature anneal estimated to about 50°C to 100°C up to a temperature of 300°C. This insensitivity can be seen unambiguously seen in STS spectra taken on samples annealed with different temperatures, shown in figure 3.3 a). Both surfaces show an identical pronounced peak in the LDOS at about +0.75 eV. A detailed view on the $(\sqrt{3} \times \sqrt{3})R30°$ surface lattice reveals different kind of defects in the atomic structure, see figure 3.3 b). They comprise two different local defects and a bright boundary between domains with differently oriented $(\sqrt{3} \times \sqrt{3})R30°$ lattices. All three types of defects are likewise reported by Mao *et al.* [41].

All in all, STM topography images taken on a Sb-Ag(111) surface show a well-ordered $(\sqrt{3} \times \sqrt{3})R30°$ lattice with a six-fold symmetry, independent of the post-annealing temperature. They compare well with those published by Mao *et al.* [41] that are proposed to show a buckled antimonene lattice. A honeycomb structure in STM, as shown in the publication from Shao *et al.* [42] could not be reproduced.
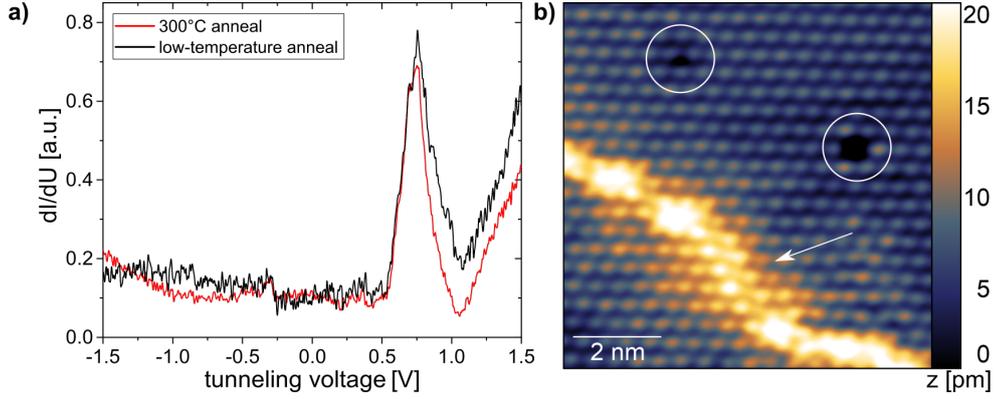
Figure 3.3: *a) STS spectra taken on the $(\sqrt{3} \times \sqrt{3})R30°$ Sb-Ag(111) surface after sample preparation with a low-temperature and high temperature anneal. b) Detailed STM topography scan $(-0.1$ V, 3 nA$)$ including different types of point defects (circles) and a surface domain boundary (arrow) between differently oriented domains.*

3.2 Electronic structure of Sb-Ag(111)
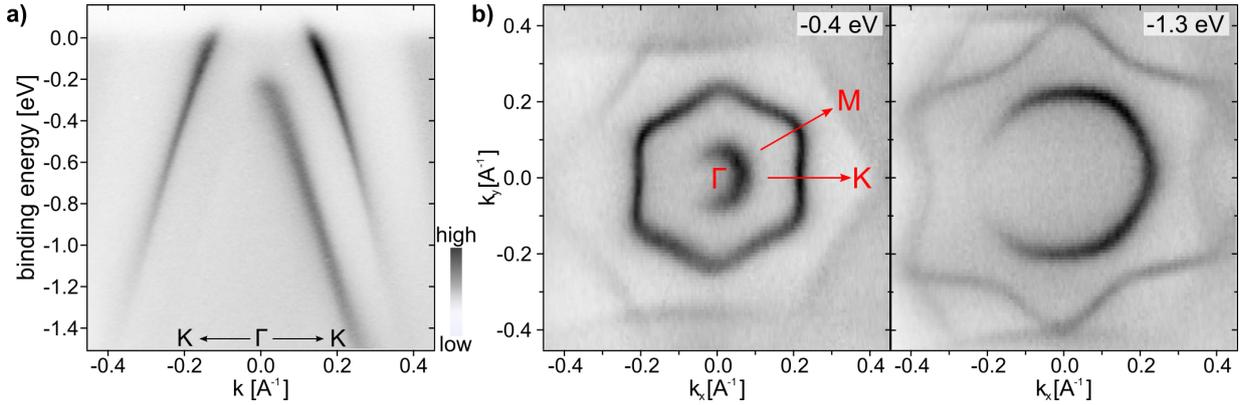
Figure 3.4: *a) Band structure measurement along K-Γ-K. Two parabolas are centered around Γ from which one crosses the Fermi level. b) Constant energy contours at -0.4 eV and -1.3 eV. A circular and hexagonal feature are present around Γ and surrounded by faint intensity of the backfolded Ag bulk conduction band.*

Following the STM measurements, the homogeneous Sb-$(\sqrt{3} \times \sqrt{3})R30°$ surface of the Ag(111) single crystal was investigated regarding its electronic band structure with ARPES. The band dispersion along $\overline{\Gamma K}$, see figure 3.4 a), consists of two hole-like parabolas centered around Γ. The upper band crosses the Fermi level at $k_F = \pm 0.13$ Å^{-1} thereby forming a hole pocket around Γ, while the lower band has its band maximum in the occupied states at -270 meV. Figure 3.4 b) shows cuts through the momentum space at a constant energy, so called constant energy contours (CECs). They consist of three features, the intense

constant energy contours of both hole-like parabolas around Γ and another faint feature with an almost hexagonal shape surrounding them. While the inner contour shows a circular shape, the constant energy contour of the metallic band exhibits a strong hexagonal distortion.

This ARPES data is in good agreement with the Rashba-split band structure measured by Moreschini *et al.* [72] on a Ag(111) sample with a Ag_2Sb surface alloy. According to Moreschini *et al.*, the outermost faint constant energy contour in figure 3.4 b) can be attributed to a Ag bulk band that is back-folded at the zone boundary of the alloy Brillouin zone. The groups first-principles calculations predict that the band maximum of the metallic hole pocket is located at around +0.7 eV which is in good agreement with the LDOS maximum observed with STS in figure 3.3 b).

A comparison of the experimental band structure obtained on the Sb-Ag(111) single crystal to DFT calculated band structures for the atomic lattices proposed by Mao *et al.* [41] or Shao *et al.* [42] does not show any conformity. Despite similarities in STM, the ARPES data obtained on our Sb-Ag(111) sample therefore strongly contradicts the formation of a planar or buckled antimonene layer.

3.3 The X-ray standing wave technique

3.3.1 Measurement principles

In order to clarify this controversy between STM and ARPES results in regard to other publications, we analyzed the Sb-Ag(111) single crystal surface with the X-ray standing wave technique at beamline I09 at Diamond Light Source[2]. Measurements and analysis have been performed in collaboration with Judith Gabel and Tien-Lin Lee. The XSW technique dates back to 1964, when Batterman *et al.* [77] were able to observe an X-ray standing wave field inside a germanium crystal by measuring the dependency of the samples fluorescence curve on the incidence angle of the X-ray beam. The standing wave in the crystal thereby originates from the interference of the incident and reflected X-ray beam and reflects the periodicity and orientation of the mirror planes responsible for the Bragg reflection, schematically shown in figure 3.5 a). The photoelectrons excited by this standing

---

[2]Diamond Light Source Ltd, Didcot, Oxfordshire, UK

wave field carry information about the structural and chemical composition of the sample which can be extracted, e.g., with a hemispherical electron energy analyzer. In order to generate a homogeneous standing wave field, a high degree of uniformity is needed for the bulk structure of the sample which limits the choice of substrates to single crystals.
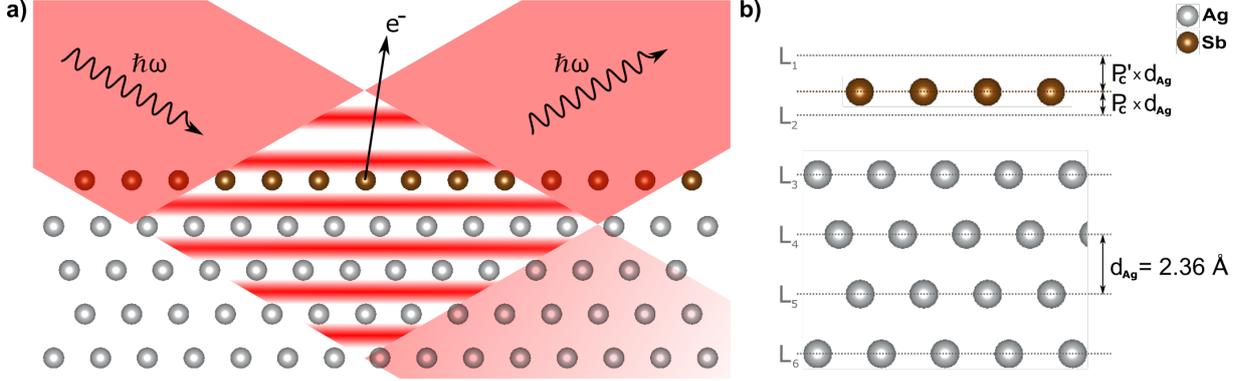
Figure 3.5: a) *Schematic of the XSW process at the sample surface. Under the Bragg condition, the reflected X-ray interferes with the incoming beam and creates a standing wave field that follows the periodicity of the underlying lattice planes. Sweeping the beam energy around the Bragg condition entails a phase shift of the standing wave relative to the lattice planes. If a position of maximum intensity coincides with the position of an atom, photoelectrons are exited and collected by a detector. b) Atomic positions [24] are measured relative to the periodicity of the Ag(111) lattice planes (labeled L_x). XSW measurements reveal the value of P_c which describes the relative distance from the corresponding atom to the first lattice plane in the direction of the substrate (L2). Simulations that include damping of photo electrons take the first lattice plane in the direction away from the substrate (L_1) as reference and therefore require $P_c' = 1 - P_c$.*

The physics of this method is centered around the dipolar photo-absorption process of the X-ray standing wave which takes place exactly at the center of the atoms [78]. Tuning the energy of the X-ray beam through the Bragg condition generates a phase shift of the X-ray standing wave field relative to the Bragg planes. The corresponding energy-dependent intensity change of photoelectrons is simultaneously detected for a certain core level and allows to extract structural information of the underlying atomic species normal to the Bragg planes.

The relation between the photo-electron yield Y, the spatial distribution of the corresponding atomic species $\rho(r)$ and the standing wave intensity $I(\Theta, E_\gamma, r)$ can be expressed as

$$Y_A(\Theta, E_\gamma) \propto \int \rho(r) I(\Theta, E_\gamma, r) dr. \tag{3.1}$$

for a beam energy E_γ and an incidence angle Θ [78]. For an X-ray beam in normal incidence, the general form of the intensity of a standing wave field $I(\Theta, E_\gamma, r)$ is dependent

on the reflectivity $R(\Theta, E_\gamma)$, the lattice vector H and the phase difference $\nu(\Theta, E_\gamma)$ between incident and reflected wave.

$$I(\Theta, E_\gamma, r) = I_0\{1 + R(\Theta, E_\gamma) + 2\sqrt{R(\Theta, E_\gamma)}cos[\nu(\Theta, E_\gamma) - 2\pi H \cdot r]\}. \qquad (3.2)$$

The substitution of (3.2) in (3.1) allows to express the photo-electron yield in the form

$$Y(E_\gamma) = Y_0\{1 + R(E_\gamma) + 2\sqrt{R(E_\gamma)}F_c cos[\nu(E_\gamma) - 2\pi P_c]\}, \qquad (3.3)$$

which only dependents on two parameters, the coherent fraction F_c and coherent position P_c [78]. As the name already suggests, the coherent position P_c carries information about the averaged atomic position of an atomic species. The result does not represent an absolute value, but the relative normal position of the relevant atoms to the Bragg planes of the substrate, ranging from 0 to 1, see figure 3.6 b) for visualization. For a single adsorption site of an atom species, 0 and 1 imply a position directly on a mirror plane L while 0.5 implies a position half way between two mirror planes. The value of the coherent fraction F_c equals 1 if all coherent positions of a certain atomic species are the same and diminishes if multiple positions are taken. In the simple case of a single atomic adsorption site of an adsorbate, the experimentally obtained coherent position determines its position relative to the mirror planes and the coherent fraction is close to 1.

3.3.2 X-ray standing wave measurements
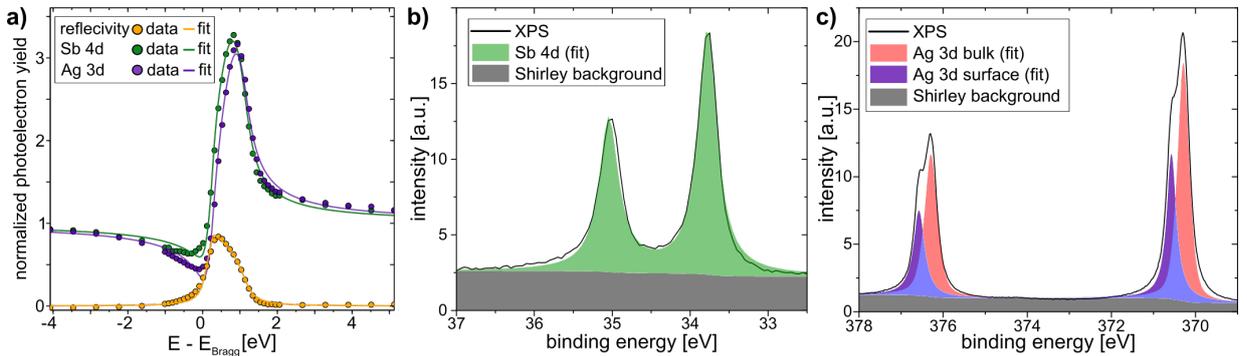
Figure 3.6: *a) Normalized photoelectron yield for the reflectivity and the Sb 4d and Ag 3d core levels. b) and c) Corresponding XPS spectra of both core levels. The spectral shape of Sb 4d can be fitted with a single peak doublet. The Ag 3d core level spectrum shows a splitting that can be attributed to bulk Ag (red) and Ag(111) surface atoms (purple).*

atomic species	position	coherent fraction F_c	coherent position P_c $\Delta P_c = \pm 0.01$	absolute position [Å] $\Delta = \pm 0.023$
Ag	1	1.000	0.069	0.163
	2	1.041	0.068	0.161
	3	1.040	0.071	0.168
Sb	1	0.901	0.124	0.293
	2	0.955	0.123	0.290
	3	0.946	0.127	0.300
Ag	∅	1.027±0.023	0.069±0.017	0.164±0.04
Sb	∅	0.934±0.029	0.125±0.017	0.294±0.04

Table 3.1: *XSW results for the coherent fraction and coherent position after fitting the photoelectron yield line shape for different spots on the Ag(111) crystal. The absolute position is calculated under the assumption of a single adsorption site.*

After transfer of the Sb-Ag(111) single crystal to the Diamond Light Source[3] in a UHV suitcase, the surface quality was checked with XPS and LEED. No contaminants or signs of surface degradation could be detected. For the XSW measurement, the beam energy was set to 2.63 keV in normal incidence to the Ag(111). The energy was tuned in a range of $[-4, +5]$ eV relative to the Bragg condition of the (111) mirror planes while the reflectivity and photoelectron yield of the Ag$3d^{\frac{5}{2}}$ and Sb$4d^{\frac{5}{2}}$ core levels were recorded. To statistically confirm the results, three different spots of the single crystal have been probed. The experimental photo electron yields obtained with the XSW technique for one of those positions as well as the relevant XPS core level spectra are displayed in figure 3.6. Using a standard fitting procedure, the coherent position and coherent fraction for both atomic species have been extracted from the photoelectron yield line shape with equation 3.3[4], see table 3.1. Assuming a single adsorption site, justified due to a coherent fraction close to 1, the absolute position can be calculated by multiplying the coherent position P_c with the mirror plane spacing of the Ag(111) surface of $d_{111} = 2.36$ Å. The absolute position can, however, deviate by multiples of d_{111}. Nevertheless, in the simple case of a single adsorption site, it is usually possible to determine an absolute position by a comparison of the XSW results to DFT calculations or by taking into account physically realistic bond lengths.

The measurements taken on different positions on the Ag(111) single crystal yield very sim-

---

[3]Diamond Light Source Ltd, Didcot, Oxfordshire, UK

[4]Data fitting performed by Tien-Lin Lee (Principal Beamline Scientist on I09 of Diamond Light Source in Didcot, Oxfordshire, UK).

ilar results and confirm a homogeneous coverage of the Sb-induced surface reconstruction on the Ag(111) surface. For the Sb core level, the average coherent fraction and coherent position are determined as $F_{c,Sb} = 0.934 \pm 0.029$ and $P_{c,Sb} = 0.125 \pm 0.002$, respectively. The value of the coherent fraction close to 1 thereby indicates a single Sb adsorption site relative to the substrate mirror planes. The small deviation might arise due to the presence of Sb atoms displaced by point defects and domain boundaries or to individual Sb adatoms, as exemplary shown in figure 3.3 b). XPS additionally supports the hypothesis of a single adsorption site with a Sb 4d core level spectrum that can be fitted with a single fine structure doublet of $4d^{\frac{3}{2}}$ and $4d^{\frac{5}{2}}$ core levels , see figure 3.6 b). Under this assumption, the coherent position can be translated in an absolute distance normal to a Ag(111) mirror plane of (0.294 ± 0.005)Å.

For the Ag 3d core level, the measurement detects a deviation from the Ag(111) bulk mirror planes as well. This implies a shift of Ag atoms away from their intrinsic bulk position. The averaged coherent fraction for these atoms is $F_{c,Ag} = 1.027 \pm 0.023$ and their coherent position $P_{c,Ag} = 0.069 \pm 0.001$ which translates to an absolute shift from their bulk position towards the surface of (0.164 ± 0.004)Å. The unphysical value of the coherent fraction larger than 1 can thereby be attributed to non-linear effects in the detector. An XPS measurement of the Ag 3d core level additionally confirms the observation of Ag atoms in a non-bulk configuration. The spectrum shows two separate binding energies for both fine structure doublets with a separation of 0.3 eV, see figure 3.6 c). Intuitively, the slight outward relaxation of the substrate atoms can be expected to happen in the surface layer that interacts with the Sb atoms. Such a shift of the surface Ag atoms has likewise been reported for an Ag_2Sb surface alloy by several groups [73, 79, 80].

3.3.3 X-ray standing wave simulation

In order to compare the different atomic models available in literature with the XSW results, the coherent fraction and coherent position for each proposed atomic structure have been simulated by solving equation

$$F_c e^{2\pi i P_c'} = \int \rho(r) e^{2\pi i H \cdot r} dr \cong \frac{\sum_i \left(\frac{n_i}{n}\right) e^{-\frac{P_{c,i}' d_{111}}{\lambda_{IMFP}}} e^{2\pi i P_{c,i}'}}{\sum_i \left(\frac{n_i}{n}\right) e^{-\frac{P_{c,i}' d_{111}}{\lambda_{IMFP}}}} \tag{3.4}$$

positions $P'_{c,i}$	Ag$_2$Sb alloy [73]	planar antimonene [42]	AgSb$_2$ alloy [41]	AgSb$_2$ + buckled Sb-ene [41]
1	0.915	0.933	0.44±0.10	0.20±0.10
2	-	-	1.07±0.10	0.59±0.10
3	-	-	-	1.44±0.10
4	-	-	-	2.07±0.10
coherent position P'_c	0.915	0.933	$0.41^{+0.12}_{-0.10}$	$0.26^{+0.12}_{-0.15}$
coherent position P_c	0.085	0.067	$0.59^{+0.10}_{-0.12}$	$0.74^{+0.15}_{-0.12}$
coherent fraction F_c	1	1	$0.68^{+0.15}_{-0.14}$	$0.51^{+0.15}_{-0.04}$

Table 3.2: *Positions $P'_{c,i}$ for Sb atoms of all atomic models under consideration as well as their corresponding simulated coherent positions P'_c, P_c and the coherent fraction F_c. Atomic positions of the Ag$_2$Sb alloy and planar antimonene are given in the respective publications [42, 73]. Those of the AgSb$_2$ alloy with and without a buckled antimonene are estimated from the figures shown by Mao et al. [41] and therefore prone to errors. This is taken into account by adding an error of ±10% of the Ag lattice constant to these atomic position.*

for F_c and P_c [81] under the assumption of a discrete density $\rho(r)$ with n_i atoms at site i ($n = \sum_i n_i$). In order to account for the damping of photo electrons escaping from below the surface with an inelastic mean free path λ_{IMFP}, the coherent position is measured relative to the first mirror plane located away from the substrates surface and hence named $P'_c = 1 - P_c$ (see figure 3.5 b) for visualization).

For the planar Sb honeycomb structure [42] and the Ag$_2$Sb alloy phase [73], experimental or theoretical values for atomic positions of the Sb atoms are given in the respective publications and allow an accurate simulation. Unfortunately, no structural information is provided by Mao *et al.* [41] besides graphical representations of their atomic structure. The interatomic distances have therefore been estimated from the dimensions of the provided figures. In order to compensate for errors provided by this rather rough approach, the simulation has also been done for atomic models in which the relative position of each Sb atom was altered by ±10% of the Ag lattice constant with the remaining Sb positions being fixed. The results of the XSW simulations are displayed in table 3.2.

For each atomic model with more than one adsorption site P_c, the simulated coherent position P_c is larger than 0.47 and the coherent fraction below 0.83. The XSW results therefore exclude the structural models proposed by Mao *et al.* [41], namely a AgSb$_2$ alloy with or without an additional buckled antimonene layer on top. Simulations for the models with a single Sb adsorption site, the planar antimonene and Ag$_2$Sb surface alloy, obviously

yield a simulated coherent fraction of 1 in agreement with the experimental observation. In addition, both simulated coherent positions are in proximity of the experimental value of 0.125 ± 0.017. For the Ag_2Sb surface alloy the simulated coherent position is $P_c = 0.085$ while it is $P_c = 0.067$ for the planar layer of antimonene. Due to a similar value obtained for both atomic structures, the simulation results do not allow to unambiguously decide between those two lattice candidates.

3.4 Comparison with proposed atomic models

The experimental data acquired with STM, ARPES, XPS and XSW on the Sb-$(\sqrt{3} \times \sqrt{3})R30°$ Ag(111) surface allows to make a comparison to the data published on different Sb-induced atomic surface structures on Ag(111). In the following, the experimental results obtained within this work are compared to those published in literature [41, 42, 72, 73]. During the writing of this thesis, we became aware of a publication by Zhang *et al.* [82] that investigates the Sb-Ag(111) and Sb-Cu(111) surfaces with Raman spectroscopy and provides evidence that excludes the formation of an antimonene layer on the Ag(111) surface and attributes the observed $(\sqrt{3} \times \sqrt{3})R30°$ surface reconstruction to an Ag_2Sb surface alloy.

3.4.1 AgSb$_2$ alloy & buckled antimonene

STM topography images taken on our Sb-induced Ag(111) surface do not only reproduce the six-fold symmetric unit cell allegedly taken on a buckled antimonene layer, but additionally show all types of point defects and domain boundaries reported on by Mao *et al.* [41], as shown in figure 3.3 b). This allows to conclude that within this work the same surface structure has been grown and investigated. Mao *et al.* attribute their experimental results to the formation of a $AgSb_2$ alloy (figure 3.1 c)) that is covered by a buckled hexagonal Sb lattice (figure 3.1 d)). Despite an agreement in STM data, our ARPES data does not show similarities to the DFT-derived band structure shown by Mao *et al.*. Their proposed band gap at Γ of more than 2 eV is in stark contrast to the parabolic hole pockets observed with our ARPES experiment. The discrepancy to their proposed atomic model with three different Sb adsorption sites is additionally bolstered by the experimental observation of a single adsorption site with XSW measurements. The data taken within

this work therefore refutes the allegation of the successful preparation of a buckled anti-monene layer on the Ag(111) surface as asserted by Mao *et al.* [41], in accordance with the publication of Zhang *et al.* [82].

3.4.2 Planar antimonene

Shao *et al.* [42] report on the growth of a planar antimonene lattice on Ag(111), schemat-ically depicted in figure 3.1 a). Similar to Mao *et al.* [41] and this work, their surface preparation consists of the Sb evaporation with the Ag(111) sample held at room tem-perature followed by a subsequent anneal to 80°C. They claim that their low-temperature anneal allows to extend the growth of isolated Sb islands on Ag(111), previously reported by several groups [83, 84], to cover the entire surface. The interaction of the antimonene lattice with the substrate is deemed negligible as no chemical shift is observed in their Ag 3d core level spectrum in XPS.

The STM topography scans published by Shao *et al.* differ from those obtained within this work. Instead of a triangular array of bright spots, they observe a planar hexagonal surface lattice. Regarding the electronic structure, it is only possible to compare our experimental ARPES data to DFT band structure calculations for a free-standing antimonene layer with the lattice constant of the Ag(111) surface. Their calculations do not show a metallic behavior as observed within this work, but show a large band gap of more than 3 eV at Γ. Due to this large discrepancy, we can safely exclude that the Sb-Ag(111) surface investigated within this work featured a planar antimonene layer.

While the STM results presented by Shao *et al.* [42] indeed allow to draw the conclusion of a planar honeycomb layer, the group does not support their claim with a complementary experimental technique to exclude possible measurement artifacts, e.g., a misshaped STM tip. Due to their simple growth conditions, it seems astonishing that a planar antimonene phase covering the entire surface has not yet been observed taking into account the amount of experimental studies [41, 72, 73, 76, 79, 83–85] on the Sb-induced Ag(111) surface. Ac-cording to first principles calculations by Oppo *et al.* [75], the provision of thermal energy supports the incorporation of Sb in a Ag-Sb surface alloy. The low temperature anneal at 80°C used during sample preparation by Shao *et al.*, comparable to the low temperature anneal used within this work, should as such promote the alloy formation. Without ex-perimental data provided by Shao *et al.* on the electronic structure of their Sb-Ag(111) it

is therefore doutable if the group has indeed been able to synthesize a planar antimonene layer.

3.4.3 Ag$_2$Sb alloy

The Ag$_2$Sb alloy, displayed in figure 3.1 b), is a Sb-induced phase that is known and widely investigated since the 90's [74–76,79,80,83,85–88] due to the role of Sb as surfactant during the epitaxial growth of silver crystals. At low temperatures, Sb atoms were found to form Sb islands on Ag(111) that get embedded into the Ag surface layer upon annealing [75,76]. Later, in 2009, this surface alloy came back into focus after related Ag surface alloys with Bi and Pb showed an unexpected large Rashba-type spin splitting of their surface bands [72, 73].

With no atomically resolved STM data available in literature for the Ag$_2$Sb alloy, a comparison to available publications is limited to ARPES and XSW results. The band structure obtained on the Sb-Ag(111) sample investigated in this work matches well to the experimental and theoretical data published by Moreschini *et al.* [72] obtained for the Ag$_2$Sb alloy. XSW results obtained within this work further support the presence of this surface alloy. They support a single adsorption site of Sb and resolve an outward relaxation of the Ag surface layer which has also been reported by several groups [72, 73, 79, 80, 89] which investigated the alloy phase experimentally. The Sb-Ag(111) surface under investigation in this work can therefore be identified as the well-known Ag$_2$Sb surface alloy.

3.5 Conclusion

By means of a comprehensive experimental study with complementary surface sensitive techniques, including LEED, STM, ARPES, XPS and XSW, we are able to characterize the Sb-induced surface under investigation as a Ag$_2$Sb alloy. It is unambiguously identified by a six-fold symmetric $(\sqrt{3} \times \sqrt{3})R30°$ lattice in STM, the observation of a single Sb adsorption site with XSW measurements and a good agreement of the ARPES data to first principles calculations and published experimental band structures. No signs for the formation of a planar or buckled Sb honeycomb lattice could be found. Instead, the perfect agreement of our STM data with that published by Mao *et al.* [41] allows to refute their assertion of the growth of a buckled antimonene layer. All in all, our findings are in agreement with the

statement made by Zhang *et al.* [82] that a planar or buckled antimonene layer on Ag(111) does not exist.

4 Sb islands on InSb(111) - A moiré system

A promising substrate candidate for the growth of a strained single bilayer of Sb is the III-V semiconductor InSb with its room temperature band gap of 170 meV [90]. Its In-terminated (111) surface - typically named InSb(111)A- offers a three-fold symmetric buckled honeycomb surface with a bi-atomic basis, see figure 4.1 c). The unreconstructed (111) surface possesses unsaturated dangling bonds of In atoms which have the tendency to form bonds to lower the surface energy. The intrinsic surface termination of InSb(111) therefore does not show the simple 1×1 bulk periodicity, shown in figure 4.1 c), but more complex reconstructions with larger periodicities such as a 2×2 or $(2\sqrt{3} \times 2\sqrt{3})$R30° [91]. In the presence of adatoms, intrinsic surface reconstructions can be substituted by adatom-induced surface lattices that typically adapt to the lattice of the underlying substrate [13, 92, 93]. With a lattice constant of 0.46 nm, the InSb(111) surface offers a template for the growth of a hexagonal Sb layer including a 7% tensile strain compared to bulk Sb(111). This strain is supposed to be sufficient to realize the strain-driven topologically non-trivial phase of the buckled Sb bilayer according to Chuang *et al.* [46] and Huang *et al.* [45]. The groups predict the transition from the trivial to the topological phase above a strain of 4.6% and 6%, respectively. Only Zhao *et al.* [44] except a larger strain of 9.7% to achieve a topological transition according to their calculations. Independent of which prediction is most valid, a successful strained growth would, on the one hand, show the general feasibility to strain an Sb bilayer by means of the epitaxial growth on a strongly lattice mismatched substrate and, on the other hand, enable to experimentally investigate the influence of strain on its electronic properties.

In contrast to expectations of an strained epitaxial growth, we find that Sb does not adapt to the lattice of the Inb(111)A substrate, as will be shown in the following chapter. Instead, Sb grows unstrained in triangular islands of various thicknesses thereby keeping its atomic

bulk lattice structure. While a strain-driven topological phase transition can therefore not be observed, the growth of Sb islands with various thicknesses allows to investigate thickness-dependent properties of antimony. These should show several topological phase transitions from a trivial insulator to a topological semi-metal if the thickness is increased from the monolayer to the bulk regime, as predicted for free-standing antimony by Zhang *et al.* [47].

In this chapter, we report on the successful preparation of unstrained Sb bilayer films with various thicknesses - from the monolayer limit to thick (> 20 BL) films - on InSb(111)A by a combined study of STM and scanning transmission electron microscy (STEM). Considering a local approach in DFT, the unstrained growth of Sb on InSb(111) is deemed energetically favorable compared to a strained growth. The lattice mismatch at the interface thereby manifests in a surface corrugation of the Sb layers which can be observed in form of a moiré pattern. The surface state of Sb is experimentally confirmed to persist down to low film thicknesses by the investigation of quasi particle interference patterns, in agreement with DFT calculations provided by Stefan Enzner. The data shown in this chapter has been published in collaboration with the research group of Giorgio Sangiovanni [94].

4.1 Preparation and structural characterization of Sb islands on InSb(111)
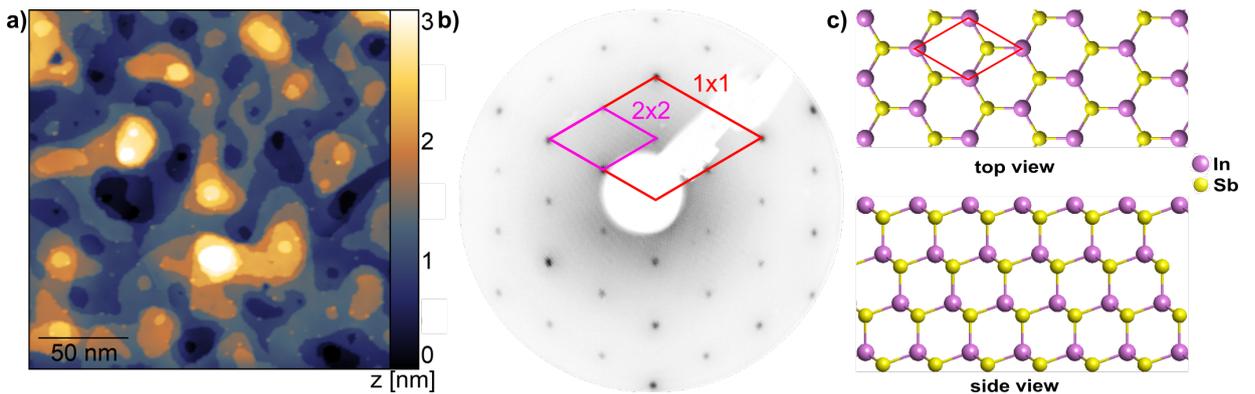
Figure 4.1: a) *STM overview (1.0 V, 50 pA) scan of the InSb(111)A surface after in-situ cleaning procedures showing atomically flat terraces separated by atomic steps. b) LEED (45 eV) confirms a well-ordered surface termination with the established 2×2 surface reconstruction. c) Atomic model [24] of the unreconstructed InSb(111)A surface in top and side view with the 1×1 unit cell marked red. For clarity, the top view is limited to the atoms of the surface layer.*

The InSb(111)A substrate was initially cleaned *ex-situ* in an ultrasonic bath with organic solvents (acetone, isopropanol, methanol) to remove a layer of photoresist and rough contamination before transfer into a UHV chamber with a base pressure below 5×10^{-10} mbar. Additional cleaning was performed *in-situ* with repeated cycles of argon sputtering and subsequent anneals to 340°C. Before growth, the surface quality was investigated using LEED and STM [see figure 4.1 a) and b)]. The as-cleaned surface has atomically flat terraces of arbitrary shape separated by single atomic steps. The observation of the established InSb(111)A 2×2 surface reconstruction [95] in LEED additionally indicates a well defined surface termination. Highly pure Sb (99.9999%) was evaporated using a commercial Knudsen cell with the substrate held at a temperature of about 110°C.
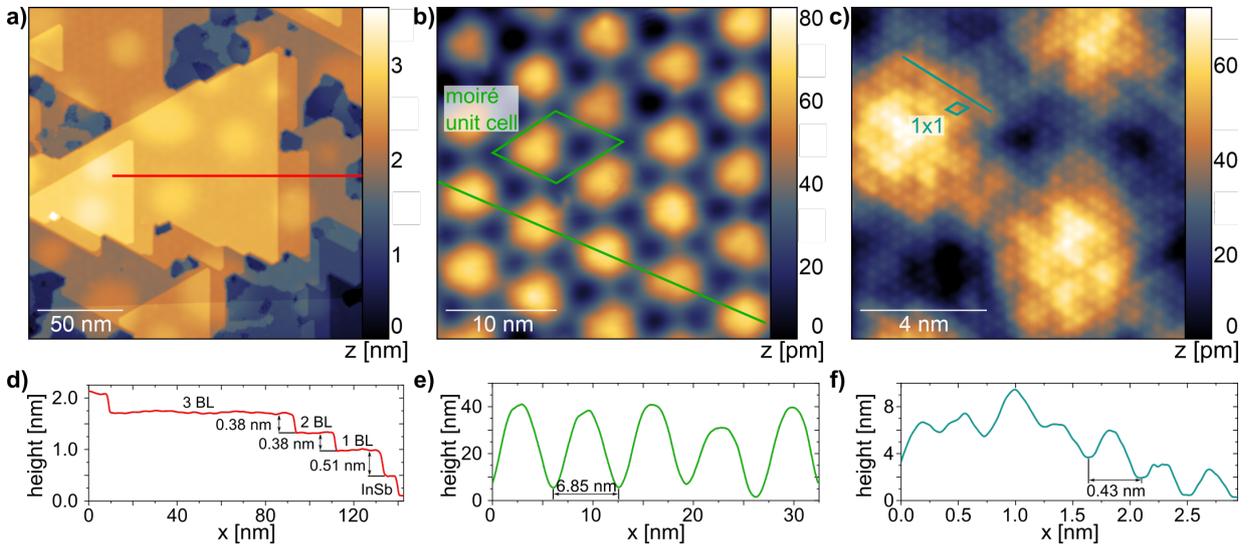
Figure 4.2: *a) STM overview scan (1.5 V, 30 pA) after Sb growth shows no homogeneous growth but the formation of triangular Sb islands of various thicknesses. b) Zoom-in STM image (−3.8 V, 60 pA) of the long-range intensity modulation (moiré superstructure) on top of a 4 BL Sb island. c) Close-up STM image (0.1 V, 200 pA) of a 5 BL island revealing a six-fold symmetric atomic structure superimposed with the moiré pattern. d)-f) Height profiles along lines marked in a)-c), respectively.*

After Sb deposition, the surface is covered with pyramid-like triangular Sb islands of various sizes and thicknesses, as shown in figure 4.2 a). Depending on the duration of Sb evaporation, island thicknesses can vary from a single Sb BL up to thick Sb layers of > 20 BL. Due to a Volmer-Weber type growth behavior [96], no homogeneous coverage of the substrate with a defined thickness can be achieved. Instead islands within a certain range of thicknesses are present simultaneously. An inhomogeneous Sb wetting layer around the Sb islands on the bare InSb(111) surface can be removed with a post-anneal to 200°C after

initial Sb growth. The substrate thereby forms the established Sb-rich $(2\sqrt{3} \times \sqrt{3})$R30°
reconstruction of the InSb(111)A surface [97], see figure 4.4 c). A line profile across the Sb
island of figure 4.2 a) allows to extract the step height separating adjacent terraces within
an Sb islands, see figure 4.2 d). The value of 0.38 nm agrees well with the atomic step
height of Sb(111) in its bulk configuration. An increased height of 0.51 nm is observed
for the first Sb layer relative to the substrate surface. The Sb terraces are covered with a
large scale six-fold symmetric periodic intensity modulation with a unit cell size of about
(6.85 ± 0.10) nm, shown in 4.2 b) and e). As will be later shown in section 4.2, this moiré
pattern can be attributed mainly to a surface corrugation caused by the lattice mismatch
of the Sb film and substrate at the interface. Close-up STM topography measurements
allow to resolve the atomic lattice of the Sb islands and reveal a six-fold symmetric atomic
structure with a unit cell size of (0.43 ± 0.05) nm, see 4.2 c) and f). The unit cell size is
identical with that of bulk Sb indicating the formation of the buckled hexagonal lattice of
Sb(111). The observed six-fold symmetry, compared to the three-fold symmetry expected
for a buckled hexagonal lattice, can be explained with the selective sensitivity of the STM
that only captures atoms of the Sb bilayer buckled upwards. In combination, the observed
unit cell size and terrace step height allow to determine the nature of the islands as stacked
Sb layers with a buckled honeycomb structure, so called β-antimony, as shown in figure 4.3
a). The bulk-like unit cell size of 0.43 nm additionally indicates that the Sb layers do not
adapt to the larger lattice constant of the substrate of 0.46 nm but keep the unstrained
bulk lattice structure, an observation that will be confirmed by data shown in figure 4.3.

4.2 Structural properties of moiré superstructure

Insights into the origin of the periodic intensity modulation are obtained by STEM mea-
surements on an Sb-InSb(111)A sample[1]. As the sample was exposed to ambient atmo-
sphere during sample transfer, thick Sb layers have been grown in order to protect the
interface from potential oxidation. Figure 4.3 a), shows a close-up image of the interface
between the Sb film and the substrate (marked with a dashed green line). In its surface

---

[1]provided by Dr. Martin Kamp (Physikalisches Institut Julius-Maximilians-Universität Würzburg)
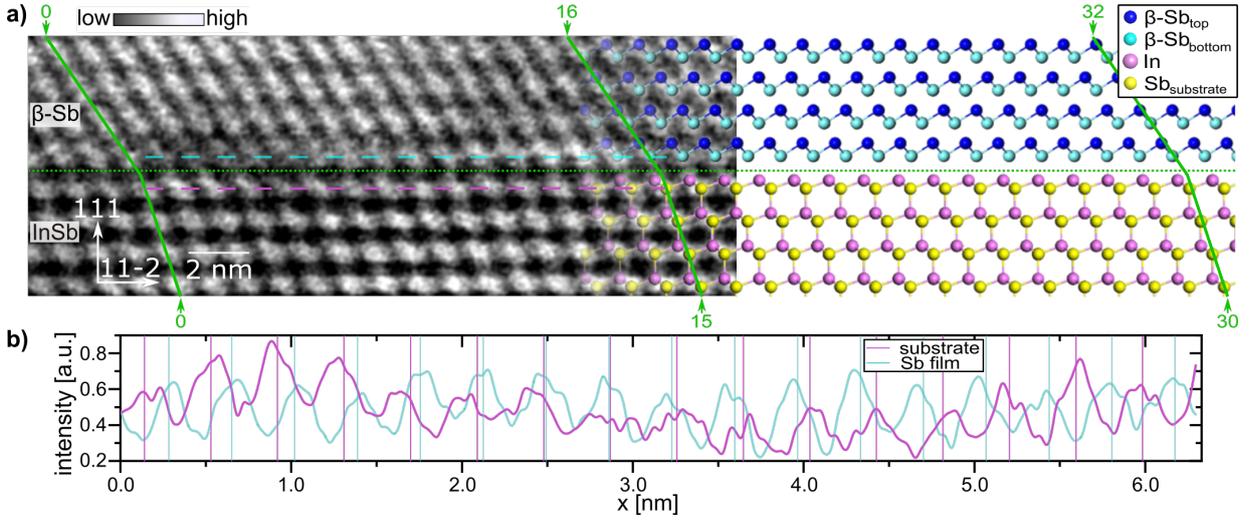
Figure 4.3: *a) Cross-sectional HAADF-STEM image of the Sb-InSb(111)A interface overlayed with the relaxed atomic structures of bulk Sb and InSb(111) [24]. The interface between substrate and Sb film is marked by a dotted line. Sb does not adapt to the substrate lattice constant at the interface but keeps its bulk lattice constant. The stacking sequence between both lattices repeats every 16 unit cells of Sb which match in distance to 15 unit cells of InSb(111). b) Line profiles along the first Sb bilayer and substrate surface layer of the STEM image in a). Vertical lines mark atomic positions. The positions of Sb atoms shift continuously relative to the substrate. c) Atomic model of the moiré unit cell in top view considering only the surface layer of the substrate and 1 BL of Sb. High symmetry sites are labeled according to the notation used for bilayer graphene and TMDCs [98, 99]. d) Local stacking sequence [24] of each high-symmetry site whereby the substrate lattice is compressed to the lattice constant of the Sb layers to achieve a computationally feasible primitive 1×1 unit cell for DFT calculations.*

layer, the substrate shows the atomic structure of its bulk configuration without indications that an intrinsic InSb(111)A surface reconstruction is still present after Sb growth. The interaction between Sb film and InSb(111) therefore cracks the 2×2 reconstruction that was present before Sb growth and stabilizes the unreconstructed 1×1 InSb(111)A surface. Regarding the Sb film, it is apparent that not even the first Sb layer adapts the periodicity of the substrate. Instead, atomic positions of the first Sb BL shift continuously relative to those of the substrate surface layer, as shown in line profiles in figure 4.3 b). The relative alignment thereby periodically repeats itself after 16 (15) unit cells of Sb (InSb). The distance covered by the multiples of both lattice constants matches to the observed moiré periodicity of (6.85 ± 0.10) nm in STM, suggesting a purely lattice mismatch-driven root cause. This assumption is further supported by the fact that the atomic lattices of Sb film and substrate are simultaneously resolved in the STEM image in a distinct manner which contradicts a rotational misalignment. Additionally, the rotational alignment of Sb film
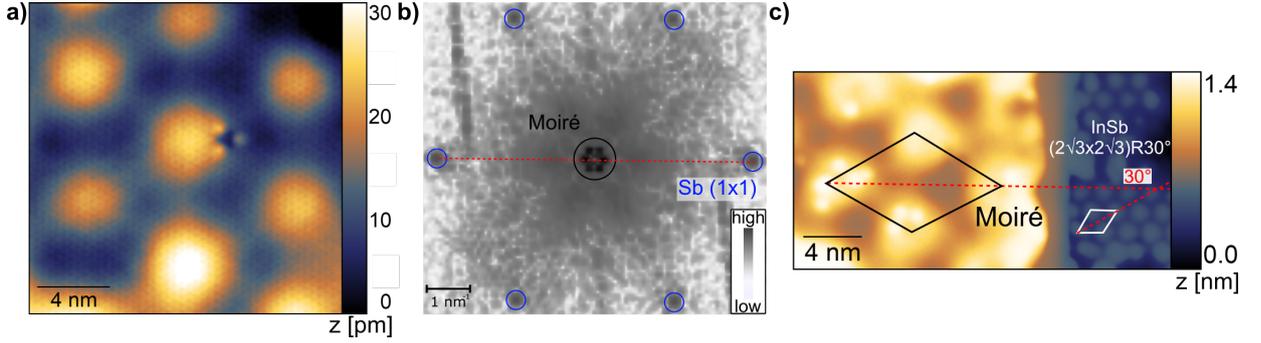
Figure 4.4: *a) STM image (1.0 V, 10 pA) of several moiré unit cells including atomic resolution. b) Fourier transformation of the STM image in a) shows a rotational alignment of the spots of the atomic lattice of Sb with those of the moiré superstructure that forms a hexagonal feature in the center. c) STM image (1.0 V, 20 pA) that shows the moiré unit cell alongside the $(2\sqrt{3} \times 2\sqrt{3})R30°$ reconstruction of the substrate. Red lines in b) and c) visualize the relative alignment of the lattices.*

and substrate can be verified by STM, see figure 4.4. Figure 4.4 a) shows an atomically resolved STM image of the Sb film including the moiré superstructure. Its Fourier transform in figure 4.4 b) allows to deduce that both, the atomic Sb lattice as well as the superstructure, share the same alignment. Figure 4.4 c) allows to confirm the alignment of the superstructure lattice to that of the reconstructed InSb(111) substrate. The 30° angle between both lattices is present due to the rotation of the substrates $(2\sqrt{3} \times 2\sqrt{3})R30°$ surface which is rotated by 30° with respect to the primitive substrate unit cell. In combination, both datasets shown in figure 4.4 confirm the absence of a rotational misalignment between Sb film and substrate.

A schematic atomic model of the moiré unit cell, limited to the substrate surface layer and a single Sb BL, is depicted in figure 4.5 a). It shows three high-symmetry sites labeled AA, AB_{In} and AB_{Sb}. This notation is adapted from that used for bilayer graphene and TMDCs [98,99] and denotes in their index which atom species of the substrate lattice is uncovered by the upper lattice in top view. For AA, the atomic positions of both lattices match while for AB_{In} (AB_{Sb}), In (Sb) atoms of the substrate are positioned laterally in the center of a buckled hexagon of the Sb film.

The observability of the moiré pattern in STM raises the question whether the lattice mismatch at the interface manifests in a modulation of the surface corrugation and/or in a periodic charge accumulation. To address this issue theoretically, the properties of the system are calculated by DFT in a local approximation [94]. Within this approach, relaxed atomic models in primitive 1×1 unit cells are considered for which the lattice

constant of the substrate is reduced to follow the periodicity of the Sb film. As the moiré unit cell comprises arbitrary registry shifts between both lattices, DFT calculations have been performed for various interface alignments including all three high-symmetry points for which atomic models are displayed in figure 4.5 b). The results, shown in the following, therefore only represent a local picture of the moiré unit cell and exclude interactions between different stacking configurations and long-range moiré physics. This approach circumvents the simulation of the entire moiré unit cell which is computationally out of reach for systematic brute-force ab-initio simulations.
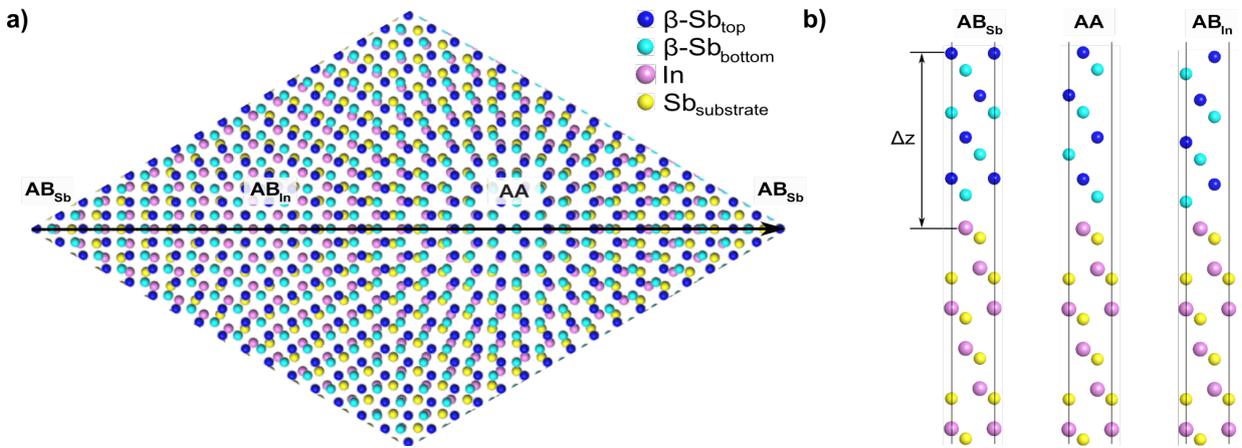
Figure 4.5: a) *Atomic model of the moiré unit cell in top view considering only the surface layer of the substrate and 1 BL of Sb. High symmetry sites are labeled according to the notation used for bilayer graphene and TMDCs [98,99]. b) Local stacking sequence [24] of each high-symmetry site whereby the substrate lattice is compressed to the lattice constant of the Sb layers to achieve a computationally feasible primitive 1×1 unit cell for DFT calculations.*

Figure 4.6 a) displays the height corrugation Δz of the upwards buckled Sb atoms of a 1 BL Sb film relative to the position of surface In atoms [visualized in figure 4.5 b)]. Each data point corresponds to the height corrugation obtained for a specific alignment of Sb and InSb lattices along the black arrow shown in figure 4.5 a) that spans the entire moiré unit cell. The height variations are calculated either for a unit cell size strained to the lattice constant of the substrate (green), to the lattice constant of the Sb layers (black) or an intermediate value (red, blue). Overall, all graphs show a similar shape with a minimum at site AB_{In} and a maximum at site AA. Increasing the thickness of the Sb island does not drastically change the expected height variation as shown for a 4 BL Sb film in figure 4.6 b).
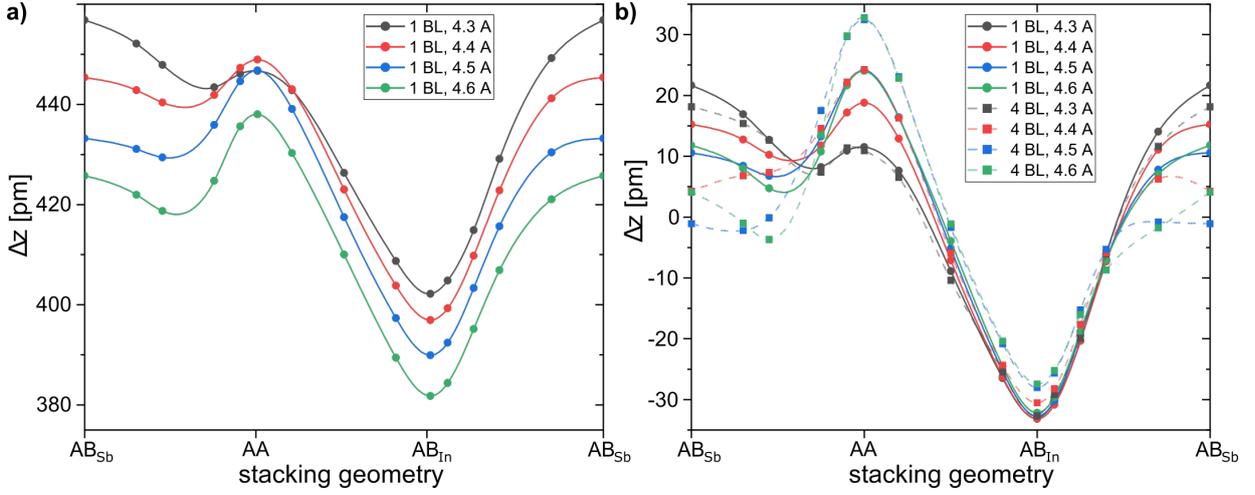
Figure 4.6: a) *Calculated height profiles of 1 BL Sb for depending on the lattice constant at different interface alignments following the path marked by an arrow in figure 4.3 b) [94]. b) Comparison of the calculated height trends for 1 BL (solid) and 4 BL (dashed) reveals that the overall height trend persists across several BLs [94]. Profiles are offset by their respective average to allow a better comparison.*
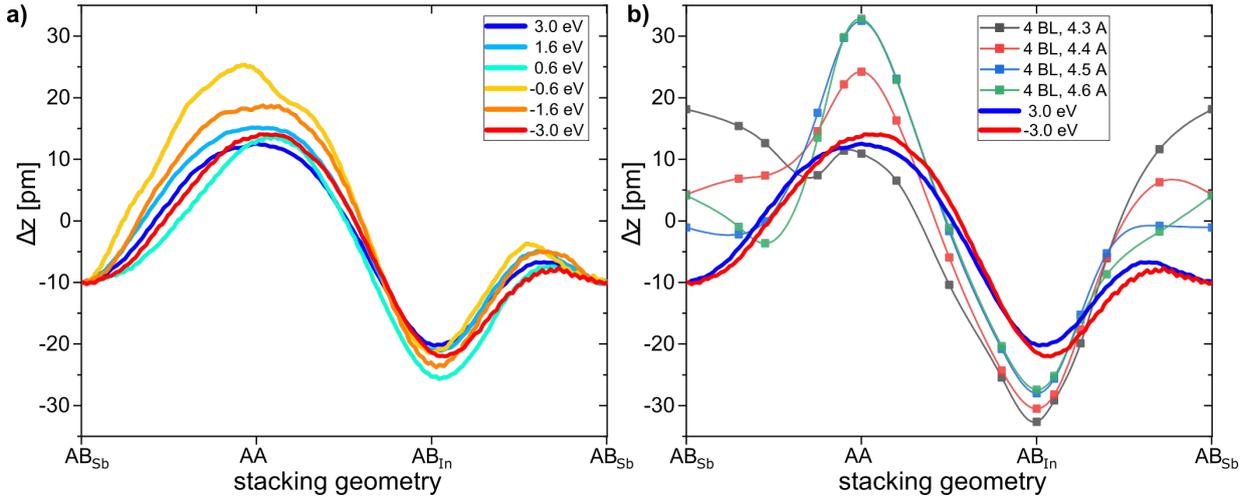
Figure 4.7: a) *STM height profiles taken across high symmetry sites of the moiré unit cell on a 4 BL Sb island. Profiles are shifted to match at position AB_{Sb} for better comparison. The overall height trend is independent of the tunneling voltage. b) Comparison of calculated and experimental height profiles for 4 BL of Sb. Height trends match qualitatively and indicate a manifestation of the moiré situation at the interface in a periodic surface corrugation.*

Figure 4.7 a) shows the experimentally obtained height trends on a 4 BL Sb island as obtained with STM for different tunneling voltages. The height trend is almost independent of the chosen voltage except for a small height increase at position AA for low binding energies. This indicates that the height trend is not dominated by LDOS variations,

but mainly stems from a surface corrugation of the Sb islands. Figure 4.7 b) overlays experimental and theoretical height trends for a 4 BL Sb island. The overall trend is well reproduced by experiment and even shows an amplitude comparable to theory. The agreement between theory and experiment supports the assumption of a surface corrugation of the Sb islands which is driven by the varying interplay of both lattices at the interface. At the same time, it validates the local approach for theoretical analysis which does not take into account long-range moiré interactions.

4.3 Mechanism behind moiré formation

The observation of a lattice mismatch-induced moiré situation at the interface of an epitaxial film with a covalent substrate is rather unusual. Typically, surface lattices of adatoms saturate dangling bonds of covalent surfaces thereby lowering the surface energy while simultaneously adapting the substrates lattice constant [13, 92, 93]. For Sb, an unstrained growth on a covalent substrate has already been observed on Ge(111) [40]. The authors attribute their observation to weak interface interactions and suggest the absence of covalent bonds at the interface. Additionally, an unusual growth mode has been reported for bismuth - another group 15 element - on the Sb-terminated InSb(111)B surface [100]. Similar to antimony, the resulting bismuth lattice does not adapt to the InSb(111) lattice but relieves strain by forming an exotic Sierpiński structure. Both observations can be attributed to the large lattice mismatch of the adlayers with the substrate and the pseudo-layered structure of Sb and Bi bulk lattices in (111) direction. The strong intra-layer bonds of the buckled Sb/Bi-BLs [101] favor bonds within the adlayer during growth while the weaker inter-layer interaction between substrate and adatom layers is insufficient to strain the films to the larger substrate lattice. For this system of Sb films on InSb(111)A, we find that the strained growth is indeed energetically unfavorable by analyzing all relevant energies involved in the growth of the Sb islands.

On the one hand, a strained growth of Sb on InSb(111) requires energy to elongate the Sb-Sb bonds of the Sb bilayers and reduce the intrinsic buckling of the bilayer. On the other hand, the interface interaction between Sb film and substrate lowers the total energy of the system. Depending on which energy scale dominates, one can either expect a strained growth or an attempt of the film to somehow relieve the strain, e.g., by forming a moiré interface. Figure 4.8 a) displays the energy required to strain free-standing Sb films of
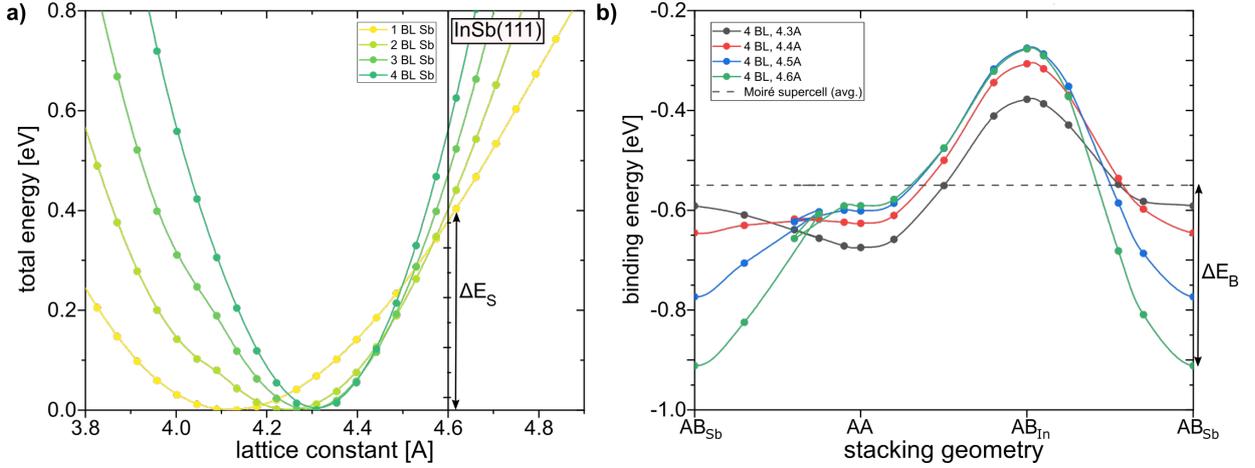
Figure 4.8: *a) Total energy required to strain 1-4 BLs of free-standing Sb to specific lattice constants [94]. Straining to the lattice constant of InSb(111) requires an energy of about 0.4 eV for 1 BL which increases with thickness. b) Alignment-dependent binding energies of 4 BL Sb on 6 layers of InSb(111) calculated for different unit cell sizes [94]. The dashed line represents an estimate for the binding energy of the moiré unit cell with a 4.3 Å lattice constant. Even for the energetically most favorable strained growth in the AB_{Sb} stacking sequence, the binding energy gain ΔE_B is smaller than the required energy ΔE_S to strain the Sb layers to the substrate lattice constant.*

different thicknesses to a specific lattice constant. The energetically most favorable lattice constant thereby increases with thickness towards that of bulk Sb(111), namely 0.43 nm. Straining the Sb film to the lattice constant of InSb(111) (0.46 nm) requires an energy ΔE_S of 0.4 eV for a 1 BL film and increases to 0.55 eV for 4 Sb BLs. The complementary energy gain of the combined film-substrate system due to interface interactions is shown locally resolved for various interface alignments and different lattice constants in figure 4.8 b) for a 4 BL film. Considering a primitive 1×1 unit cell of Sb-InSb(111) with the Sb bulk lattice constant allows to approximate the average energy gain inside of a moiré unit cell to -0.55 eV, within the limits of the local approach taken by DFT. For this approximation, the energy gain obtained for specific stacking configurations along the black line in figure 4.3 c) has been averaged. This value can be taken as a reference to determine the relative energy gain of strained films with a specific stacking geometry compared to the unstrained moiré growth. In general, the interface alignment at position AB_{In} is found to be energetically least favorable. On the other hand, the strongest energy gain is obtained for the AB_{Sb} stacking. It increases with the lattice constant of the primitive unit cell under consideration. Strained to the lattice constant of the substrate, the lowest possible binding energy of a 4 BL Sb film is found to be -0.91 eV in AB_{Sb} sequence. This translates into a maximal energy gain of $\Delta E_B = -0.36$ eV for a strained 4 Sb BL film relative to the

unstrained growth. The strained growth of the 4 BL film, however, requires an additional energy of at least 0.4 eV, as stated before. The total energy of the strained Sb film on the InSb(111) substrate is therefore higher than that of the unstrained moiré system. It is therefore energetically favorable for the Sb film to avoid a strained growth and, instead, keep its intrinsic bulk lattice structure, even for low layer thicknesses.

4.4 Thickness-dependent electronic properties

4.4.1 Local band structure calculations

Having established an understanding of the moiré supercell, the implications of the local stacking configurations on the electronic properties will be investigated. For comparison, the band structure of a free-standing Sb film of 10 BL thickness which is almost identical to the bulk band structure, is shown in figure 4.10 c). Its main feature is the spin-polarized topological non-trivial surface state with a strongly distorted Dirac cone at Γ connecting valence and conduction band. Figure 4.9 shows DFT calculated band structures along high-symmetry sites for different thicknesses of the Sb film and for all three high-symmetry stacking configurations [94]. The point size thereby represents the projection weights for the antimony atoms in the film and the color visualizes the projection weights for Sb states on opposite sides of the Sb film, the interface to the substrate (red) and the surface (yellow).

The presence of the InSb(111)A substrate separates the surface and interface states of the Sb film as visible in the 5 BL case in figure 4.9 for all stacking configurations under investigation. For AA and AB_{In}, the interface state is pulled towards lower binding energies and even to the unoccupied states for AB_{In} compared to the surface state binding energy. With decreasing thickness, the interface states remain rather fixed in energy while the surface states shift upwards in energy as they increasingly start to 'feel' the substrate. Below a thickness of 4 BL, electrons may tunnel between states on opposite sites of the Sb film which opens band gaps at intersections of the topological non-trivial interface and surface state at and around Γ [94]. This thickness-dependent behavior is representative for most other stacking configurations present in the moiré supercell. A local exception is only found regarding the AB_{Sb} geometry for which the interface state is located at higher binding energies than the surface state. Both states shift downwards in energy with
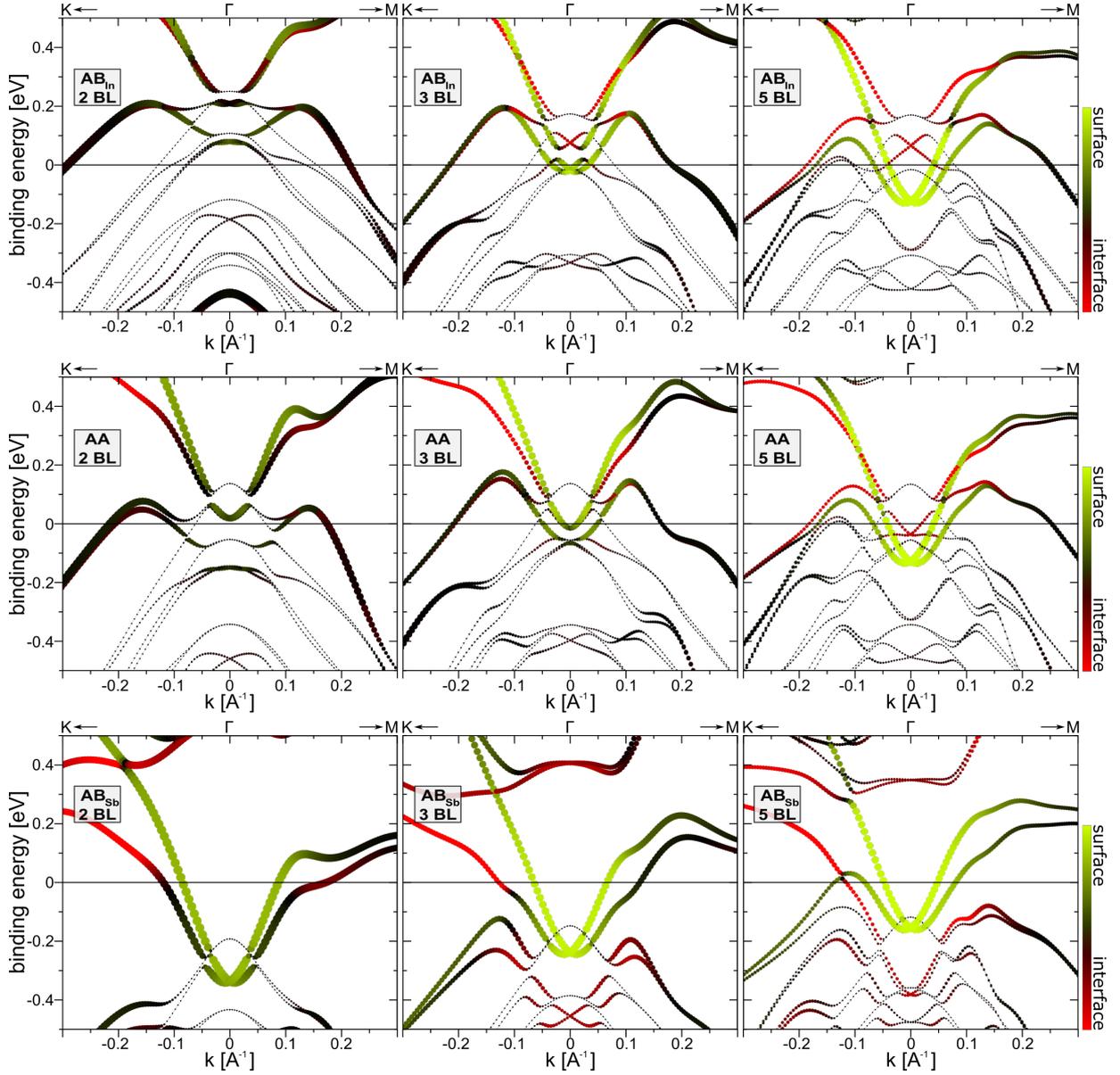
Figure 4.9: *DFT calculated band structures [94] of 2 BL, 3 BL and 5 BL of Sb on InSb(111) along K-Γ-M directions for the high-symmetry stacking sites AB_{In}, AA and AB_{Sb}. Colors represent projection weights onto surface (yellow) and interface (red) states of the Sb films. The point sizes indicates projection weights onto all Sb atoms of the film. For AB_{In} and AA (AB_{Sb}), the surface state shifts towards lower (higher) binding energies with decreasing thickness.*

decreasing thickness which prevents the opening of a hybridization gap at Γ. A local band gap is only opened between Γ and K below a thickness of 5 BL. The exceptional case of position AB_{Sb} can be attributed to a particularly enhanced film-substrate interaction for this stacking configuration as it features the smallest distance between atoms of substrate

bond length [nm]	AA	AB_{In}	AB_{Sb}
$Sb_{bottom}-In$	0.383	0.350	0.295
$Sb_{bottom}-Sb$	0.377	0.417	0.461
$Sb_{bottom}-Sb_{top}$	0.299	0.298	0.294

Table 4.1: *Bond length at the interface between the first Sb layer and the top layer of the substrate. Sb_{bottom} (Sb_{top}) is the bottom (top) Sb atom of the first Sb layer within their buckled honeycomb structure, and In (Sb) is the In (Sb) atom of the top InSb(111)A layer.*

and Sb film compared to other positions, see table 4.1.

The observation of a substrate-induced separation of the surface and interface state has also been observed for $Sb-Bi_2Te_2Se$ [37] and Sb on Bi-terminated Si(111) [102]. Kim *et al.* show that this separation can be simulated by applying an electric field perpendicular to a free-standing Sb film. The energy separation prohibits the tunneling of electrons between states on opposite surfaces as energy conservation is no longer preserved and prevents the opening of a tunneling-induced gap. Bian *et al.* [102] suggest that the energy separation should become even more pronounced with decreasing thickness which is in contrast to our DFT [94] study that predominantly observes a smaller separation with hybridization between both inter- and surface states.

4.4.2 Quasi-particle interference measurements

ARPES measurements experimentally confirm the bulk-like topological surface states around Γ for thick layers of Sb on InSb(111), see figure 4.10 a). Hole pockets of the surface state along Γ-M thereby form a three-fold symmetric pattern at the Fermi surface (figure 4.10 b)), in good agreement with the ARPES data reported by Sugawara *et al.* [104] for bulk Sb(111). A thickness-dependent experimental investigation of the electronic structure is, however, out of reach for photoemission techniques. The 3D growth of the Sb islands on InSb(111) requires a hitherto unrealized lateral resolution of the beam spot of ≤ 20 nm to measure single height film thicknesses. We therefore use the resolution advantages of the STM for the thickness-dependent investigation of the electronic structure.

With STS providing momentum-averaged information about the LDOS of the system, the behavior of the surface state Dirac cone cannot be probed directly but requires a more elaborate approach. We therefore adapt a quasiparticle interference (QPI) method
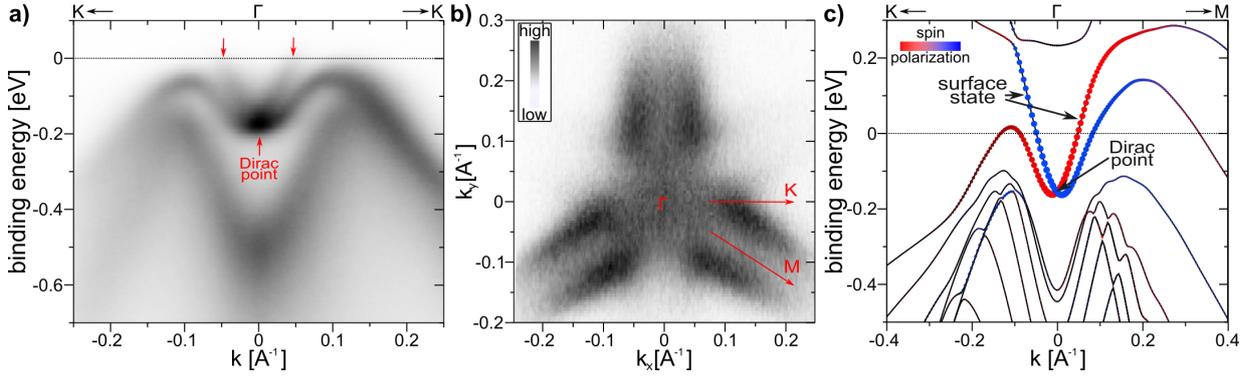
Figure 4.10: a*) ARPES band structure measurement along K-Γ-K for thick Sb layers (>10 BL) on InSb(111)A. The metallic surface state (red arrows) and the Dirac crossing at Γ are nicely resolved. b) Fermi surface around Γ. The three-fold symmetry indicates that the surface state is not only confined to the six-fold symmetric surface layer but penetrates the three-fold symmetric rhombohedral bulk structure [103]. c) DFT calculated band structure of a 10 BL free-standing Sb film along K-Γ-M. The surface state is spin-polarized as indicated by the colors. The point size indicates the strength of the surface state character. Adapted from [94]*

previously applied to the bulk surface of Sb(111) by Seo *et al.* [105]. This method utilizes the standing wave interference pattern of the Sb surface state generated by the scattering at atomic step edges. The energy-dependent periodicity of the pattern thereby correlates to the dispersion relation of the surface state. The scattering wave vector $q(E)$ between incoming and reflected electrons can be obtained by a Fourier-transform of the real space signal. It is mathematically defined by

$$q(E_n) = k_i(E_n) - k_f(E_n) \tag{4.1}$$

with k_i and k_f describing the respective initial and final momentum state of an elastic scattering event at the step edge at energy E_n. Due to the topological nature of the Sb surface state, scattering between states of orthogonal spin is forbidden. This simplifies the interference pattern and reduces the scattering to events with scattering vectors q_A and q_B. The relevant scattering vector for this analysis is q_B which connects states with opposite momenta within the surface state, visualized in the inset of figure 4.11 b). It is thereby sufficient to consider scattering processes along Γ-M as this scattering direction is predetermined by the edges of the triangular Sb islands. The energy minimum at which scattering is observed marks the energy of the Dirac crossing at Γ and allows to trace its thickness-dependent behavior. Due to a finite terrace width L - given by the separation of adjacent parallel step edges - the observed scattering vector is additionally quantized to

values with a multiple of $\frac{2\pi}{L}$.
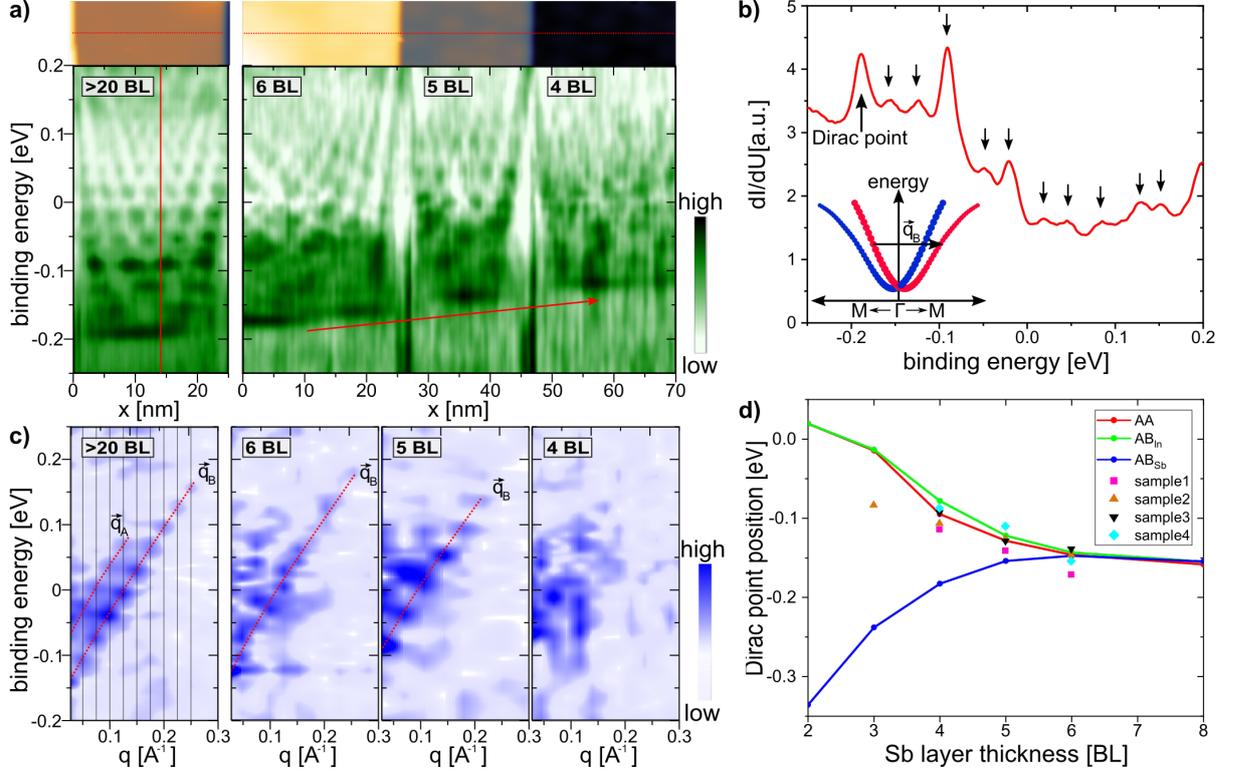
Figure 4.11: *a) Spatially resolved spectra taken across Sb terraces of various thicknesses along the lines, shown above in the STM topography images. The interference pattern arises due to the scattering of the surface state on neighboring parallel terrace edges. With decreasing thickness, the Dirac point position shifts towards lower binding energies. b) Spectra visualizing the energy discretization induced by the spatial confinement to the terrace width. Inset: Schematic of the surface state with scattering vector q_B between states with identical spin. c) Fourier transform of the data in a) shows the thickness-dependent dispersion of q_A and q_B (including red lines that serve as guide to the eyes). d) Thickness-dependent shift of the Dirac point position for measurements taken on different samples compared to that predicted by band structure data for interface alignments of all high-symmetry sites. A good agreement to the experimental data is obtained for sites AB_{In} and AA.*

In experiment, STS measurements were obtained along a line perpendicular to adjacent step edges to achieve the energy-dependent interference pattern of the surface state in real space, see figure 4.11 a). For a thick Sb island (>20 BL), the observed pattern is identical to that reported by Seo *et al.* [105] for bulk Sb, albeit shifted to lower binding energies by about 35 meV, see left part of figure 4.11 a). The Fourier transform of this interference pattern allows to extract the contributing scattering vectors, see figure 4.11 c). Both scattering vectors, q_A and q_B, are well resolved and show the expected quantized behavior with multiples of $\frac{2\pi}{L}$ as indicated by equidistant black lines in the leftmost panel of 4.11

c). As a quantization in momentum naturally implies a quantization in energy, single STS spectra similarly show a distinct array of peaks above the Dirac cone energy at -193 meV[2], exemplary displayed in figure 4.11 b). Taking a look at data obtained on Sb islands of lower thicknesses ($6-4$ BL) still reveals an interference pattern of the surface state, see right panel of figure 4.11 a). The measurements, however, become fuzzier with decreasing thickness and the interference patterns less pronounced against the background intensity. This naturally translates into momentum space to the QPI patterns for which scattering vectors become increasingly difficult to assign. A possible explanation for the loss in signal could be the increasing influence of the moiré superstructure on the electronic properties as it becomes more pronounced with decreasing thickness. As shown in figure 4.6 c), additional charge is accumulated locally at AA sites at low binding energies - the position of the surface state. A periodic potential created by these charge accumulations might generate additional scattering centers for the surface state thereby making the interference pattern more complex and diffuse.

Nonetheless, the real space data in figure 4.11 a) allows to extract a shift of the interference pattern onset towards lower binding energies for decreasing thicknesses. The onset is found at -172meV, -143 meV[3] and -115 meV for 6, 5 and 4 BL, respectively. This thickness-dependent trend of the Dirac cone is a consistent feature among datasets taken on different samples, see figure 4.11 d). Despite small variations between datasets, the experimental trend matches well with that predicted by DFT for local sites AA and AB_{In} and unambiguously contradicts the trend expected for site AB_{Sb}. Unfortunately, no solid data could be obtained to follow this trend experimentally down to 2 BL or 1 BL due to the decreasing signal strength of the interference pattern and sparsity of parallel edges.

Overall, we were able to trace the surface state down to an Sb film thickness of at least 3 BL by QPI measurements. With decreasing thickness, the Dirac cone shifts towards lower binding energies. This observation is in agreement with the local properties expected for most interface alignments of the moiré unit cell, including sites AA and AB_{In}, according to DFT [94]. It can therefore be assumed that, despite the local approach in DFT calculations, the overall electronic properties of the moiré supercell follow the general properties of these two high-symmetry sites. Whether the predicted opening of a hybridization gap below 4 BL results in a topological trivial or non-trivial gap has yet to be determined theoretically and experimentally.

---

[2]corrected by -3 meV due to the confinement-driven quantization ($L = 25$ nm)
[3]corrected by -8 meV due to the confinement-driven quantization ($L = 20$ nm)

4.5 Conclusion

We successfully synthesized high-quality Sb films on an insulating InSb(111)A substrate with thicknesses down to the monolayer limit. Despite a covalent substrate surface, the Sb layers do not grow epitaxially strained but keep their bulk lattice constant. As a consequence, the lattice mismatch at the interface induces a moiré superstructure with a 6.85 nm unit cell. The rather unusual unstrained growth of Sb on a covalent substrate can be explained with the large energy required to strain the Sb films that outweighs the corresponding gain in binding energy. The moiré pattern manifests mainly in a surface corrugation of the Sb film which gets additionally enhanced in STM in the occupied states at low binding energies by a local charge accumulation on AA sites. The Dirac point of the Sb surface state shifts towards lower binding energies with decreasing thickness, in agreement with theoretical predictions obtained from local band structure calculations for most interface alignments of the moiré unit cell. According to DFT, this shift corresponds to a Sb band structure that undergoes a thickness-dependent phase transition from a 3D TI to a potentially topological non-trivial 2D insulating state which, however, has yet to be determined.

This work establishes an understanding for the underlying mechanisms behind the moiré growth of Sb on InSb(111)A and the general thickness-dependent electronic properties of the Sb films. Experimentally, the biggest challenge to be tackled in the future is the non-uniform thickness of Sb islands which prevents the meaningful application of averaging techniques, such as ARPES, to directly investigate the momentum-dependent electronic structure thickness-dependent. As no systematic dependency between growth parameters and island size could be observed it is questionable if the InSb(111)A substrate is the right candidate to tackle this problem. Theoretically, calculations have so far only been done within a purely local picture without taking into account potential electronic long-range correlations inside the moiré unit cell. Their presence is, however, experimentally confirmed with the observation of local charge accumulations at AA sites. While the Sb-InSb(111)A system provides an interesting mixture and interplay of exotic phenomena, including non-trivial topology and moiré physics, the very same properties complicate its investigation by experiment and theory.

5 Surface reconstructions of Sb on SiC(0001)

Besides InSb(111), the (0001) surface of the large-gap semiconductor SiC offers a promising template for the epitaxial growth of topologically non-trivial monolayer phases of antimony. Its three-fold symmetric covalent surface, schematically shown for the 4H-SiC polymorph in figure 5.1 a), is proposed in literature as an adequate substrate to host either a planar hexagonal $(\sqrt{3} \times \sqrt{3})R30°$ [51, 106] or triangular 1×1 [107] lattice of antimony according to theoretical simulations. The band gap of 3.27 eV (4H-SiC) [108] around the Fermi level thereby isolates low-energy states of an adlayer from the electronic states of the substrate.

The planar $(\sqrt{3} \times \sqrt{3})R30°$ honeycomb lattice of Sb on SiC(0001) features a unit cell size of 5.35 Å [51, 106] which induces an enormous strain of 24% on the antimonene lattice. According to literature [44–46] this strain would be sufficient to drive a phase transition to a topological non-trivial phase for a free-standing lattice. On SiC(0001), however, the presence of the substrate is expected to alter the electronic structure to resemble that of graphene with Dirac cones at each K point, similar to the case of bismuthene/SiC(0001) [13, 33, 51]. In this case, the covalent bonding to the substrate allows for a large on-site spin-orbit coupling (SOC) that would open a topological band gap of about 0.3 eV [51]. In combination with the reported stability of antimony lattices under atmospheric conditions [38–40, 109], the realization of a room-temperature topological antimonene lattice would promise excellent properties for future device applications.

The triangular Sb-(1×1) lattice, on the other hand, is proposed by Wang *et al.* within a global study on 2D metal films on SiC [107]. They report the formation energies for different coverages of Sb on SiC(0001), among those for many other elements, ranging from 0.33 monolayer (ML) to 2.66 ML. The formation energy of a 1×1 reconstruction in which Sb atoms sit atop each surface Si atom (1 ML coverage) is found to be about 130 meV lower than that of a planar graphene-like honeycomb lattice of antimony (0.66 ML

coverage), as proposed by other groups [51, 106]. The structural and electronic properties are expected to be similar to those of indenene, a triangular lattice of In on SiC(0001), which was realized by Bauernfeind *et al.* [93]. The group experimentally confirmed the topologically non-trivial character of their material with a band gap of 125 meV in the occupied states. Owing to the higher electron count of Sb compared to In, the overall band structure of a triangular Sb lattice is predicted to be shifted towards higher binding energies, moving the Dirac cone deeper into the occupied states.

In this chapter, we report on the preparation of two novel Sb-induced surface reconstructions on SiC(0001), a triangular Sb-(1×1), as proposed by Wang *et al.* [107] and a kagome-like Sb-(2×2). Combining experimental (STM, ARPES and STEM) and theoretical techniques (DFT), both lattices are identified on the basis of their structural and electronic properties. The following section reports on the properties of the Sb-(1×1), an indenene-analogue buried below an Sb adlayer. The subsequent section focuses on the investigation of the asymmetric Sb-(2×2) kagome lattice, constituting the first realization of an elemental surface kagome structure to date. All DFT calculations shown in this chapter have been provided by the research group of Giorgio Sangiovanni from Julius-Maximilians-Universität Würzburg with the main work performed by Philipp Eck.

5.1 Buried triangular Sb-(1×1) lattice

5.1.1 Surface preparation

As substrate, we use the commercially available n-doped 4H-SiC(0001) polymorph with Si termination. Initially, samples are cleaned *ex-situ* from a protective photoresist in an ultrasonic bath with organic solvents (acetone, isopropanol, methanol). A well-defined (0001) surface is then achieved *in-situ* by etching the topmost atomic layers at high temperature in a H-reactor specifically designed for the SiC preparation [110]. After etching, hydrogen atoms saturate the dangling bonds of the surface Si and render the unreconstructed SiC(0001) 1×1 surface suitable for the epitaxial growth of adatoms [111]. The presence of the 1×1 reconstruction of the clean substrate can be verified by means of LEED, shown in figure 5.1 b). An atomic model of the unreconstructed SiC(0001) surface, without H-termination, is shown in figure 5.1 a). The surface layer consists of a buckled SiC bilayer with Si atoms terminating the surface. They form a triangular lattice and provide dangling

bonds for the epitaxial growth of adatoms. Due to the presence of carbon atoms in the surface layer, the six-fold symmetry of the Si atoms is reduced to an overall three-fold symmetry of the surface layer. The three high symmetry adsorption sites of the lattice are labeled T1 (atop surface Si atoms), T4 (atop surface C atoms) and H3 (inside surface honeycomb).
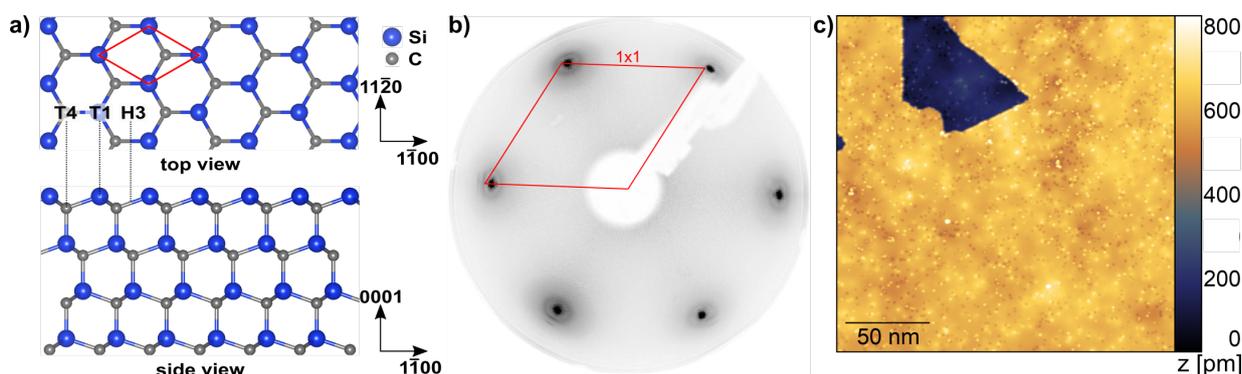
Figure 5.1: a) *Atomic model [24] of the SiC(0001) surface. For clarity, the top view is limited to the atoms of the surface layer. High-symmetry adsorption sites are labeled accordingly. b) LEED (55 eV) confirms the presence of an unreconstructed surface layer with 1 × 1 periodicity. c) STM topography image (+3.0 V, 10 pA) of a H-terminated SiC(0001) surface after etching showing an atomically flat terrace with point defects.*

STM topography images of as prepared H-terminated SiC(0001) surfaces consist of large atomically flat terraces, as can be seen in figure 5.1 c). Irregularities in the surface can be attributed to subsurface dopant atoms and point defects. They do, however, not impede a high quality adsorbate layer growth as proven for bismuthene or indenene [13,93]. To avoid a temperature-driven surface reconstruction [111] of the substrate during Sb growth, highly pure Sb (99.9999%) was offered via an effusion cell simultaneously to the thermal desorption of hydrogen at $\approx 600°$C. Thus, dangling bonds of hydrogen-free Si atoms are immediately saturated by Sb atoms and the irrevocable intrinsic Si-rich surface reconstruction of the SiC(0001) surface is avoided. To ensure a sufficient Sb coverage, evaporation was continued several minutes beyond the thermal desorption step of hydrogen until the sample was cooled down to room temperature. Excess Sb was subsequently removed from the surface by an anneal of the sample to 350°C.
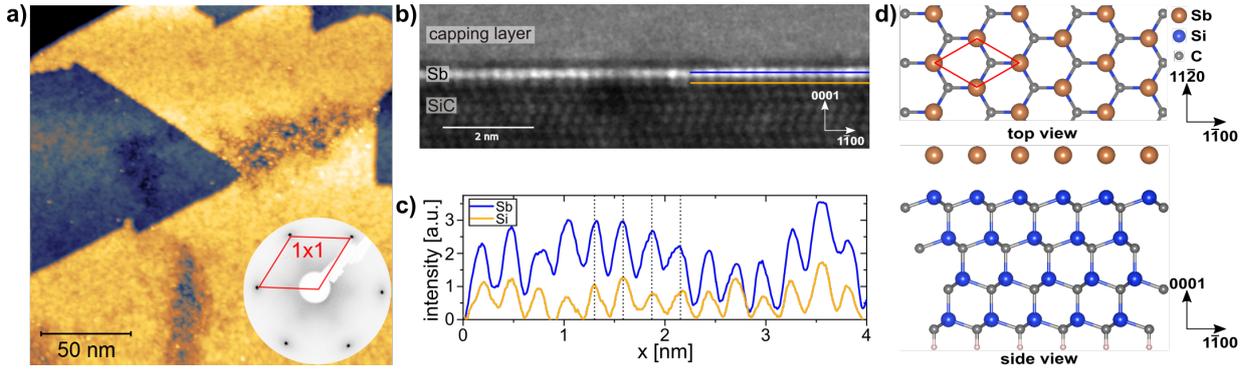
Figure 5.2: a*) STM topography image (+3.0 V, 10 pA) of the SiC(0001) surface after Sb evaporation and low-temperature anneal showing no regular order of Sb. Inset: LEED measurement of the surface showing spots of a 1×1 reconstruction. b) Cross-sectional HAADF-STEM image of the Sb-SiC(0001) interface reveals an ordered monolayer of Sb on top of the substrate surface. d) Profiles along lines marked in c) reveal that the adsorption site of Sb atoms is atop of the surface Si atoms, similar to indenene [93]. d) Atomic model [24] of the Sb-(1×1) in T1 position. For clarity, the top view is limited to the substrate atoms of the surface layer.*

5.1.2 Structural characterization of the Sb-(1×1) SiC(0001) surface

Investigation of the as-grown sample with STM reveals an inhomogeneous surface without any regular order and a simple diffraction pattern of a 1×1 reconstruction in LEED, see figure 5.2 a). At a first glance, this could indicate that no epitaxial Sb growth has taken place and the observed LEED pattern solely results from the lattice structure of the substrate. STEM measurements[1] taken on a thin lamella of a Sb-SiC(0001) sample, however, reveal a bright, well-ordered monolayer of Sb at the substrate surface, see figure 5.2 b). Within the projection onto the $11\bar{2}0$ lattice plane, Sb atoms are located right above the Si atoms of the substrate surface layer. The Sb atoms thereby follow the periodicity of the substrate along direction ($1\bar{1}00$), as shown in line profiles in figure 5.2 c) taken along the Sb adlayer and the substrate surface layer. The lateral position of Sb atoms along the $11\bar{2}0$ e-beam direction cannot be deduced from this STEM measurement. The observation of a simple 1×1 reconstructions in LEED measurements nevertheless indicates the adsorption of Sb atoms on a high symmetry site of the SiC(0001) surface as they naturally follow the periodicity of the surface. This assumption singles out adsorption site T1 as it is the only site which is located above surface Si atoms within the perspective given by the STEM measurement. The corresponding Sb lattice model is shown in figure 5.2

---

[1]provided by Dr. Martin Kamp (Physikalisches Institut Julius-Maximilians-Universität Würzburg)

d). It matches the energetically most-favorable triangular lattice as proposed by Wang *et al.* [107]. Further support for this lattice structure is provided by the fact that the atomic lattices of related materials bismuthene/SiC(0001) and indenene/SiC(0001) also use the T1 site for adsorption [13, 93].

Interestingly though, we were not able to investigate the Sb lattice with STM as it was invariably covered by a disordered adlayer. The standard procedure to remove excess atoms, a sample anneal, is indeed able to remove the adlayer, as described in section 5.2.1, but additionally leads to a phase transition. As such, a detailed analysis with STM of the observed Sb lattice was not possible. As the surface was only exposed to Sb atoms during growth and a contamination of the effusion cell can be excluded, the adlayer is expected to consist of additional Sb atoms. It is debatable if the presence of this layer contributes to the stability of the underlying Sb lattice or if it is just strongly adsorbed and simply requires a thermal energy for desorption that surpasses the thermal stability of the regular Sb lattice. In both cases, it is surprising that the apparent interaction does not cause any regular order in the adlayer.

5.1.3 Electronic properties of the Sb-(1×1) SiC(0001) surface

While an investigation of the electronic properties of the Sb-induced surface with STS is not possible due to the inhomogeneous adlayer, ARPES measurements are able to probe the surface lattice underneath. The experimental band structure information can then be compared to theoretical data obtained with DFT calculations provided by the research group of Giorgio Sangiovanni from Julius-Maximilians-Universität Würzburg.

Experimental band structure of the Sb-(1×1)

Figure 5.3 a) shows the band structure of a Sb/SiC(0001) sample along high-symmetry paths of the Brillouin zone as obtained with ARPES at room-temperature. Due to the large band gap of SiC(0001), substrate bulk bands are located at high binding energies as depicted by dark colored bands in figure 5.4 a). They nevertheless show up as satellite features at lower binding energies due to the non-monochromatized He I light source of the ARPES setup. The hole-like features centered around $\Gamma_{1\times1}$ caused by He I β and He I γ light are neglected in the further analysis. As a general observation, the intensity of the
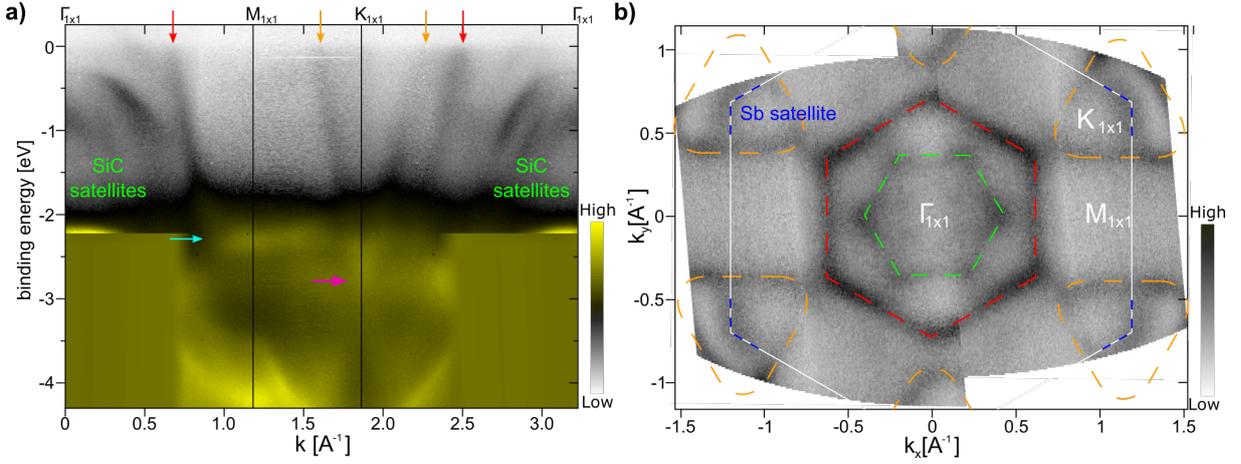
Figure 5.3: a) *ARPES band structure along high-symmetry paths on a Sb-(1 × 1) SiC(0001) sample consisting of several separate measurements (no data was measured around Γ for binding energies below −2.2 eV). Features centered around Γ are satellites of substrate bands located at higher binding energies. Sb-induced features are: four metallic band (red, orange), a flat band (cyan) and a Dirac-cone like band crossing (purple) at $K_{1 \times 1}$ (marked with arrows). b) Symmetrized CEC taken at −20 meV. Dashed lines schematically depict the shape of features with colors corresponding to arrows in a). Solid white lines depict the 1 × 1 Brillouin zone boundary. Intensity at $K_{1 \times 1}$ stems from He I satellites of Sb bands.*

remaining Sb-induced bands is rather weak, comparable to that of the before mentioned satellite features of the substrate, and broadened. This is unusual as the ARPES signal quality of monolayer materials with comparable cross sections is significantly higher [13,93]. Possible explanations are a low surface coverage of the Sb-(1 × 1) lattice below the adlayer or a broadening of bands due to the inhomogeneous interaction of the regular antimony lattice with the adlayer. While the signal quality of Sb bands does not allow to resolve fine details of the band structure, it enables the identification of several bands that can be attributed to the formation of a regular lattice of antimony. At low binding energies, four bands (indicated by red and orange arrows) cross the Fermi level and show steep, nearly linear dispersions. At a binding energy of about −2.3 eV, the metallic band crossing E_F between $\overline{\Gamma M}$ merges into a flat band that spans from $M_{1 \times 1}$ towards $K_{1 \times 1}$ (cyan arrow). Both steep bands marked orange keep their linear dispersion across the entire energy range and seem to cross each other at a binding energy of about −2.7 eV (purple arrow).

At the Fermi surface, the before mentioned metallic bands form two distinct features, depicted in figure 5.3 b) in form of a CEC taken at −20 meV. Firstly, a hexagonal shape with half the size of the 1×1 Brillouin zone surrounds $\Gamma_{1 \times 1}$. It almost perfectly traces the outline of the 2 × 2 Brillouin zone boundary with an experimental value of $k_{II} = 0.70 \pm 0.02$ Å^{-1}

along $\overline{\Gamma K}$ compared to the expected value for $K_{2\times2}$ of $k_{II} = 0.682$ Å^{-1}. Secondly, the metallic bands surrounding $K_{1\times1}$ form triangular shapes pointing towards the hexagonal shape in the Brillouin zone center. Intensity inside the triangles can be attributed to satellite features of Sb-induced bands from higher binding energies. The Fermi surface, consisting of a hexagonal feature around Γ and triangular features around K points, has the characteristic appearance of a circular (nearly) free-electron like band backfolded at the Brillouin zone boundary. It resembles the Fermi surface obtained on SiC(0001) covered with 2 MLs of In [112] albeit with an increased radius of the electron pockets. In this perspective, the steep metallic bands can be attributed to parabolic nearly free electron pockets. In contrast to the case of 2 ML indium, these bands seem to hybridize with flat bands near $M_{1\times1}$.

Theoretical band structure of the triangular Sb-(1×1) lattice
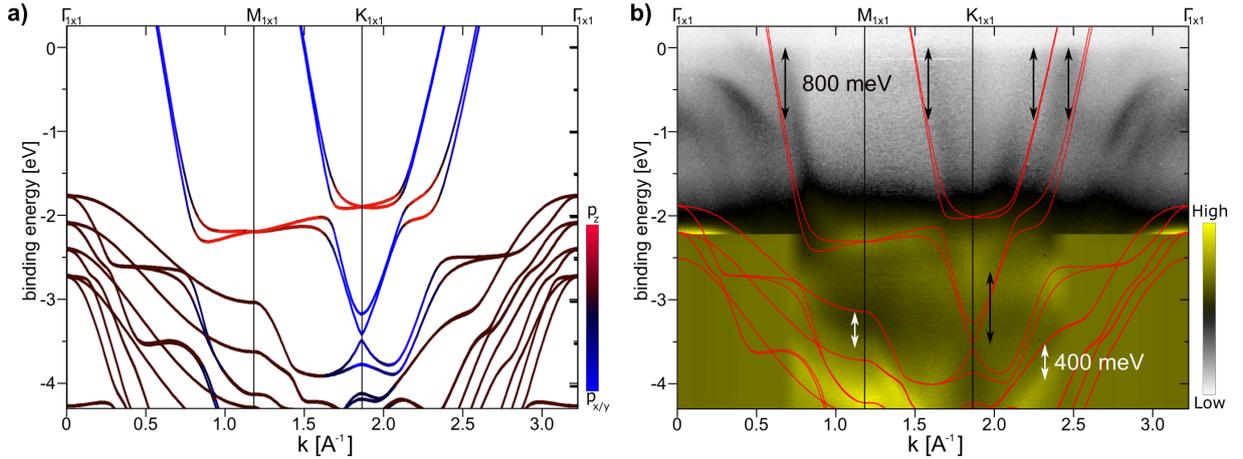
Figure 5.4: *a) DFT calculated band structure including SOC of the atomic model shown in figure 5.2 d). Blue and red colors denote the orbital character of Sb bands whereby black lines indicate substrate bands. b) ARPES band structure of figure 5.3 a) overlayed with the DFT band structure of a). Both datasets are aligned to match the energetic position of the flat band at $M_{1\times1}$.*

For comparison with experiment, figure 5.4 a) shows the DFT-derived band structure of the atomic model proposed in the previous section 5.1.2, displayed in figure 5.2 c). The band dispersion reproduces all features shown by Wang *et al.* [107], but additionally captures the influence of spin-orbit coupling. It generally resembles the band structure of the TI indenene [93] albeit with bands shifted towards higher binding energies, attributed to the higher electron count of antimony. Within the substrate band gap, four steep

metallic bands of $p_{x/y}$ character disperse down to higher binding energies, similar to the experimental observation. At about -2 eV they hybridize with a flat p_z band spanning most of the Brillouin zone. The hybridization between in- and out-of-plane orbitals is thereby induced by the presence of the substrate which breaks the mirror symmetry in z direction (parallel to the surface normal). At $K_{1\times1}$, two of these bands form an avoided crossing which results in a band gap of 70 meV at a binding energy of -3.4 eV.

There are two counteracting driving forces for this gap opening. On the one hand, the local SOC λ_{SOC} which depends on the atomic number and, on the other hand, a non-local term λ_{ISB} introduced by the inversion symmetry breaking (ISB) of the $C_{3\nu}$ symmetric SiC substrate. If the local SOC dominates over the ISB, the band gap is of topological non-trivial character while a trivial band gap opens up in the reverse case [20,93]. The strength of λ_{ISB} thereby depends on the bonding distance d of the Sb lattice to the substrate, depicted in figure 5.2 d), and the choice of substrate. As the substrate and atomic number of the adlayer are predefined by the chosen materials, the topological character is solely defined by the bonding length of the Sb monolayer. For indenene, a critical bonding length of $d_{In,crit} = 2.57$ Å is theoretically predicted by DFT above which a topological phase is established [93]. With an experimentally determined bonding length of $d_{In} = 2.68$ Å, this criterion is fulfilled and the electronic structure of indenene thus in a non-trivial regime. Compared to indium, Sb has a slightly increased λ_{SOC} due to the larger atomic number which should reduce the critical value to $d_{Sb,crit} < 2.57$ Å. With a predicted bonding length of $d_{Sb} = 2.64$ Å, according to DFT, the proposed triangular Sb-(1×1) lattice is therefore expected to have a topological non-trivial band gap in the occupied states.

Band structure comparison between theory and experiment

The DFT band structure reproduces all main features observed experimentally, namely four steep metallic bands and a pronounced flat band at higher binding energies. Besides showing similar band dispersions, differences between theoretical and experimental data exist, however, regarding the alignment of bands relative to each other in energy. If the DFT-derived band structure is overlayed to that measured with ARPES, it is not possible to match the position of all bands. If the DFT band structure is aligned to the experimental data such that the binding energy of the flat p_z band at $M_{1\times1}$ matches, see figure 5.4 b), the metallic $p_{x/y}$ bands are shifted rigidly by about -800 meV and the substrate bands by $+400$ meV compared to experiment.
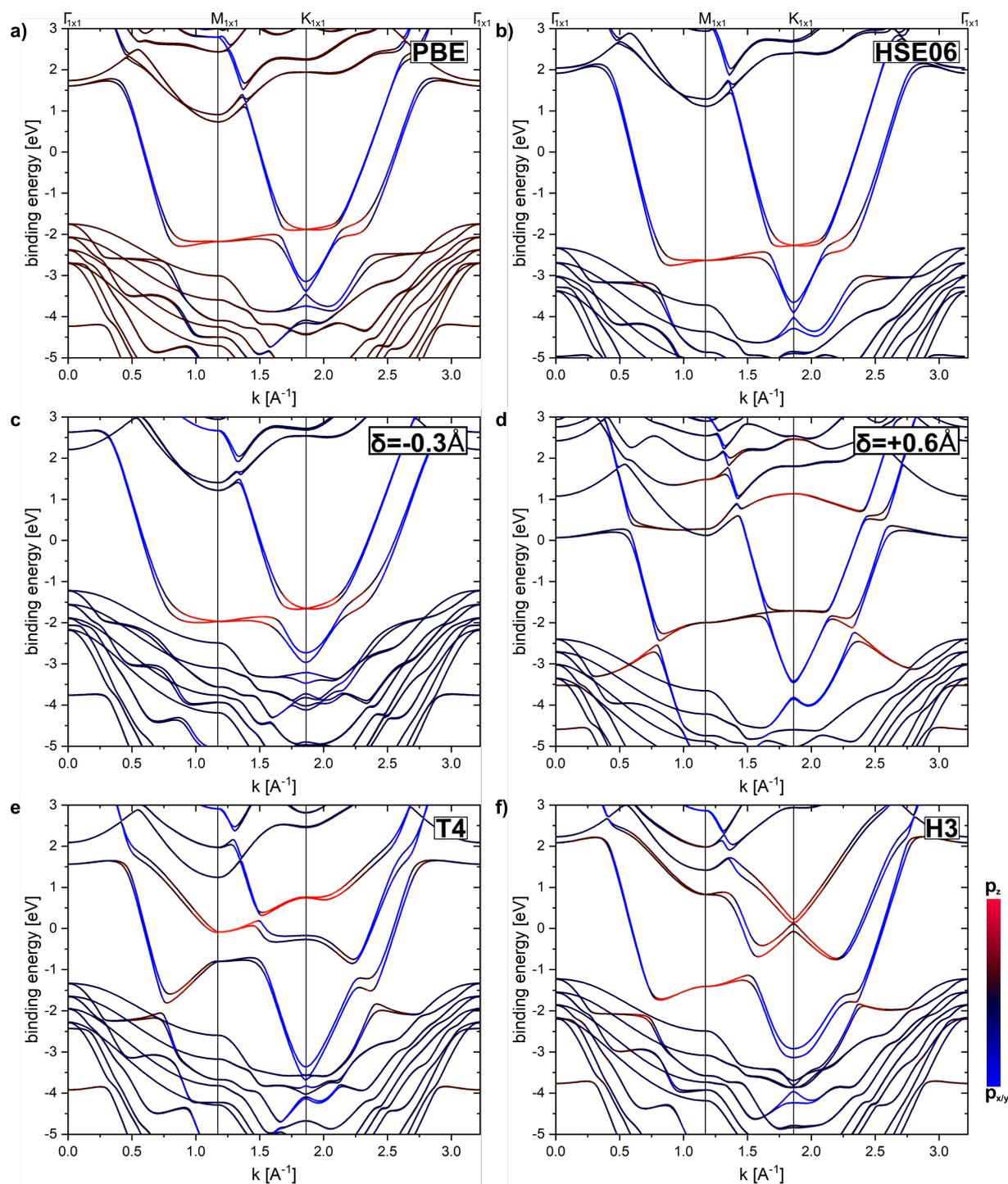
Figure 5.5: *DFT band structure calculations of Sb-(1 × 1) on SiC(0001). a) and b) show the influence of the choice of the functional on the band structure with Sb in T1 position (PBE and HSE06, respectively). c) and d) show the band structure for Sb in adsorption sites T4 and H3, respectively. For e) and f), the bonding length of Sb in T1 sites is reduced and enlarged, respectively.*

In order to investigate potential root causes for this misalignment, the band structure of the Sb-lattice has been calculated with another DFT functional, by assuming other high-symmetry adsorption sites and by varying the Sb bonding length. Figure 5.5 a) shows the same band structure as that in figure 5.4 a) obtained with a PBE functional, but with an increased energy range. For the band structure in figure 5.5 b), an advanced HSE06 functional [113] was used that extends the general gradient approximation by including an Hartree-Fock exchange term. No major differences can be observed beside an overall shift to lower binding energies and a slightly larger band gap at $K_{1\times1}$ of 109 meV. A significant influence of the chosen functional on the resulting band structure can therefore be excluded. For figure 5.5 c) and d), the bonding distances d of the Sb atoms to the substrate were artificially decreased and increased, respectively. Due to a larger influence of the substrate on the electronic properties of the Sb lattice, hybridization gaps are increased for a smaller bonding length. Consequently, hybridization gaps get smaller or even close completely if the Sb lattice is further away from the substrate. The overall alignment of p_z, $p_{x/y}$ and substrate bands relative to each other does, however, not change drastically. The Dirac point moves indeed closer to the flat band with decreasing bonding length, but the separation in energy is still above 1 eV and therefore significantly larger than that observed experimentally of about 0.4 eV. At last, figure 5.5 e) and f) show the corresponding band structures of triangular Sb lattices adsorbed on high symmetry sites T4 and H3, respectively. While similar features are present, namely steep metallic bands and a flat band around $M_{1\times1}$, the band structure close to the Fermi level differs significantly from that observed experimentally. Additionally, total energies of triangular Sb lattices on T4 and H3 sites are increased by 0.95 eV and 0.53 eV compared to T1 sites, respectively. This theoretical finding supports the observation made with STEM that those adsorption sites can be excluded. None of the parameters investigated therefore allow to explain the energetic misalignment between experiment and theory as displayed in figure 5.4 b).

What has so far been neglected in this theoretical analysis of the electronic structure is the inhomogeneous adlayer on top of the Sb-(1×1) lattice that is inevitably present in experiment. Due to its inhomogeneity, and therefore the lack of distinct adsorption sites, its interaction cannot be readily predicted by DFT. Nevertheless, adatoms in specific adsorption geometries are able to alter the band structure as shown for graphene [114]. It might therefore be possible that despite the inhomogeneity apparent in STM and the lack of additional diffraction spots in LEED, a certain adsorption geometry occurs preferably on the Sb monolayer but without long-range order, and alters its electronic properties.

The overall weak and broadened appearance of the Sb-induced bands at least supports the assumption of an influence of the adlayer on the electronic properties of the regular Sb lattice. Despite the observed misalignment of bands, the general agreement between the electronic structure observed in experiment and theory supports the proposed atomic model of a triangular Sb lattice adsorbed in T1 position.

5.1.4 Conclusion on the Sb-(1×1) SiC(0001) surface

All in all, our experimental data supported by theoretical calculations allows to conclude on the preparation of an indenene-like Sb lattice on T1 sites of the SiC(0001) surface which exists below an inhomogeneous Sb adlayer. STEM and LEED measurements thereby indicate the formation of an Sb monolayer lattice on the SiC(0001) surface with Sb atoms centered atop surface Si atoms. This hypothesis is underpinned by ARPES band structure measurements which reproduce all main features expected for a triangular Sb lattice in T1 adsorption sites according to first principle calcuations. The electronic structure thereby resembles that of the topological insulator indenene/SiC with all bands shifted to higher binding energies, including a potential non-trivial band gap in the occupied states.

5.2 Kagome lattice of Sb on SiC(0001)

5.2.1 Preparation and structural characterization of the Sb-(2×2) SiC surface
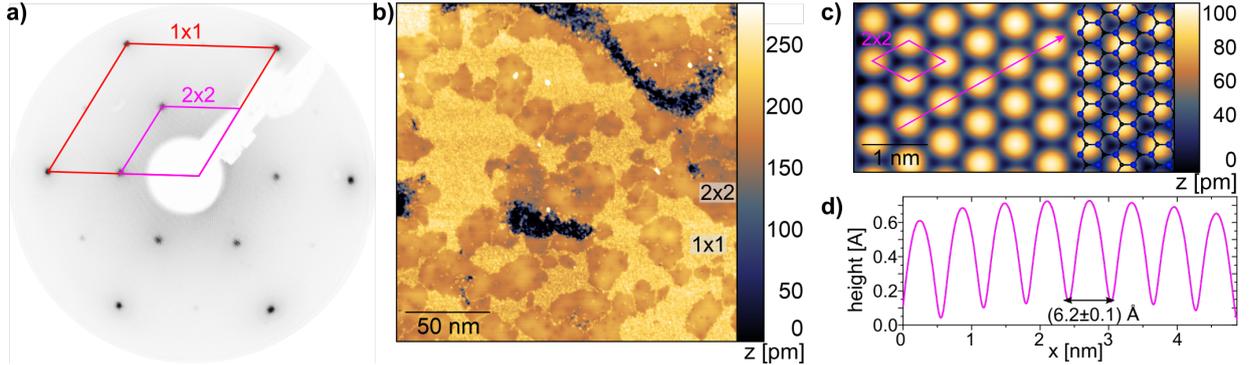
Figure 5.6: a) *LEED (55 eV) image of the Sb-SiC(0001) surface after annealing to 440°C with additional spots indicating the formation of a 2×2 surface structure. b) STM topography image (-3.0 V, 10 pA) of a Sb-SiC(0001) surface after anneal to 440°C. Domains with 2×2 unit cell start to replace the covered Sb-(1×1) surface, but are themselves destroyed simultaneously and leave behind dark 'holes'. c) Close-up STM image (-1.6 V, 60 pA) of the new domains confirm the formation of a well-ordered 2×2 lattice. For size comparison, the atomic model [24] of the substrate is overlayed with arbitrary alignment. d) A unit cell size of 6.2 ± 0.1 is extracted from a line profile marked in c).*

The Sb-SiC(0001) surface can be altered after the initial growth of the covered Sb-(1×1) structure, described in section 5.1.1, by adding a further preparation step. Upon annealing of the as-grown surface to 440°C, parts of the Sb-induced surface undergo a transition to a regular surface lattice with a 2×2 unit cell. The transformation can be seen with LEED which shows additional spots halfway between those of the substrates 1×1 lattice, see figure 5.6 a). STM images of the surface reveal that only parts of the surface host the newly formed antimony lattice, see figure 5.6 b). Within the inhomogeneous Sb adlayer covering the Sb-(1×1), slightly darker domains have formed. These well-ordered domains increase in size if the duration of the anneal is prolonged and supersede patches hosting the covered Sb-(1×1) lattice. However, the substrate temperature required for the transformation seems to be close to the desorption temperature of antimony from SiC. As such, even before the Sb-(1×1) structure is completely substituted, dark 'holes' start to appear on the surface which can be attributed to overheated patches. The annealed Sb-SiC(0001) surface consequently hosts three different types of surface structures. First, patches with

the inhomogeneous adlayer that covers the Sb-(1×1) lattice, second, domains of a well-ordered 2×2 surface lattice and third, overheated patches. The Sb-(2×2) lattice therefore unavoidably coexists alongside covered Sb-(1×1) patches. The maximum surface coverage which could be achieved for the new antimony phase using optimized sample-dependent annealing times was about $\approx 50\%$.

A close-up STM image of a newly formed antimony domain shows a triangular lattice with a 2×2 periodicity of 6.2 ± 0.1 Å, see figure 5.6 c) and d). The shape of the main bright spot changes from triangular to circular if the tunneling voltage is increased from $+1.3$ V $(-1.25$ V$)$ to $+2.0$ V $(-2.0$ V$)$ for the unoccupied and occupied states, respectively, see figure 5.7. Due to the voltage-independent position of the bright spot in topography images, it can be assumed to represent the actual surface topography and therefore most likely indicate the presence of Sb atoms. In between those protrusions, an intensity asymmetry can be observed which discriminates positions A and B of the 2×2 unit cell, labeled in the bottom left of figure 5.7. Measurements closer to the Fermi level than those shown in figure 5.7 have not been possible without crashing the STM tip into the surface. This can be attributed to a large band gap of the Sb-(2×2) and an overall low sensitivity of the experiment to electronic states closer to the Fermi level, as described in detail later on in section 5.2.2.
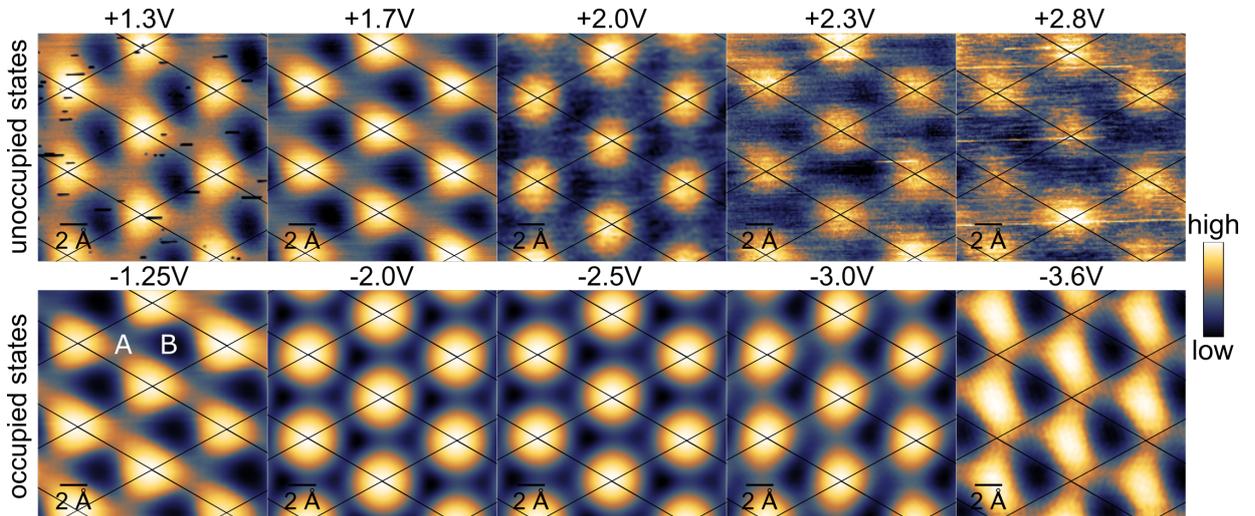
Figure 5.7: *Bias-dependent STM topography images (50 pA) in the occupied and unoccupied states. Black lines outline the 2×2 unit cell. Besides the measurement at -3.6 eV, maximum intensity is found at the same position. Its shape changes from triangular to circular with increasing bias in occupied and unoccupied states. For all biases, an asymmetry between positions labeled A and B is observed.*

Due to the sensitivity of the STM to both, topography and LDOS of the surface, the number of Sb atoms per unit cell and their positions relative to the substrate cannot be unambiguously extracted from these topography measurements. The lateral extensions of the bright spots nevertheless allow to assume a multi-atomic basis. A comparison to the substrate lattice, arbitrary aligned to the Sb-(2×2), see inset in figure 5.6 c), reveals that the size of a bright protrusion encircles about three surface Si atoms. The spots are therefore much larger than the single atomic bright spots of the indenene lattice on SiC(0001) [93]. A direct evidence for a multi-atomic basis, however, can only be provided by atomically resolved atomic force microscopy which is solely sensitive to the surface topography.

5.2.2 Electronic properties of the Sb-(2×2) SiC(0001) surface

Information about the electronic properties of the Sb-(2×2) reconstruction are obtained by investigation with non-local (ARPES) and local (STS) experimental techniques. For comparison with theory, first principle band structure calculations for different atomic models have been provided by the research group of Giorgio Sangiovanni from the Julius-Maximilians-Universität Würzburg with the main work performed by Philipp Eck.

Experimental band structure

For ARPES, the mixed phase sample surface with Sb-(1×1) and Sb(2×2) domain sizes of $10 - 50$ nm is challenging as the beam spot inevitably illuminates both antimony reconstructions simultaneously. In order to attribute features to the Sb-(2×2), it therefore requires the comparison to data measured on a pure Sb-(1×1) sample. Figure 5.8 a) and b) show ARPES measurements along the high-symmetry path of the 2×2 Brillouin zone taken on a Sb-(1×1) and mixed phase sample, respectively. In order to avoid the He I β/γ satellite features of the substrate surrounding $\Gamma_{1 \times 1}$, the path was chosen inside the second Brillouin zone as depicted green in figure 5.8 d). Due to the low surface coverage $< 50\%$, the spectral intensity of features stemming from the Sb-(2×2) is rather low and exacerbates the identification of bands. The comparison of energy distribution curves (EDCs) and momentum distribution curves (MDCs) are therefore used to identify differences between both datasets.
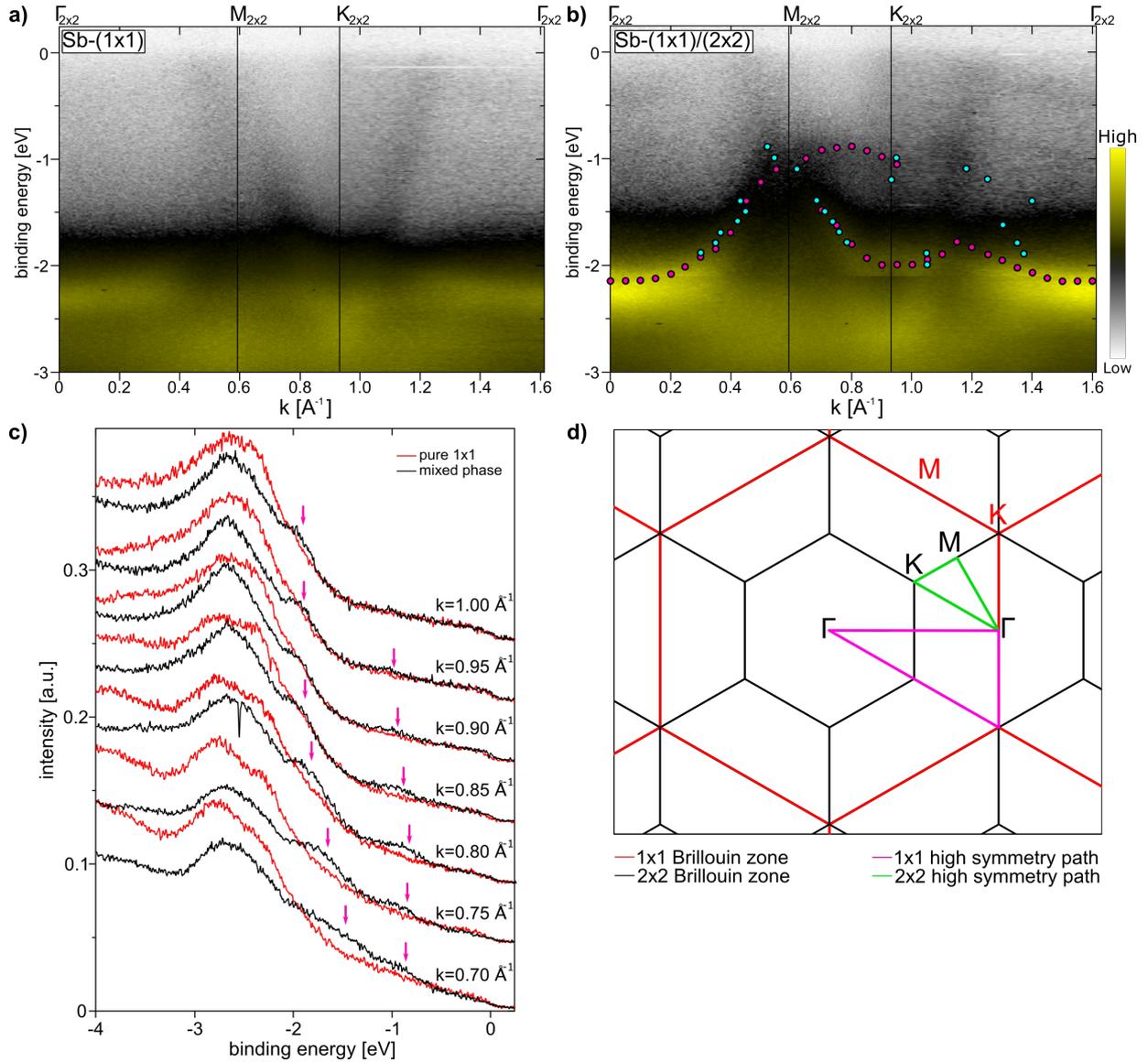
Figure 5.8: a) and b) Experimental band structure obtained with ARPES along the 2×2 high-symmetry path marked in d) on a pure Sb-(1×1) sample at RT and a mixed phase SiC(0001) sample at 10 K, respectively (both datasets are stitched together from separate measurements). Purple and light blue spots mark the position of features that are solely present on the mixed phase sample and can thus be attributed to the formation of a new phase. Positions of purple (light blue) spots have been extracted from a direct comparison of EDCs (MDCs), exemplary shown in c). c) EDCs at different momenta with arrows pointing at features that can be attributed to the Sb-(2×2) lattice. d) Schematic drawing of the high-symmetry paths of the 1×1 and 2×2 Brillouin zone.

Figure 5.8 c) exemplary shows EDCs taken at momenta ranging from -0.7 Å to -1.0 Å for a Sb-(1×1) and mixed-phase sample. Additional weak features can be identified in

the spectra of the mixed-phase sample (marked with arrows) which can be attributed to the presence of the Sb-(2×2) phase. Purple and light blue dots in figure 5.8 b) mark the position of all features identified by a direct comparison of EDCs and MDCs, respectively. Due to the low intensity and shallow appearance of these features, their exact positions in momentum and energy hold errors (EDC: ± 0.15 eV, MDC: 0.05) and should therefore only be taken as guide to the eyes. No features of the new phase can be identified above -0.9 eV which implies a large band gap of up to 900 meV. Around $\Gamma_{2 \times 2}$, a flat band is present at about -2.15 eV, slightly above the coexisting flat band of the Sb-(1×1) band structure at $\Gamma_{2 \times 2}$ (equivalent to $M_{1 \times 1}$). This flat band disperses upwards towards $M_{2 \times 2}$ where a flat feature extends to $K_{2 \times 2}$ while another feature disperses back down to higher binding energies. From $K_{2 \times 2}$ to $\Gamma_{2 \times 2}$, a shallow dispersing band is identified that connects with the flat band at $\Gamma_{2 \times 2}$. The comparison of MDCs additionally implies a band dispersion from $\Gamma_{2 \times 2}$ upwards to $K_{2 \times 2}$ albeit with a very weak fingerprint.

Local density of states
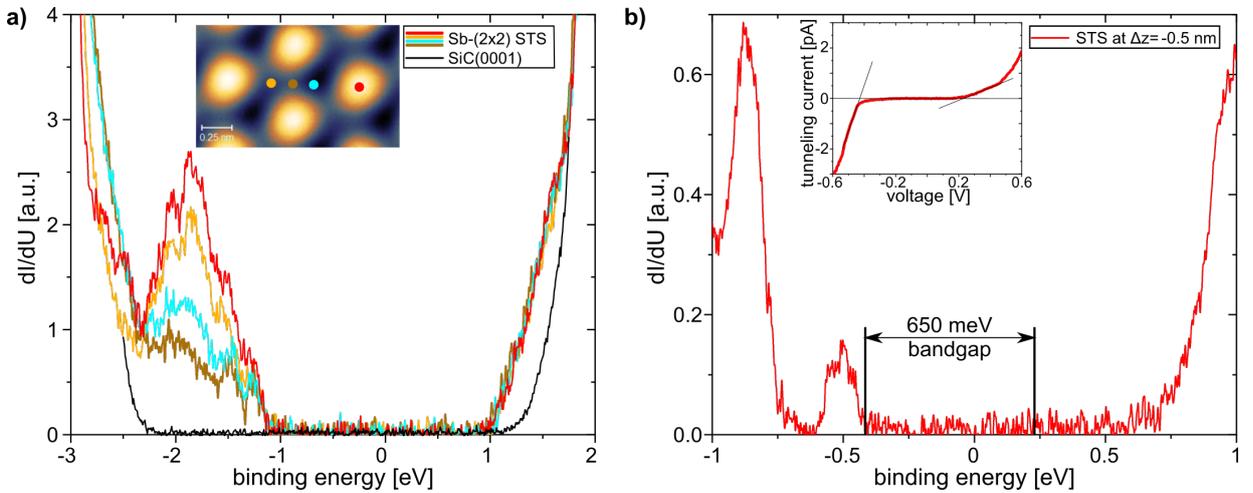
Figure 5.9: a) *STS spectra (setpoint: -2 V/10 pA) taken on different positions inside the 2×2 unit cell (see inset). b) STS spectrum for which the STM tip was manually approached to the surface by Δz after stabilizing at the setpoint used for spectra in a). This method increases the sensitivity to states closer to E_F. The simultaneously measured I(V) curve (inset) allows to extract a band gap of 650 meV.*

In contrast to ARPES, STS allows to locally address the electronic structure of the Sb-(2×2) lattice, albeit momentum integrated. Figure 5.9 a) shows spectra taken with the help of a lock-in amplifier at different positions within the Sb-(2×2) unit cell, representing

the energy-dependent distribution of the local density of states. Before the acquisition of each spectrum, the STM tip was stabilized at a setpoint of -2 V/10 pA. Overall, spectra taken at different positions exhibit identical features only deviating in their respective intensity. As these feature reside inside the SiC(0001) band gap they can be unambiguously attributed to the Sb lattice on the surface. Most prominent is a feature in the range of -1.1 eV to -2.3 eV which is most intense at the position of the unit cell that appears as a bright spot in topography measurements (see inset). The feature itself has a fine structure consisting of several peaks which does not change significantly throughout the unit cell. In the unoccupied states, Sb-related LDOS can be found above $+1.0$ eV, indicating a large band gap of 2.1 eV. This finding is in agreement with the observation that no topography measurements could be conducted in this energy range.

Additional electronic states can, however, be identified, if the tip-sample distance is reduced while taking a spectrum. Therefore, the tip is manually approached to the surface after the before-mentioned stabilization of the tip at the desired STS setpoint. Figure 5.9 b) shows a spectrum taken with the same setpoint as those in figure 5.9 a), but with a tip-sample distance reduced by $\Delta z = 0.5$ nm. Due to the reduced width of the tunneling barrier, the tunneling current is enhanced and additional LDOS features are observed. Two peaks are located in the occupied states at -0.5 eV and -0.88 eV whereas intensity in the unoccupied states is present starting from around $+0.23$ eV and increases strongly above $+0.5$ eV [see I(V) curve in figure 5.9 b)]. The low sensitivity of the STM for these states can have two possible root causes considering peculiarities of the tunneling process. Firstly, the relevant electrons within these states might hold a large parallel momentum. Tunneling into states with finite momentum parallel to the surface enlarges the inverse decay length and consequently reduces their contribution to the tunneling current [115,116]. The tunneling process is therefore dominated by electronic states at Γ and suppresses contributions from states with higher parallel momentum. Secondly, the relevant states might be of $p_{x/y}$ character. As $p_{x/y}$ orbitals lie in-plane of the surface, they naturally have a larger separation from the STM tip compared to p_z orbitals sticking out of the surface. This increases the tunneling barrier and consequently reduces their contribution to the tunneling current. The electronic states detected close to the Fermi level therefore presumably hold a high parallel momentum, are of $p_{x/y}$ character or feature a combination of both.

The I(V) curve corresponding the spectrum in figure 5.9 b), see inset, allows to determine the Sb-(2×2) band gap to (650 ± 50) meV ranging from -0.42 eV to $+0.23$ eV. The

observation of a large band gap within the occupied states is in agreement with the ARPES results shown in figure 5.8 b). As the electronic states of flat bands are compressed in a narrow energy range, they typically appear as intense peaks in LDOS spectra. The sharp LDOS feature at -0.88 eV and the most prominent peak around -1.9 eV could therefore be related to flat features observed in ARPES at -0.9 eV and -2.15 eV, respectively. All in all, the general agreement between ARPES and STS allows to assign the new features in ARPES to the Sb-(2×2) lattice observed with STM.
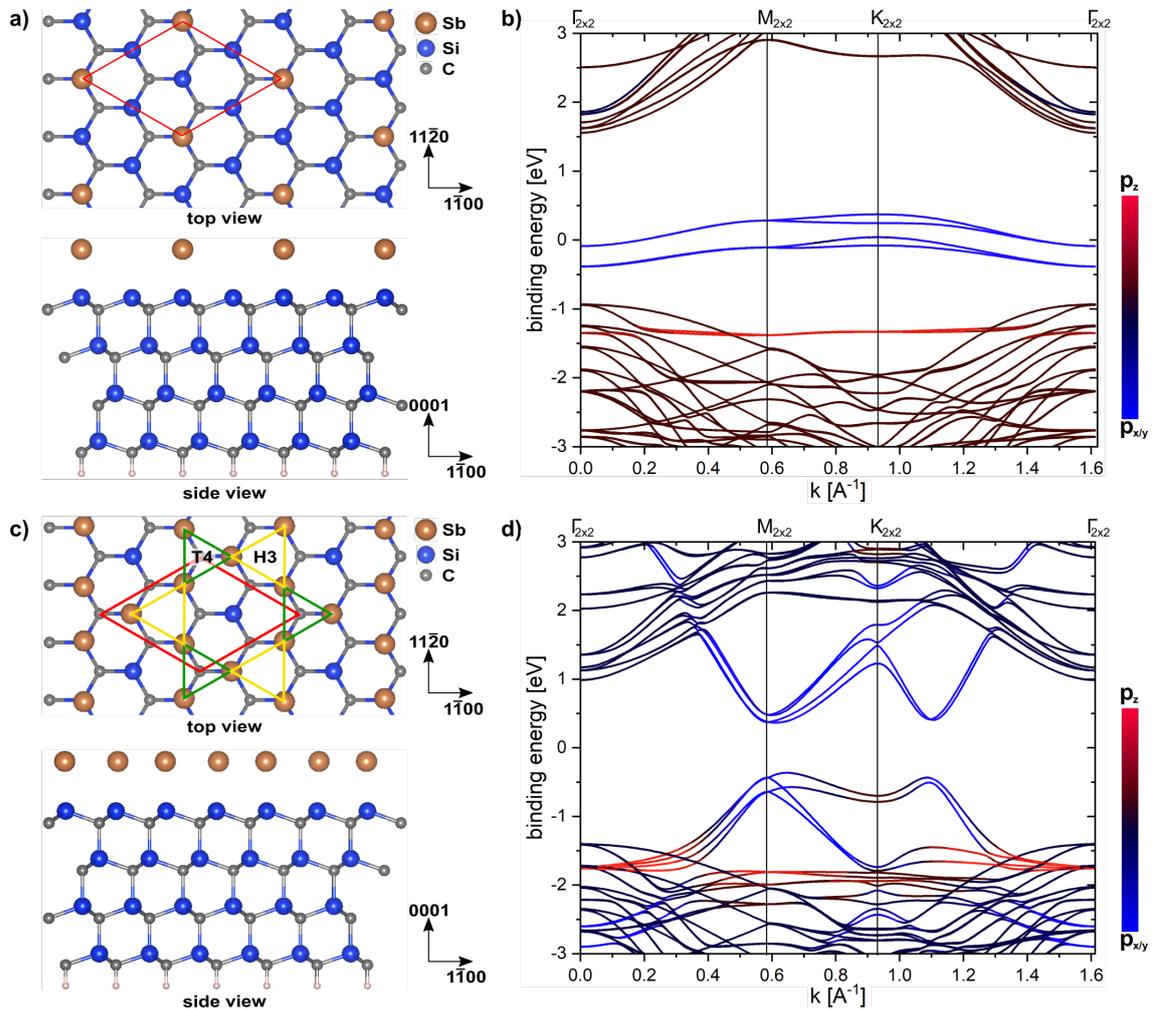
Figure 5.10: a) Atomic model [24] of a Sb-(2×2) lattice with 0.25 ML coverage. For clarity, the top view is limited to the substrate atoms of the surface layer. b) The corresponding DFT band structure, including SOC, shows three flat bands, two bands with $p_{x/y}$ orbital character around E_F and a p_z band at -1.3 eV. c) Atomic model [24] of a kagome-like Sb-(2×2) lattice with a slight asymmetry regarding the size of the triangles. For clarity, the top view is again limited to the substrate atoms of the surface layer. d) The corresponding DFT band structure, including SOC, shows a band gap of 610 meV.

5.2.3 Band structure calculations for atomic model candidates

With the knowledge obtained experimentally on the electronic properties of the Sb-(2×2) lattice, two Sb lattices with 2×2 periodicity are investigated with DFT[2]. We assume two simple atomic models which are closely related to the Sb-(1×1), see figure 5.10 a) and c). Both models allow for a simple transition from the 1×1 to 2×2 phase as they are both diluted 1×1 lattices with Sb atoms on T1 adsorption sites but reduced Sb coverage. As such, no significant mass transport and/or structural rearrangement is required during phase transition. The atomic model shown in figure 5.10 a) depicts the simplest case for a lattice with 2×2 periodicity, a single atomic basis. For the second atomic model in figure 5.10 c), a three-atomic basis is chosen based on the observation of triangular features in STM at certain energies, see section 5.2.1.

Figure 5.10 a) displays the atomic model of a triangular Sb lattice following a 2×2 periodicity with a surface coverage of 0.25 ML. The interatomic distance of Sb atoms is 1.24 nm, twice the distance of the Sb-(1×1) lattice, which significantly reduces the Sb-Sb interaction. The high localization of the Sb orbitals is reflected in the corresponding DFT calculated band structure in figure 5.10 b). All Sb bands disperse flat across the entire Brillouin zone without exhibiting a significant SOC splitting. A p_z band is located at -1.4 eV while two bands of $p_{x/y}$ character disperse around the Fermi level and render the system metallic. This band structure looks alike that predicted initially for a Sn-$(\sqrt{3} \times \sqrt{3})R30°$ lattice on SiC(0001) [117], albeit with double the number of flat bands around E_F. As the Sn-$(\sqrt{3} \times \sqrt{3})R30°$ lattice did not show a flat band around the Fermi level in PES experiments, but a large band gap, it was initially interpreted as a Mott-Hubbard insulator [117] but later explained with the formation of an anti-ferromagnetic order in the Sn lattice [118]. Compared to the experimental ARPES data obtained on the Sb-(2×2) lattice, the proposed band structure in figure 5.10 a) does not show many similarities besides the flat p_z band which is present at Γ. Especially, no bands disperse from the flat band towards the Fermi level around $M_{2 \times 2}$ as observed experimentally. This model candidate can therefore be discarded as an explanation for the experimental data.

The atomic model shown in figure 5.10 c) depicts an Sb lattice in 2×2 periodicity with a surface coverage of 0.75 ML. The three Sb atoms per unit cell form a kagome lattice that consists of interconnected equilateral triangles with enclosed hexagonal spaces, depicted

---

[2]theory support provided by the research group of Giorgio Sangiovanni from Julius-Maximilians-Universität Würzburg

with green and yellow triangles. Due to the lower symmetry of the SiC substrate, the C_{6v} symmetry of the prototypical kagome lattice is reduced to C_{3v} as Sb atoms surrounding surface carbon atoms are pulled closer to each other. This reduces the size of triangles around T4 sites (green) to 2.90Å per side while enlarging triangles around H3 sites (yellow) to 3.25Å per side. The DFT calculated band structure of this asymmetrical kagome surface lattice is shown in 5.10 d). The system is in an insulating state with an overall band gap of 610 meV centered around the Fermi level. The conduction and valence band consist of two SOC split bands of mainly $p_{x/y}$ character and are almost particle hole symmetric. Both bands disperse towards the Fermi level from $\Gamma_{2\times2}$ to $M_{2\times2}$. While one band drops back down to higher binding energies towards $K_{2\times2}$, the other band has a camel-hump appearance with a flat segment towards $K_{2\times2}$ and another extremum on its way to $\Gamma_{2\times2}$. Similar to the other Sb-SiC(0001) band structures shown in this chapter, the band structure exhibits a flat p_z band in the occupied states due to the Sb atoms bonding to the substrate [51]. At crossings with the Sb in-plane orbitals the inversion symmetry breaking of the substrate allows for hybridization gaps. The prototypical electronic structure of a kagome lattice featuring a flat band and a Dirac crossing at K are, however, impossible to identify for this atomic model. This is attributed to the overall complex band structure featuring the SOC splitting of the bands, the opening of hybridization gaps and the interaction of Sb bands with the bulk band structure.

5.2.4 Comparison of experiment and theory

Figure 5.11 a) provides a direct comparison of the Sb-(2×2) band structure obtained with ARPES and the DFT calculated band structure of the asymmetric kagome lattice. For this overlay, theoretical data was shifted by -400 meV which allows for a good agreement. The shift towards higher binding energies can be explained twofold. Firstly, the chemical potential of our SiC(0001) sample is shifted due to its n-type doping. Secondly, the illumination of the sample during the ARPES measurement causes a surface photo voltage effect on semiconductor surfaces. For semiconductors with an intrinsic upward band bending towards the surface, as present for n-doped SiC(0001) [119], the surface photo voltage typically reduces the band bending causing a rigid shift of the spectrum in the order of several tenths eV towards higher binding energies [120].
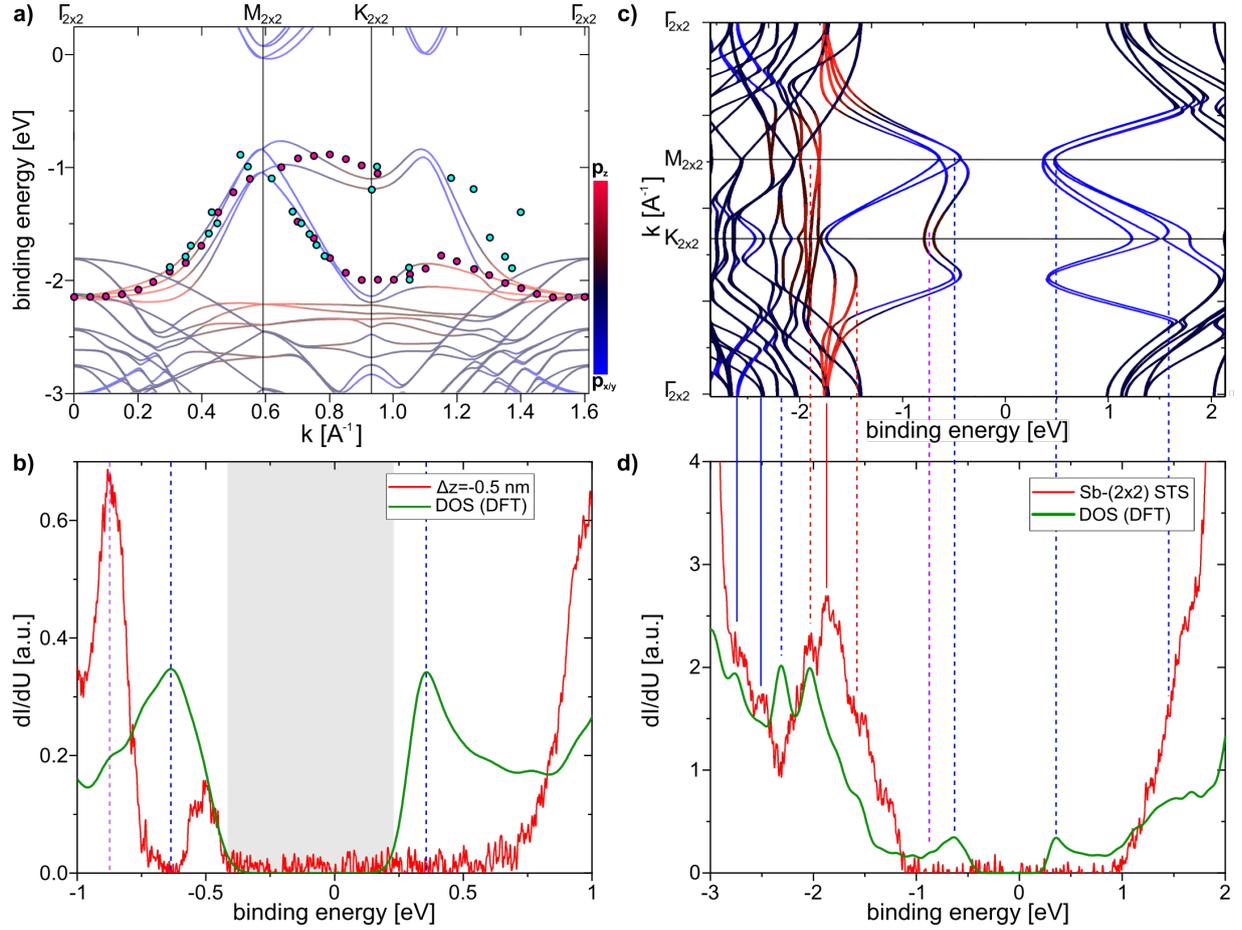
Figure 5.11: a) *Overlay of spectroscopic features found in ARPES with the DFT band structure calculation of the asymmetric Sb kagome lattice. Theoretical data is shifted by -400 meV to achieve a good agreement. b) Spectroscopic data of the LDOS overlayed with the density of states obtained from DFT. The theoretical data was aligned in energy by -140 meV to match the position of the experimental band gap (shaded area). c) DFT band structure of the asymmetric Sb kagome lattice rotated by $90°$ to allow for an easy comparison with the overlay of experimental and theoretical LDOS data in d). Lines between both figures and within b) are guide to the eyes to correlate peaks in the LDOS data with band structure features. Solid (dashed) lines indicate features located at $\Gamma_{2\times2}$ (around $M_{2\times2}$ or $K_{2\times2}$) while their color represents the orbital character of the feature.*

Including this shift in the DFT data, experimental features closely trace band dispersions predicted theoretically for the asymmetric kagome lattice. The symmetric hump around $M_{2\times2}$ that connects to the flat band at -2.15 eV is well reproduced whereas the position of the faint flat feature at about -1 eV of figure 5.8 b) can be explained with the camel-hump feature of the DFT valence band. The good agreement of experiment and theory regarding the electronic band structure therefore strongly suggests the formation of an asymmetric kagome lattice of antimony on SiC(0001).

Figure 5.11 b) and d) show an overlay of the STS data shown in figure 5.9 with the momentum-integrated density of states of the asymmetric kagome lattice as obtained from DFT. The theoretical data is thereby shifted rigidly by -140 meV to match the position of the experimental and theoretical band gap which are of similar size ((650 ± 50) meV and 610 meV, respectively). Including this shift, peak positions expected from theory are mostly reproduced by the experimental spectrum [see lines connecting figure 5.9 c) and d), as well as lines in b)], except features at $+350$ meV, -650 meV and -2.3 eV. This discrepancy can, however, be explained by taking into account the orbital character of the corresponding electronic states and their finite parallel momentum k_{II} in reciprocal space, see discussed in 5.2.2. Firstly, $p_{x/y}$ orbitals do not protrude out of the surface like p_z orbitals. They are therefore located further away from the STM tip which mitigates their contribution to the tunneling current. Secondly, a large parallel momentum k_{II} of electrons enlarges the inverse decay length χ [115,116] of the tunneling process, see chapter 2.1, and reduces the contribution of such states to the measured signal. Consequently, p_z states around Γ are expected to appear as intense peaks in STS whereas $p_{x/y}$ states at finite parallel momenta contribute significantly less to the tunneling current. Taking into account this selective sensitivity of the STS measurement allows to explain the before-mentioned discrepancies between theoretical LDOS and the STS spectra. For a better visualization, lines connecting features in figure 5.9 c) and d) and those in figure 5.9 b) have been colorized and altered according to their orbital character and parallel momentum value from DFT. Solid (dashed) lines indicate features located at $\Gamma_{2\times2}$ (high parallel momenta) while the color represents the orbital character of the feature. As expected, the flat p_z band at Γ (solid red line) coincides with the strongest peak in STS while features at $M_{2\times2}$ and $K_{2\times2}$ of $p_{x/y}$ character (dashed blue lines) are hardly visible in experiment. As the calculated DOS integrates over states of the entire Brillouin zone without taking into account the local nature of the STS measurement, a comparison to experiment is only meaningful regarding peak positions and not their intensity. The good agreement observed in figure 5.11 d) thereby supports the existence of an asymmetric kagome lattice on the SiC(0001) surface.

While both experimental datasets, ARPES and STS, can be explained with the formation of an asymmetric kagome lattice of Sb on the SiC(0001) surface, the alignment in energy between both methods differs by about 260 meV. This difference can be attributed to a combination of surface photo voltage effect in ARPES, and local variations in the doping level affecting STS measurements.
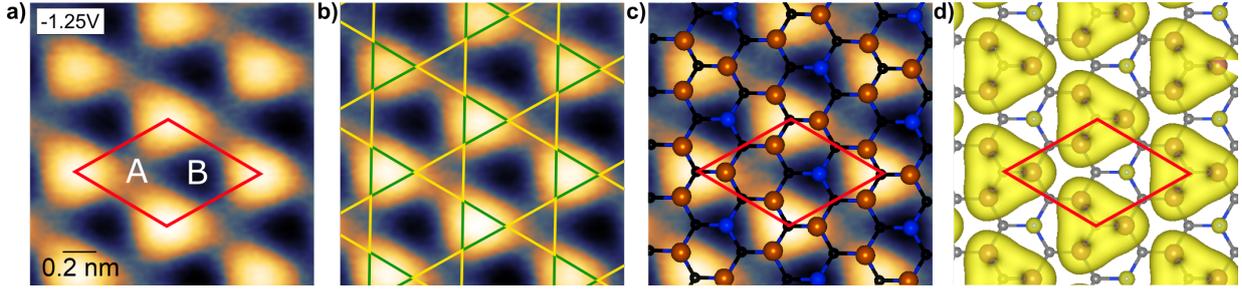
Figure 5.12: *a)-c) STM topography images of the Sb-(2×2) (−1.25 V, 50 pA) overlayed with the outline of the 2×2 unit cell, a schematic of the asymmetric kagome lattice structure and the atomic model [24], respectively. d) Real space charge density distribution of valence band states at $M_{2×2}$ and $K_{2×2}$.*

Figure 5.12 shows STM topography images of the Sb-(2 × 2) overlayed with a schematic outline and the atomic model of the asymmetric kagome lattice. As there are two distinguishable triangles forming the asymmetric kagome lattice, the lattice can in principle be aligned twofold to the STM image in figure 5.12 b). Intuitively, an increased LDOS can be expected at the position of the smaller triangle due to a higher local density of Sb atoms. This assumption is supported by a calculation depicting the real space charge density distribution obtained for the valence band states at $M_{2×2}$ and $K_{2×2}$[3]. It reproduces the triangular shape surrounding the smaller antimony triangle. Assuming this alignment, the represenation of the charge density distribution is additionally able to reproduce the experimentally observed asymmetry of positions A and B. The spot of least intensity (B) marks the position of the unoccupied surface Si atom while the larger Sb triangle possesses an intermediate intensity (A). This is again to be expected, as the surface Si atom is located below the Sb layer and does not host valence band states. While STM data on their own does not allow to conclude on the underlying atomic lattice, the atomic model allows to explain the experimental STM image considering reasonable assumptions and therefore supports the formation of the proposed asymmetric kagome lattice.

5.2.5 Conclusion on the kagome lattice of Sb on SiC(0001)

By annealing a Sb-SiC(0001) surface to 440°C, a Sb-(2 × 2) lattices forms which can be attributed to the formation of an asymmetric Sb kagome lattice with a surface coverage of 0.75 ML. It exists solely within a small temperature range and inevitably co-exits with the Sb-(1 × 1) phase. From experiment (ARPES, STS) the lattice is found to exhibit a large

---

[3]provided by Philipp Eck, Julius-Maximilians-Universität würzburg

band gap around the Fermi level of about 650 meV. Its band structure features a flat band centered around $\Gamma_{2\times2}$ and valence band maxima near $M_{2\times2}$ and $K_{2\times2}$. The experimental data can be readily explained with the formation of a kagome lattice consisting of triangles with slightly asymmetric sizes, attributed to the reduced symmetry of the substrate.

So far, 2D kagome lattices have only been realized in multi-component materials such as layered van der Waals materials (e.g., RbV_3Sb_5 or $Pd_3P_2S_8$), ternary ferromagnetic $Co_3Sn_2S_2$ [121] or SiO_2 [122]. A surface kagome lattice involving only a single atomic species has, to the best of our knowledge, thus far only been realized in twisted bilayer silicene [123]. The kagome structure is thereby, however, only induced by a moiré pattern in the electronic structure with a large unit cell size of about 17 Å and not in the atomic structure itself. The realization of an elemental purely 2D atomic surface kagome lattice therefore represents the first of its kind. Despite the simple atomic structure of a kagome lattice, the corresponding electronic structure deviates from the simple prototypical kagome band structure. This is attributed to the presence of the SiC(0001) honeycomb substrate that breaks inversion symmetry parallel to the surface normal, reduces the in-plane symmetry to $C_{3\nu}$ and forms covalent bonds between Sb and surface Si atoms on T1 sites. The strong interaction creates hybridization gaps between in- and out-of-plane states which strongly alters the electronic structure. Additionally taking into account SOC splitting due to the heavy Sb atoms and the presence of substrate bands, it is therefore difficult to retrieve the typical kagome features from the band structure of the Sb-(2×2) lattice.

5.3 Conclusion

In summary, two novel Sb-induced atomic lattices on SiC(0001) have been identified by a combined study of STM, ARPES, STEM and DFT, namely a triangular Sb-(1×1) covered by an inhomogeneous Sb adlayer and an asymmetric kagome lattice of Sb with a 2×2 periodicity. The atomic structure of the Sb-(1×1) is identical to that of indenene on SiC(0001), an experimentally confirmed topological insulator, with one Sb atom atop each surface Si. The band structure comprises four metallic bands, a flat band at $M_{1\times1}$ and a Dirac cone at $K_{1\times1}$. According to DFT, the latter is supposed to gap up due to an interplay of SOC and the symmetry breaking of the substrate. A comparison to indenene suggests, that the non-trivial character of the Dirac cone persists for this Sb-(1×1) lattice. The asymmetric kagome lattice emerges from the Sb-(1×1) upon annealing and basically

represents a diluted form of the Sb-(1 × 1) lattice with a reduced Sb surface coverage of 0.75 ML. Its electronic structure deviates from the simple structure of a prototypical kagome lattice due to the presence of the SiC(0001) substrate. It features a large band gap of 650 eV around the Fermi level. For both lattices, Sb-(1×1) and Sb-(2×2), a flat p_z band is spanning the Brillouin zone in the occupied states at about -2 eV. The similarity arises due to the same Sb-Si bond at the interface which pulls the contributing p_z orbitals away from the low energy region towards higher binding energies. The low energy properties are therefore for both lattices dominated by states of $p_{x/y}$ character, similar to the case of indenene [93] and bismuthene [51].

Both novel Sb-based lattices offer the opportunity to explore exotic quantum states of matter, albeit hard-to-reach. The triangular Sb-(1 × 1) is possibly hosts topological non-trivial physics at its Dirac point, similar to indenene, with a band gap large enough to persist at room temperature. Major drawbacks, however, are the position of the Dirac cone deep in the occupied states at -3.4 eV, the concurrent presence of substrate bands at the same binding energy and the unavoidable presence of the inhomogeneous adlayer. They prevent the application of transport measurements and the unperturbed investigation of its electronic properties with STM. The asymmetric kagome lattice, in principal, allows to investigate the most trivial case of a kagome lattice with single atoms of the same element on each lattice site. This simple case is, however, disturbed by the presence of the SiC(0001) substrate that allows for hybridization gaps to open. The presence of the SiC(0001) bulk bands additionally obstructs the experimental observation of kagome features such as the Dirac cone or flat band.

6 Oxidation of 2D elemental surface lattices on SiC(0001)

So far, this work focused on the growth and investigation of novel Sb-induced surface structures and their electronic properties in the protected environment provided by UHV. Those clean conditions enable the reproducible growth of well-ordered surface lattices with a minimal amount of defects and are inevitable for the application of surface sensitive techniques such as STM, ARPES, XPS, LEED or XSW. On the contrary, future applications require materials which are stable and resilient under ambient conditions regarding their atomic structure and electronic properties. This requirement is especially challenging for (sub-)monolayer surface materials as their entire atomic structure is naturally exposed to the surrounding environment and occurring chemical reactions unavoidably alter their 2D bulk properties. As a first step towards real-world application of 2D materials, it is therefore of utter importance to investigate their response to external influences.

In ambient atmosphere, oxygen is infamous for its erosive reactions with metals due to its strong electronegativity and concomitant high reactivity. The most common observation of oxidation in everydays life is rust which can corrode even bulky chunks of iron. The predisposition to oxidation and the implied effects on the material are, however, different for each metal. At low temperatures, metal oxidation has been studied in detail experimentally and theoretically since the 1930s [124–127]. At room temperature, the initial chemical adsorption (chemisorption) of oxygen on a clean metal surface doesn't need to overcome an activation energy and thus happens fast [126]. The duration of this oxide growth phase depends on the metal species and can persist up to an oxide layer thickness of 0.5 ML (e.g., for Sb) to 10 ML (e.g.,for Fe) [126]. Later on, oxide growth will be limited by the diffusion rate of oxygen or metal ions through the resulting oxide layer. In contrast to bulk materials, the entire oxidation of 2D materials is naturally limited to this initial oxidation phase as the entire atomic lattice is exposed. It is, however, not possible to deduce the

behavior of monolayer lattices from the initial oxidation of their bulk equivalents due to a different bonding situation of substrate supported 2D materials. Each monolayer material therefore requires to be investigated separately regarding its sensitivity to oxygen.

So far, oxidation studies of 2D materials are scarce and mainly focus on exfoliated mono-layers of graphene, hexagonal boron nitride hBN, black phosphorus or TMDCs [128–132]. Their behavior under exposure to oxygen or ambient conditions varies strongly. Black phosphorus is easily oxidized by oxygen or water [128, 129] while a monolayer of the TMDC MoS_2 oxidizes rather slowly over the time of several months [130]. Graphene and hBN, in stark contrast, have been reported to be robust against low-temperature oxidation and the influence of ambient atmosphere in general [131, 132]. The only study on the oxidation behavior of an epitaxially grown (sub-) monolayer material has, to the best of our knowledge, so far been performed by Kuhn et al. [34]. They investigated the oxidation behavior of the 2D TI bismuthene, a hexagonal lattice of bismuth atoms on SiC(0001) [13]. The bismuth lattice was found to oxidize quickly if exposed to even small amounts of oxygen.

In this chapter, we systematically study the stability of (sub-)monolayer lattices of in-denene, bismuthene and antimony on 4H-SiC(0001) under a controlled oxygen exposure by means of XPS. In all cases, oxidation takes place and eventually affects the entire surface lattice. The observed onset dosages and oxidation rates of each atomic species reveal that the antimony-induced surface is significantly less sensitive to oxidation compared to bismuthene or indenene. Attempts to thermally recover the pristine surface lattices result in a loss of adsorbate atoms and the irrevocable destruction of the monolayer lattice. At last, different protective measures against oxidation are discussed.

6.1 Initial surface characterization

For this study, (sub-)monolayer surface reconstructions of different atomic species on 4H-SiC(0001) were investigated, namely indenene/SiC, bismuthene/SiC and Sb-SiC. The choice of these materials is justified by their high relevance in current research due to their intriguing electronic properties as topological non-trivial 2D materials (indenene, bismuthene), their availability (in-house production) and their common adsorption site T1 on the very same substrate SiC(0001) which allows for a direct comparison. In-denene/SiC(0001) and bismuthene/SiC(0001) samples for this study were provided by colleagues from the chair of experimental physics 4 (EP4) at Julius-Maximilians-Universität
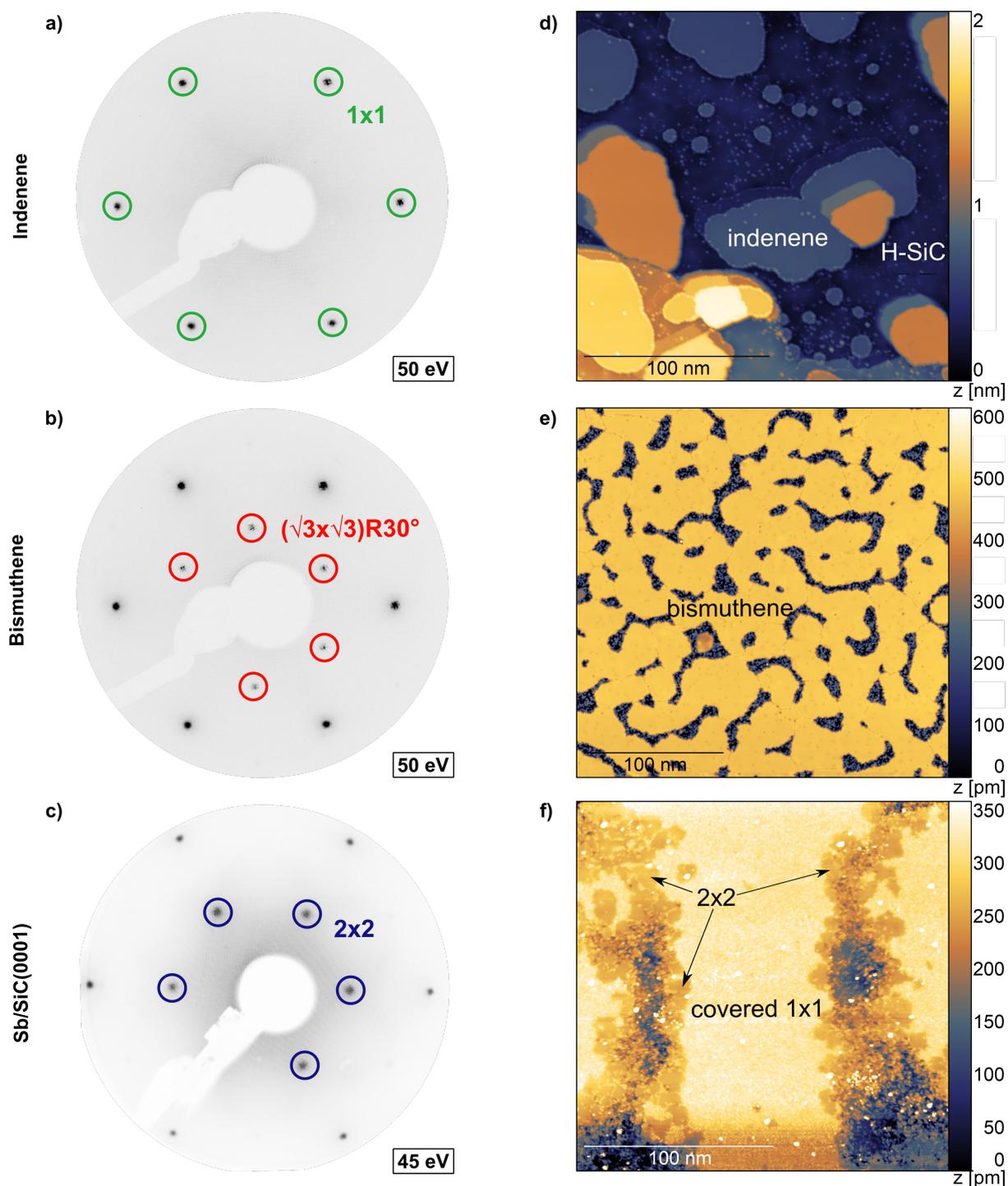
Figure 6.1: *Characterization of the pristine as-grown adsorbate surfaces of indenene, bismuthene and Sb-SiC with LEED a) - c) and STM d) - f). For these samples, indenene domains were observed as isolated 1×1 islands (including a negligible amount of a higher coverage phase), bismuthene as an almost closed film and the Sb-SiC surface had its mixed-phase surface consisting of the exposed Sb-(2×2) and buried Sb-(1×1).*

which are specialized in their preparation, namely Jonas Erhardt [112] and Raul Stühler [33], respectively. The Sb-SiC(0001) sample was grown according to the recipe of 5.1.1 and 5.2.1 which results in a mixed-phase surface featureing both, the covered Sb-(1×1) reconstruction and the asymmetric kagome lattice.

Before oxidation, each sample was characterized regarding its prevailing surface reconstruction (LEED) and the relative coverage of each surface reconstruction (STM). Figure 6.1 displays the results of the initial characterization of each sample. After growth, LEED verifies that besides the desired (sub-)monolayer lattice periodicities (indenene: 1×1, bismuthene: $(\sqrt{3} \times \sqrt{3})$R30°, Sb-SiC: 2×2) no other ordered phases are present, see figure 6.1 a)-c). As LEED measurements are solely sensitive to long-range ordered structures and do not provide precise information about the relative surface coverage of the desired lattices or the existence of disordered domains, the surfaces were additionally investigated with STM, see figure 6.1 d)-f). The surface coverages are found to be 41%, 81% and $(73 + 10)$% for indenene, bismuthene and ordered Sb domains $(1 \times 1 + 2 \times 2)$, respectively. Those values are prone to errors and should only be taken as rough estimates due to local variations in coverage and the comparably small surface area probed by STM relative to the beam spot diameter (≈ 1 mm) of the XPS setup, used later. Even though indenene domains have the smallest surface coverage of ≈ 41%, STM does not show regions of disordered In atoms around the isolated indenene islands, but the flat H-terminated SiC surface [93]. This allows to unambiguously attribute changes of the In core level spectrum in XPS during the oxidation study to atoms of the indenene lattice.

For bismuthene, areas in between bismuthene domains do not show the bare SiC surface but disordered structures. Their topographic height is lower than that of bismuthene which indicates no or only very dilute amounts of bismuth atoms. Their contribution to the core level signal in XPS of bismuth is therefore assumed to be negligible. In the case of Sb-SiC(0001), it is not possible to assign the core level evolution during oxidation to a single surface reconstruction. The surface shows bare domains of the Sb-(2×2) kagome lattice, areas of the Sb-(1×1) reconstruction covered by an inhomogeneous adlayer and overheated hole-like patches [similar to those in-between bismuthene domains in figure 6.1 e)]. The oxidation behavior observed with XPS can therefore only be taken as a general property of an adsorbate layer of antimony on SiC(0001) and not as the property of a single Sb-induced surface reconstruction.
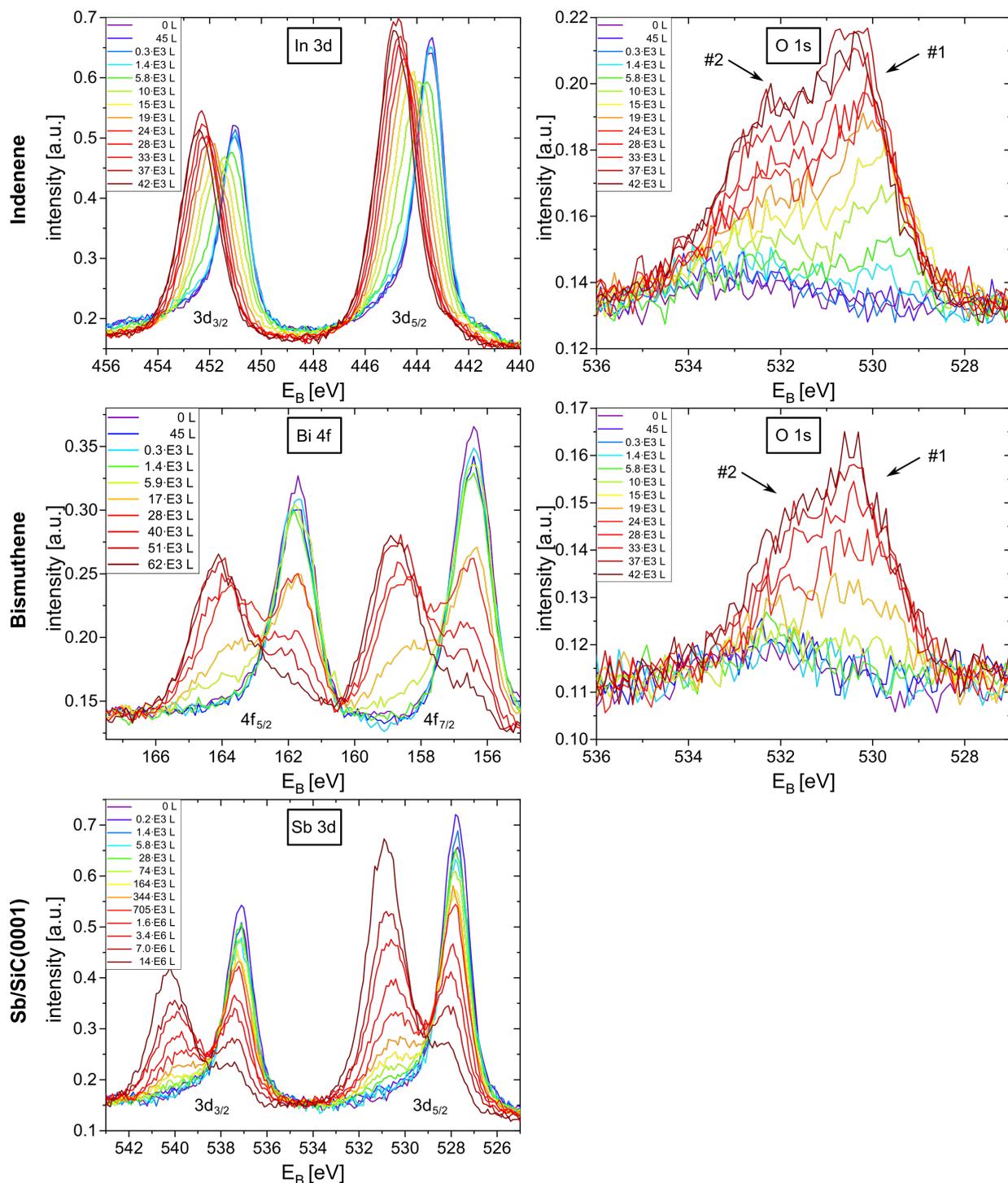
| step | Indenene | | Bismuthene | | Sb-SiC(0001) | |
#	pressure [mbar]	dosage [L]	pressure [mbar]	dosage [L]	pressure [mbar]	dosage [L]
1	$1.0 \cdot 10^{-7}$	45	$1.0 \cdot 10^{-7}$	45	$5.0 \cdot 10^{-7}$	226
2	$5.0 \cdot 10^{-7}$	226	$5.0 \cdot 10^{-7}$	226	$2.5 \cdot 10^{-6}$	$1.1 \cdot 10^3$
3	$2.5 \cdot 10^{-6}$	$1.1 \cdot 10^3$	$2.5 \cdot 10^{-6}$	$1.1 \cdot 10^3$	$1.0 \cdot 10^{-5}$	$4.5 \cdot 10^3$
4	$1.0 \cdot 10^{-5}$	$4.5 \cdot 10^3$	$1.0 \cdot 10^{-5}$	$4.5 \cdot 10^3$	$5.0 \cdot 10^{-5}$	$2.3 \cdot 10^4$
5	$1.0 \cdot 10^{-5}$	$4.5 \cdot 10^3$	$2.5 \cdot 10^{-5}$	$1.1 \cdot 10^4$	$1.0 \cdot 10^{-4}$	$4.5 \cdot 10^4$
6	$1.0 \cdot 10^{-5}$	$4.5 \cdot 10^3$	$2.5 \cdot 10^{-5}$	$1.1 \cdot 10^4$	$2.0 \cdot 10^{-4}$	$9.0 \cdot 10^4$
7	$1.0 \cdot 10^{-5}$	$4.5 \cdot 10^3$	$2.5 \cdot 10^{-5}$	$1.1 \cdot 10^4$	$4.0 \cdot 10^{-4}$	$1.8 \cdot 10^5$
8	$1.0 \cdot 10^{-5}$	$4.5 \cdot 10^3$	$2.5 \cdot 10^{-5}$	$1.1 \cdot 10^4$	$8.0 \cdot 10^{-4}$	$3.6 \cdot 10^5$
9	$1.0 \cdot 10^{-5}$	$4.5 \cdot 10^3$	$2.5 \cdot 10^{-5}$	$1.1 \cdot 10^4$	$2.0 \cdot 10^{-3}$	$9.0 \cdot 10^5$
10	$1.0 \cdot 10^{-5}$	$4.5 \cdot 10^3$			$4.0 \cdot 10^{-3}$	$1.8 \cdot 10^6$
11	$1.0 \cdot 10^{-5}$	$4.5 \cdot 10^3$			$8.0 \cdot 10^{-3}$	$3.6 \cdot 10^6$
12	$1.0 \cdot 10^{-5}$	$4.5 \cdot 10^3$			$8.0 \cdot 10^{-3} (20 \, \text{min})$	$7.2 \cdot 10^6$

Table 6.1: *List of oxygen pressures and oxygen dosages to which each sample was exposed for* 10 *min each (if not stated otherwise).*

6.2 Controlled exposure to oxgen

Samples were exposed to oxygen in a small UHV chamber connected to the XPS setup via an *in-situ* transfer system. Oxygen of purity 99.9995% was dosed into the chamber via a leak valve. As a turbo pump was continuously running, the oxidation experiment took place in a constant oxygen flow instead of a static oxygen atmosphere. The sample surface normal was aligned perpendicular to the incoming oxygen stream to avoid a direct bombardment. During exposure, the chamber pressure was monitored with a cold cathode ion gauge located about 10 cm above the sample. The leak valve was adjusted manually to guarantee a constant oxygen pressure with deviations below the second valid digit of the target pressure. The duration of each exposure was chosen to be 10 min, with a single exception for the last oxidation step of Sb of 20 min.

Oxygen pressure and dosage (1 L = 10^{-6} Torr·s) of each oxidation step are listed in table 6.1. With all steps performed on the very same sample for each material, the overall dosage to which a sample was exposed at any time is given by the sum over the dosages of all previous oxidation steps. The dosage of each step was adjusted according to the impact of the preceding step until the adsorbate core level spectra indicated complete oxidation. For Sb-SiC, full oxidation was not achieved with oxygen pressures within the limits of the

Figure 6.2: *Evolution of the core level spectra of the (sub-)monolayer adsorbate atoms and oxygen taken with XPS on indenene, bismuthene and Sb-SiC samples after exposure to increasing oxygen dosages. With increasing oxygen dosage, additional peaks appear in the adsorbate core level spectra at higher binding energies indicating the oxidation of the (sub-)monolayer materials. Consequently, the intensity of the core level signal of oxygen increases. For Sb, the O 1s binding energy cannot be investigated separately as it overlaps with the Sb 3d core level.*
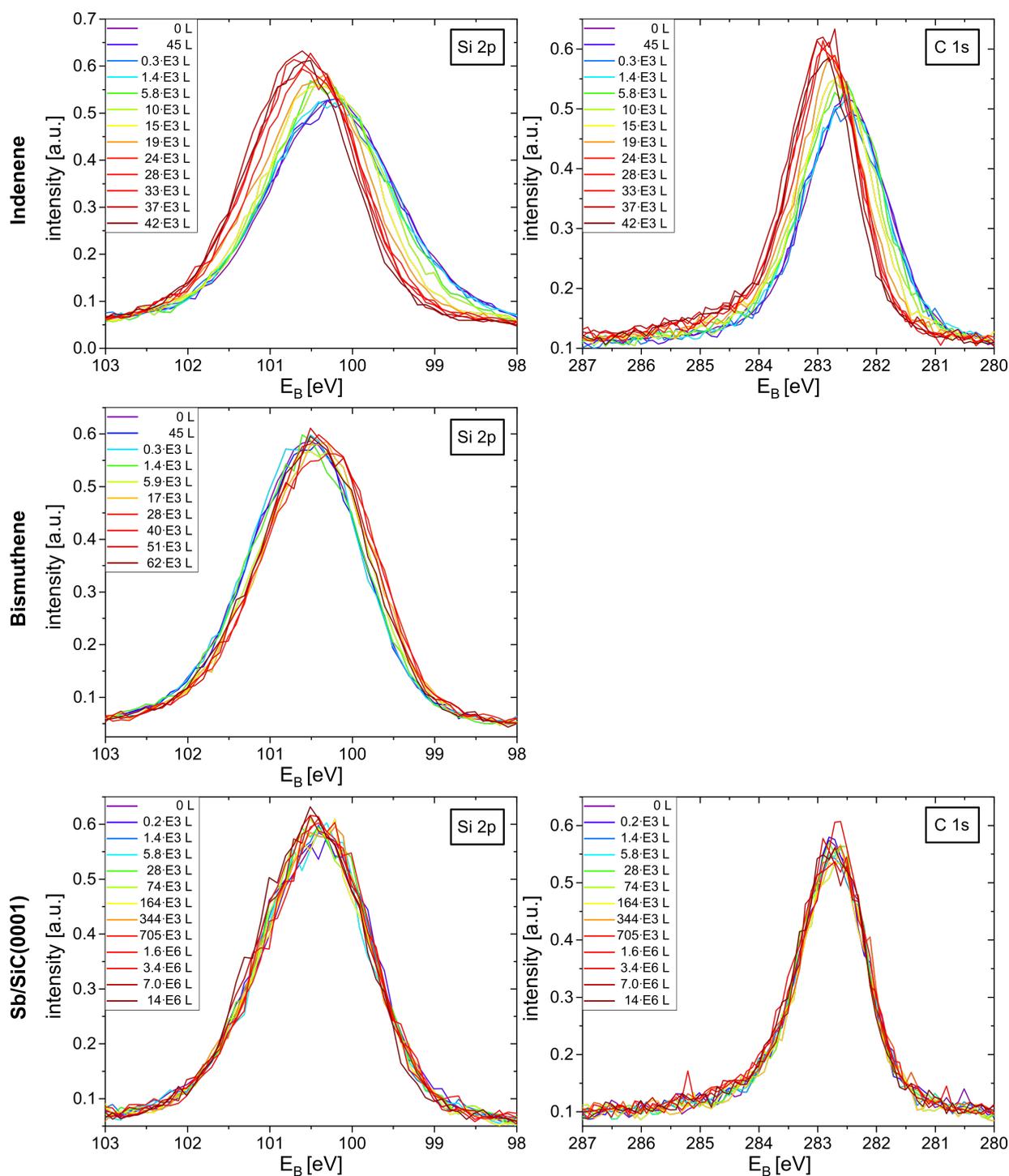
Figure 6.3: *Evolution of the core level spectra of the SiC substrate atoms taken with XPS on indenene, bismuthene and Sb-SiC samples after exposure to increasing oxygen dosages. With increasing oxygen dosage, the core levels of Si and C shift coherently to higher or lower binding energies for indenene/Sb-SiC and bismuthene, respectively. This shift is attributed to a dopant effect caused by the oxidation of the adsorbate layer.*

pressure gauge ($< 1.0 \cdot 10^{-2}$ mbar) and within a reasonable period of time. The steady decline of the pristine core level peak, however, does not show signs of saturation and indicates the potential for further oxidation.

After each oxidation step, core level binding energies of the SiC(0001) substrate (Si: $2p$ and C: $1s$), the (sub-)monolayer adsorbates (In/Sb: $3d$ & $3p$, Bi: $4f$ & $4d$) and oxygen (O: $1s$) were measured with XPS. Figure 6.2 and figure 6.3 display the evolution of each core level, normalized to the Si $2p$ substrate core level, with increasing oxygen exposure. Due to an overlap with the Sb $3d$ core level, a direct observation of the O $1s$ component for the Sb-SiC sample is not possible. No data was acquired for the C $1s$ core level of the bismuthene/SiC sample.

6.3 Core level evolution during oxidation

For the adsorbate atoms (In, Bi, Sb), the fine structure splitting of the $3d/4f$ core levels is well resolved, see figure 6.2. With progressing oxygen exposure, additional peaks emerge at higher binding energies and gain spectral weight with each oxidation step at the cost of the pristine adsorbate peaks. This shift of intensity can be attributed to the chemical interaction of oxygen with the adsorbate lattices. Binding energies of each adsorbate core level and the corresponding oxygen-related energy shifts are listed in table 6.2. Peak positions are extracted from spectra of pristine and fully oxidized samples, respectively, with a Voigt peak fitting procedure provided by SpecsLab Prodigy [133].

During fitting, the fine structure energy splitting and peak area ratios have been constrained to literature values [134]. For comparison, chemical shifts of the core level due to the oxidation of In, Bi and Sb have been extracted from the NIST database [135]. Within the error bars, see table 6.2, the XPS data of this work indicates the oxidation of the adsorbate lattices to mainly In_2O_3, Bi_2O_3 and Sb_2O_5 for the respective samples of indenene, bismuthene and Sb-SiC.

With increasing oxygen dosage, core level binding energies of the substrates Si $2p$ and C $1s$ shift alike by $+0.42$ eV, -0.14 eV and $+0.05$ eV for indenene, bismuthene and Sb-SiC, respectively. These shifts are too small to be explained with the oxidation of the substrate itself (chemical shift of Si $\rightarrow$ SiO_2: 4 eV [135]). They are therefore attributed to a change in chemical potential due to the interaction of the surface with oxygen. The chemical shifts

core level	pristine binding energy [eV]	oxidized binding energy [eV]	chemical shift [eV]	chemical shift (lit.) [eV]
In $3d_{5/2}$	443.479 ±0.004	444.877 ±0.003	0.972 ±0.005	0.98 ±0.59 (In_2O_3)
$3d_{3/2}$	450.979 ±0.004	452.377 ±0.003	0.972 ±0.005	
Bi $4f_{7/2}$	156.486 ±0.004	158.816 ±0.012	2.470 ±0.013	2.33 ±0.99 (Bi_2O_3)
$4f_{5/2}$	161.786 ±0.004	164.116 ±0.012	2.470 ±0.013	
Sb $3d_{5/2}$	527.870 ±0.004	530.882 ±0.006	2.962 ±0.007	1.92 ±0.32 (Sb_2O_3)
$3d_{3/2}$	537.170 ±0.004	540.182 ±0.006	2.962 ±0.007	3.24 ±0.92 (Sb_2O_5)

Table 6.2: *Table of binding energies for each (sub-)monolayer structure and the corresponding chemical shift. Binding energies for pristine and oxide core levels are extracted from the initial and final spectra of each oxidation study. The energy shift between pristine and oxide core levels are corrected for the overall shift observed for the substrate core levels. Chemical shifts from literature [135] are relative to the pristine bulk core level.*

of the adsorbate atoms listed in table 6.2 are corrected for this shift to solely display the effect of oxidation.

For the O $1s$ core level, no intensity is present for as-grown samples of indenene and bismuthene indicating pristine (sub-)monolayer lattices. For both samples, O $1s$ intensity builds up with increasing oxygen exposure for two separate core level components. Their binding energies are listed in table 6.3 alongside literature values. Peaks at lower binding energy (labeled #1) can be attributed to oxygen atoms that are involved in the oxidation of the (sub-)monolayer lattice to In_2O_3 and Bi_2O_3, in agreement with the observation of table 6.2. According to literature, components at higher binding energy (labeled #2) can either be attributed to oxygen molecules physisorbed to the substrate surface or to the low-temperature oxidation of substrate Si atoms [136], as there is hardly any difference in binding energy between both cases. Since there are no apparent signs of oxidation in the Si $2p$ spectra of figure 6.3, component #2 is attributed to physisorbed oxygen.

Besides the core level evolution with increasing oxygen dosage, the spectra of figure 6.2 allow to identify the oxygen pressure and dosage at which each adsorbate lattice shows first signs of oxidation, see table 6.4. Indenene is most sensitive to oxygen, followed by bismuthene and Sb-SiC. For all surface materials, the onset of oxidation is found to be significantly lower than the oxygen partial pressure of ambient atmosphere of 212 mbar.

	O 1s #1 binding energy [eV]	O 1s #2 binding energy [eV]
indenene	530.243 $\pm$ 0.035	531.92 $\pm$ 0.19
bismuthene	530.33 $\pm$ 0.17	532.03 $\pm$ 0.29
literature values	530.46 $\pm$ 0.74 (In_2O_3) 529.96 $\pm$ 0.25 (Bi_2O_3)	532.50 $\pm$ 0.41 (O_2/Si) 532.88 $\pm$ 0.30 (SiO_2)

Table 6.3: *Table of binding energies for both components of the O 1s core level for the indenene and bismuthene sample. Literature values [135] are given with their standard deviation.*

	$p_{O_2,initial}$ [mbar]	$d_{initial}$ [$\cdot 10^3$ L]	cumulative dosage [$\cdot 10^3$ L]
indenene	$(2.5 \pm 0.1) \cdot 10^{-6}$	1.128 $\pm$ 0.045	1.399 $\pm$ 0.046
bismuthene	$(1.0 \pm 0.1) \cdot 10^{-5}$	4.51 $\pm$ 0.45	5.91 $\pm$ 0.45
Sb-SiC	$(5.0 \pm 0.1) \cdot 10^{-5}$	22.56 $\pm$ 0.45	28.42 $\pm$ 0.64

Table 6.4: *Oxygen pressures, dosages and cumulative dosages after which first signs of oxidation are apparent for each (sub-)monolayer surface.*

6.4 Oxidation rates

The distribution of spectral weight among the pristine and oxide component of the adsorbate core levels is extracted from XPS spectra by means of a fitting procedure. Each spectrum is normalized to the Si 2p core level and satellite features of the non-monochromatized Al K$_\alpha$ light source, as well as an iterative Shirley background [62] are subtracted. The choice of normalization is based on the assumption that the substrates core level signal stays constant throughout the study. This is justified by the low (sub-)monolayer coverage of metal atoms which does not allow the formation of a thick metal-oxide layer that could significantly dampen the substrates photo electron intensity. For the sake of simplicity, fits to the XPS spectra only consist of features that are apparent by eye, namely pseudo-Voigt functions for each core level peak and the SiC plasmon loss peak at higher binding energy. For the pristine core levels of the metallic indenene lattice, a better fit was achieved with an asymmetric pseudo-Voigt function [137]. The peak area ratio of the pristine and oxidized adsorbate core levels have additionally been constraint to 4 : 3 (Bi 4$f_{7/2}$:4$f_{5/2}$) and

$3 : 2$ (In/Sb $3d_{5/2}$:$3d_{3/2}$) reflecting the respective multiplicity of the total angular momentum. Figure 6.4 exemplary shows fitted spectra of a pristine and partially oxidized sample including the distribution of spectral weight among all relevant features.
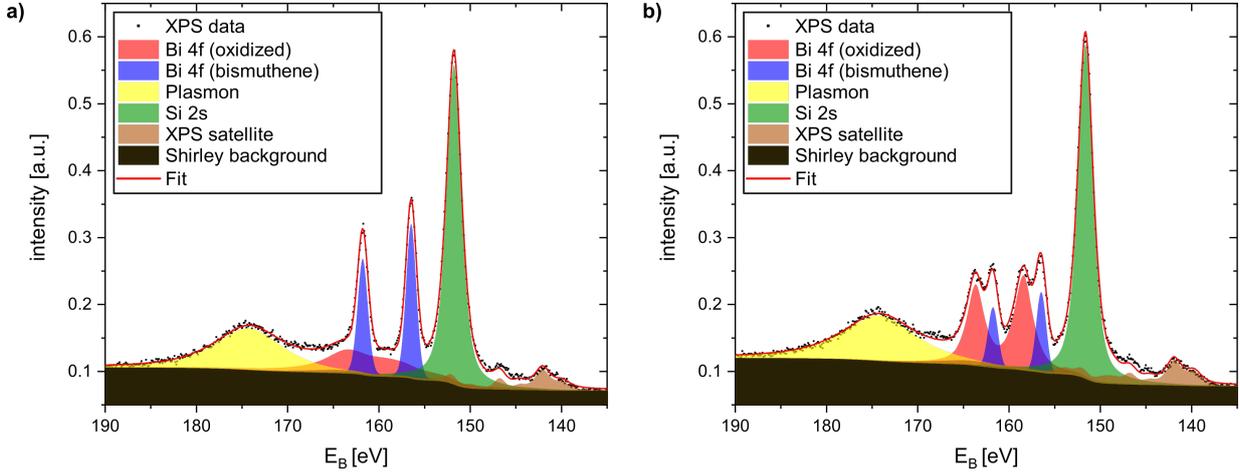
Figure 6.4: *a) and b) XPS spectrum of an as-grown and partially oxidized (step 6) bismuthene sample, respectively. The combined fit (red) is overlayed for both cases, including the distribution of spectral weight among the individual features.*

Each spectrum is fitted including peaks for the oxide core level in order to observe the onset of oxidation. For spectra with no apparent oxide peak, this approach consistently results in a finite intensity for the oxide peak, even for as-grown samples. This intensity is a result of the simplistic approach of the fitting process and derives from additional plasmon loss peaks which overlap with the core levels of the adsorbate lattice. Due to their unknown number and intensity we refrain to include them in the fitting process. However, in the following analysis, the finite intensity of the oxide core level measured on a pristine surface is treated as a constant background. This intensity is therefore subtracted from the oxide core level peak area of all spectra taken subsequently on the respective sample.

In the left panels of figure 6.5, the evolution of the spectral weight distribution between the initial and oxidized adsorbate core levels is plotted over oxygen dosage for each 2D material under investigation. The spectral weight is thereby normalized to that of the pristine adsorbate core level measured before oxidation. During the stepwise oxygen exposure, spectral weight is gradually shifted from pristine to oxide core levels for each sample. For a better visualization, but without physical meaning, the weight distribution curves are fitted with cumulative Weibull distribution functions. Full oxidation is achieved for indenene and bismuthene above 30000 L and 60000 L, respectively, which corresponds to a lifetime of
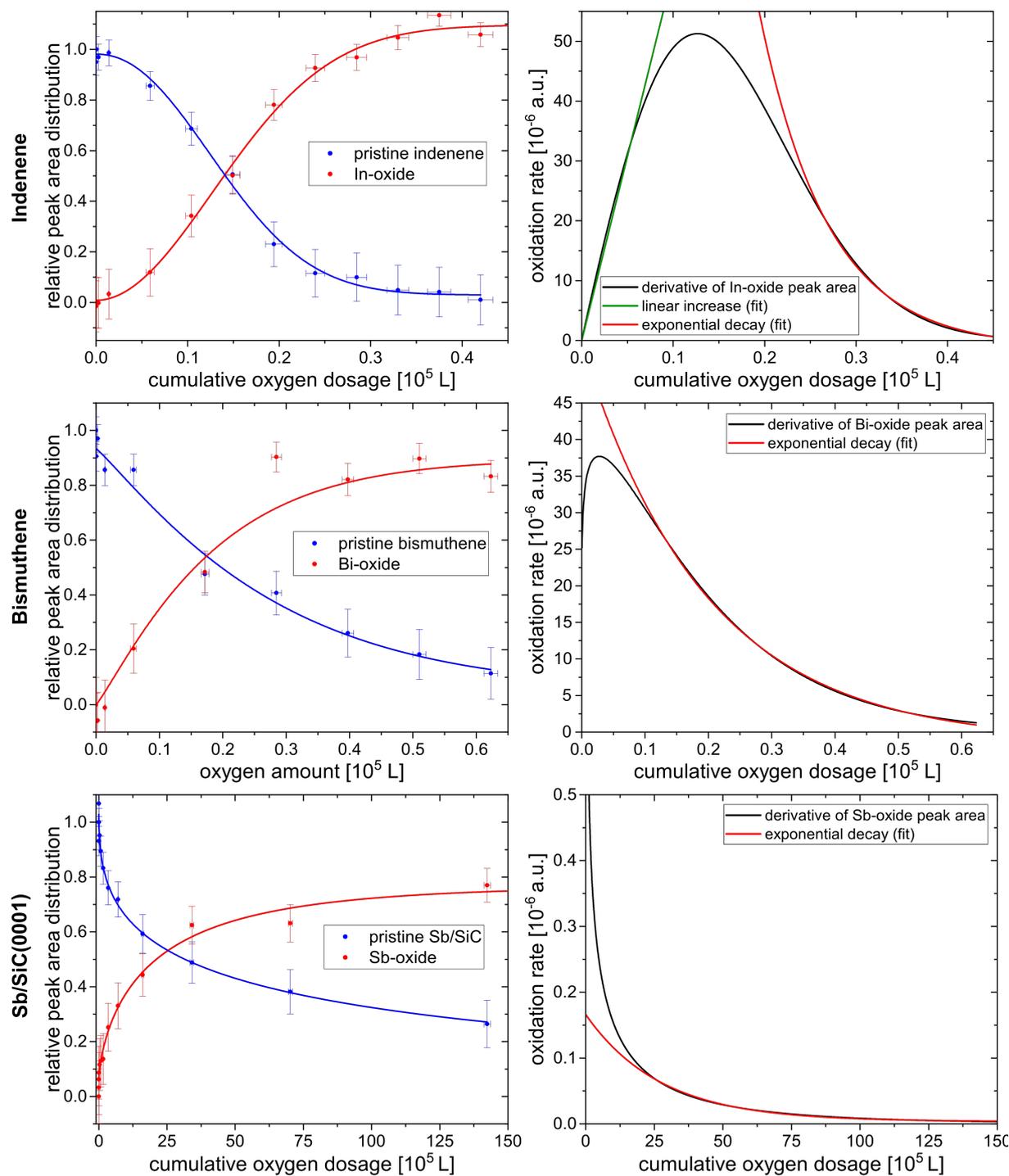
Figure 6.5: *Spectral weight distribution of pristine and oxidized adsorbate core level spectra as a function of oxygen dosage extracted via curve fitting from figure 6.2. For visualization, the data points are fitted with cumulative Weibull distribution functions. The data point for bismuthene at 28500 L deviates strongly from the observed trend and was thus excluded during curve fitting. The corresponding oxidation rates represent the derivative of the peak area distribution curves of the oxidized adsorbate. They can be fitted with linear and asymptotically decaying functions that represent the oxygen and adsorption speed limited cases of oxidation.*

the 2D material below < 1 ms under ambient conditions ($\mathrm{p}_{partial,O_2} = 212$ mbar). Due to the limited range of the pressure gauge in the oxidation chamber ($p_{max} < 1 * 10^{-2}$ mbar), the oxidation of Sb-SiC could not be investigated until full oxidation. As the weight distribution of the Sb core levels does not saturate, one can nevertheless assume that the oxidation is not yet finished and would have continued towards full oxidation as in the case of indenene or bismuthene. Overall, all (sub-)monolayer materials under investigation are prone to oxidation and can therefore be expected to be unstable under atmospheric conditions.

The weight distribution curve of the oxide core level additionally allows to extract the oxidation rate of each material, displayed in the right panels of figure 6.5. It is the derivative of the weight distribution curve and a measure for the oxidation pace. The overall line shape of the oxidation rate strongly differs between indenene and Sb-SiC which can be understood by taking into account the limiting factors during oxidation.

6.4.1 Theoretical concept

The process of oxidation requires the encounter of an oxygen molecule with an unoxidized adsorbate atom. The oxidation rate is therefore either limited by the number of oxygen atoms that impinge on the surface or, if sufficient oxygen molecules are available, by the adsorption speed S [138] of oxygen on the surface. The adsorption speed thereby depends on the probability of chemisorption and the availability of unoxidized adsorption sites.

In the case of an insufficient oxygen supply, the oxidation rate r_{oxi} should increase proportional to the number of oxygen molecules N_{O_2}. According to the kinetic theory of gases [139], N_{O_2} is proportional to the oxygen pressure p_{O_2} and therefore to the oxygen dosage

$$d_{O_2} = \int p_{O_2} dt \tag{6.1}$$

under the assumption of infinitesimal short exposure times dt. A linear dependency of the oxidation rate to the oxygen dosage is therefore a characteristic feature for the oxygen limited case of oxidation.

In case of a sufficient oxygen supply, the oxidation rate is limited by the the adsorption speed S [138, 140] which describes the probability of chemisorption of oxygen atoms to the
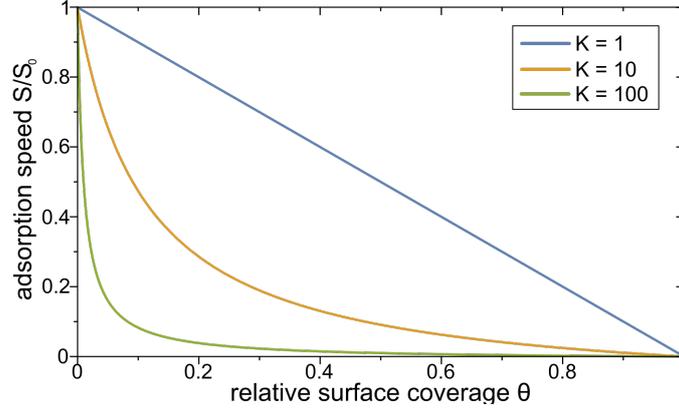
Figure 6.6: *Representation of the adsorption speed as the function of surface coverage for different values of the parameter K.*

adsorbate lattice. It is given by the equation

$$S(\Theta) = S_0(1 + \frac{\Theta}{1-\Theta}K)^{-1}.$$
(6.2)

S_0 denotes the initial adsorption speed of the pristine surface and Θ the relative surface coverage of the oxidized surface ranging from 0 (unoxidized) to 1 (fully oxidized). The constant K is dependent on the probabilities of chemisorption and desorption and is experimentally found to be > 1 [138]. $S(\Theta)$ is in general a monotonically decreasing function from S_0 to 0, as depicted in figure 6.6. The constant K indicates how fast the adsorption speed decays with increasing surface coverage. In the simple case of $K = 1$, the adsorption speed is proportional to $1 - \Theta$, whereas for values $K >> 1$, the adsorption speed declines quickly in the beginning and approaches 0 asymptotically towards full coverage.

A similar behavior can also be expected for the adsorption speed plotted against oxygen dosage, as measured in experiment, as the oxide coverage increases with dosage if not necessarily in a proportional way. This prevents the meaningful extraction of the parameter K, but does not impede the observation of a similar trend.

6.4.2 Oxidation rate in experiment

The oxygen- and adsorption-limited cases of the oxidation are well reproduced for indenene, as shown in figure 6.5. The oxidation rate initially increases linearly up to ≈ 5500 L, reaches a maximum at 12500 L and decreases asymptotically towards zero for larger oxygen

	$d_{initial}$ $[\cdot 10^3 \text{ L}]$	c_{decay} $[10^3 \text{ L}^{-1}]$
indenene	1.128 ± 0.045	7.5
bismuthene	4.51 ± 0.45	19.7
Sb-SiC	22.56 ± 0.45	2724.4

Table 6.5: *Initial oxygen dosage for oxidation $d_{initial}$ and decay constant c_{decay} for each (sub-)monolayer material.*

dosages. This line shape indicates that up to ≈ 5500 L, the oxidation is limited by the available number of oxygen atoms. For larger dosages, the oxidation rate gets limited by the adsorption speed. This results in an oxidation rate decay with an asymptotic behavior towards 0 for dosages above 20000 L, matching well with that expected for an adsorption speed limited oxidation. For bismuthene and Sb-SiC, the oxidation rate is entirely dominated by a monotonous asymptotic decay. The initial steep increase of the oxidation rate for bismuthene is thereby an artifact of the low number of data points of the weight distribution curve in figure 6.5 c) at low dosages. The absence of an oxygen-limited oxidation indicates that the absolute adsorption speed S of oxygen onto a bismuthene and Sb-SiC surface is lower compared to indenene and dominates the oxidation behavior even for oxygen dosages below 5500 L.

The adsorption speed can be quantified by fitting the oxidation rate with an asymptotically decaying function. For simplicity, an exponential decay was used for the fits in the right panels of figure 6.5. A fast decay of the oxidation rate thereby implies that the number of available sites of unoxidized adsorbate atoms diminishes rapidly. The decay constants of the different surfaces are displayed in table 6.5 alongside the oxidation threshold dosages. The results show that indenene features the smallest threshold dosage and the fastest decay of all samples under investigation which corroborates its strong oxidation susceptibility. Sb-SiC, on the other hand, resists oxidation the most with a decay constant of the oxidation rate almost three orders of magnitude larger than that of indenene.

6.5 Comparison with published results

The increased stability of Sb-SiC relative to indenene is in agreement with the observation made by Sen *et al.* [141] on bulk surfaces of both elements. The group reports that 5 ML

of In are oxidized after an exposure to an oxygen dosage of ≈ 100 L. The oxidation of the first monolayer of Sb wasn't realized until an exposure to ≈ 2300 L of oxygen. These values differ strongly to the results obtained within this work for our (sub-)monolayer materials which are fully oxidized after a much larger oxygen exposure of > 30000 L (In) and $> 10^7$ L (Sb). This strong difference in the oxidation susceptibility between bulk materials and their 2D counterparts can be explained on the basis of three factors. Firstly, the bonds within the adsorbate lattices and those to the substrate are completely different to those prevailing in the 3D bulk materials. The ensuing impact on the oxidation behavior is, however, impossible to isolate from other factors and can therefore not be quantified. Secondly, the inhomogeneous adlayer on the Sb-SC(0001) sample covers the Sb-(1×1) lattice and protects it from oxidation. A larger oxygen dosage is consequently required for its oxidation. Sen *et al.* report an increase of oxygen dosage for the oxidation of the second antimony layer of factor ≈ 10 which might also be an adequate estimate for the covered Sb-(1×1) reconstruction. And thirdly, we have ascertained a significant influence of the pressure gauge type of the oxidation chamber on the oxidation behavior. The presence of a hot cathode ion gauge for pressure observation was found to strongly accelerate oxidation as its hot filament splits oxygen molecules into more reactive atomic oxygen. The required dosage for the oxidation of bismuthene was consequently lowered by about two orders of magnitude compared to the oxidation involving a cold cathode ion gauge, see figure 6.7. In their publication, Sen *et al.* mention the use of a hot cathode ion gauge which can therefore be taken as the main cause for the observation of a significantly higher sensitivity of In and Sb to oxygen. As such it is impossible to make a meaningful comparison of their results to this work.

A comparison of the bismuthene oxidation with a similar study performed by Andreas Kuhn within his bachelor thesis [34] yields similar results regarding the sensitivity of bismuthene to oxygen, albeit with small differences regarding oxidation onset and speed. He observed first signs of oxidation already at dosages of about 440 L (this work: 4510 L) and an oxygen dosage required to oxidize 50% of the surface of ≈ 40000 L (this work: 17000 L). While similar, the differences between both studies indicate that detailed results from oxidation studies are difficult to reproduce due to a variety of parameters that influence the outcome. This includes the choice of pressure gauge, its distance to the sample, the method of oxygen exposure (static oxygen atmosphere *versus* oxygen flow) and the overall geometrical setup including gas inlet, sample position and oxygen flow. An insightful and detailed comparison regarding the oxidation behavior of different materials is therefore only possible if studies
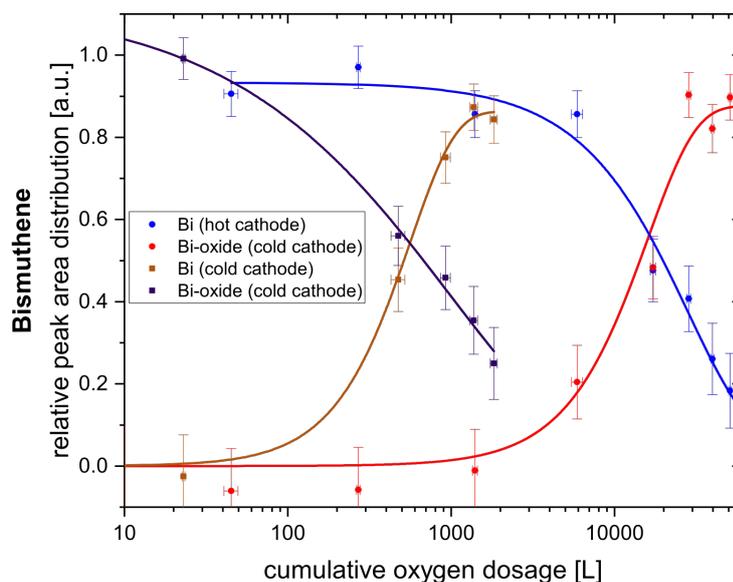
Figure 6.7: *Comparison of the oxidation behavior of bismuthene in the presence of a cold and hot cathode pressure gauge.*

are performed with a similar, if not identical, experimental setup, as done within this work for indenene, bismuthene and Sb-SiC.

6.6 Impact of oxidation on 2D atomic lattices

So far, the oxidation process has been solely investigated with XPS regarding general properties such as oxidation onset and oxidation rate. To additionally investigate the impact of oxidation on the structural level, indenene and bismuthene samples have been investigated with STM after partial oxidation. We exclude the Sb-SiC sample for this part of the analysis due to its mixed-phase surface and the concomitant impossibility in the assignment of any observable behavior to a certain surface structure. Figure 6.8 shows STM images of an indenene and bismuthene surface before oxidation (room temperature) and after oxidation (4 K). The oxygen dosage was chosen according to the results from figure 6.5 for an oxidation of the adsorbate lattices of about 50%.

Before oxidation, both (sub-)monolayer lattices cover the surface with domains of different sizes (figure 6.8 a)-b)). For this particular sample of indenene, domains are clearly separated from each other by regions of hydrogen terminated SiC. Clean bismuthene domains are of arbitrary shape with disordered patches in between. Despite a reduced resolution of
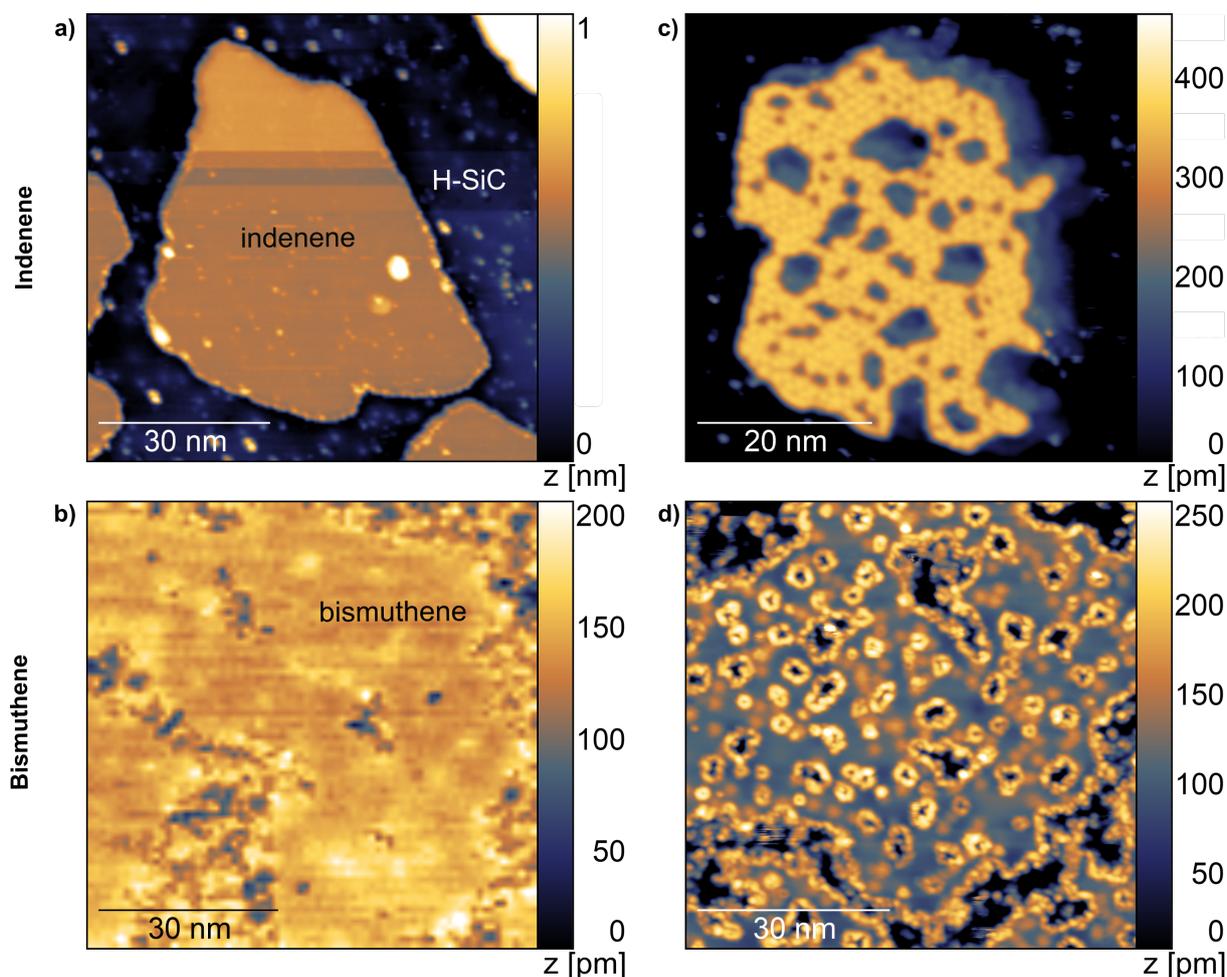
Figure 6.8: *STM topography images taken on indenene and bismuthene before (room temperature) and after partial oxidation with a subsequent anneal (4 K). Holes in the adsorbate domains indicate the irrevocable destruction of the pristine lattices by oxidation.*

the image due to a bad shape of the STM tip [1], the bismuthene lattice appears to be flat with some small holes inside the domains [similar to figure 6.1 e)]. The impact of oxygen on the adsorbate lattices can be seen in STM after annealing the samples which removes loosely bound adsorbates and allows to investigate the substrate surface, see figure 6.8 c) - d). The temperature of the anneal was thereby below the decomposition temperature of the adsorbate lattices. Changes in the lattice structure are therefore supposed to stem from the oxidation process.

After oxidation, indenene domains are reminiscent of the indenene islands in figure 6.8 a), but with tattered outlines, holes of various sizes and an irregular structure, see figure

---

[1]taken with a commercial variable temperature STM from Omicron Nanotechnology

6.8 c). While the indium coverage is apparently reduced, a significant amount of indium remains on the surface, even after the thermal treatment. The irregular structure of the remaining domain does not resemble indenene anymore but could potentially indicate the formation of a 2D phase of In-oxide. A 2D hexagonal monolayer of In_2O_3, which fits to our binding energy listed in table 6.3, has already been predicted theoretically as a stable phase of indium oxide [142]. The investigation and identification of this unknown atomic structure is, however, not within the scope of this work and requires future studies. For bismuthene, no bismuth-oxide structures are apparent after oxidation. Compared to the as-grown surface however, the oxygen-exposed bismuthene domains are homogeneously interspersed with holes of various sizes. The bismuthene lattice is therefore destroyed by oxidation and bismuth-oxide compounds subsequently desorbed from the surface by annealing.

The formation of holes in the lattice structures of both, indenene and bismuthene, provides further information about the oxidation process. Firstly, initial oxidation is not limited to the edge atoms of the domains which are stronger exposed than bulk atoms due to their incomplete bonding situation. A full (sub-)monolayer coverage of the surface therefore offers no additional protection against oxidation for both materials. Secondly, oxidized adsorbate atoms rather desorb than split their bond with oxygen. Both adsorbate reconstructions are therefore irreversibly destroyed by oxidation and cannot be recovered with a thermal treatment.

6.7 Protective measures against oxidation

The vulnerability of the adsorbate lattices to oxidation is disadvantageous as it prevents their direct implementation in future devices. It inevitably requires additional protective measures against oxidation during processing and/or application under ambient conditions. Samples either have to be processed in an inert atmosphere or be encapsulated to prevent direct contact to oxygen. First steps that have already been taken into these directions will be shortly discussed in the following.

6.7.1 Glove box environment

Maintaining an inert atmosphere requires an enclosed workspace with external access, such as a UHV setup or a glove box, which comes with severe downsides. The enclosure intrinsically limits and exacerbates operator-sample interaction and only offers local protection. It is, however, inevitable for the growth and initial processing of sensitive materials. In order to diversify the options for sample processing, Felix Reis already reported the stability of bismuthene outside a UHV setup in a dry nitrogen atmosphere [143] for 5 hours within his PhD thesis [143]. This work extends this study to include indenene and longer storage times.

For experiments, we used a glove box with dry nitrogen atmosphere accessible via a UHV compatible load-lock which allows a direct sample transfer after growth without contact to ambient conditions. In order to investigate the stability of the adsorbate lattices in nitrogen atmosphere, the core level spectra of as-grown indenene and bismuthene samples are investigated before and after storage inside the nitrogen atmosphere for different periods of time. During storage, the partial pressures of oxygen and water inside the glove box did not exceed $< 10^{-4}$ mbar. This upper limit corresponds to a maximum oxygen dosage of 9023 L, $1.35 \cdot 10^6$ L and $26.0 \cdot 10^6$ L for storage times of 2 min, 5 h and 4 d. Normalized spectra of the Bi $4f$, In $3d$ and O $1s$ core levels are displayed in figure 6.9.

Indium core levels show a partial oxidation already after a short storage of only 2 min. It manifests in an In core level shift towards higher binding energies and additional intensity in the core level signal of oxygen. After a 5 h storage inside the glove box, the In core levels are shifted to 453.13 eV ($3d_{3/2}$) and 445.57 eV ($3d_{5/2}$). This corresponds to a fully oxidized adsorbate layer according to table 6.2. In contrast to indenene, bismuthene does not show any signs of oxidation after a 5 h storage inside the nitrogen atmosphere. This is in agreement with the results shown by Felix Reis [143]. After four days of storage, however, a tiny signal of oxidized Bi and additional intensity of the O $1s$ core level can be detected in the XPS.

According to the oxygen study presented in sections 6.2 and 6.3, a fully oxidized adsorbate monolayer of indenene and bismuthene should be achieved after exposure to an oxygen dosage of about 30000 L and 60000 L, respectively. This corresponds to a glove box storage time below 15 min under the assumption that the oxidation behavior does not change significantly compared to that in a pure oxygen atmosphere. Intuitively, the nitrogen
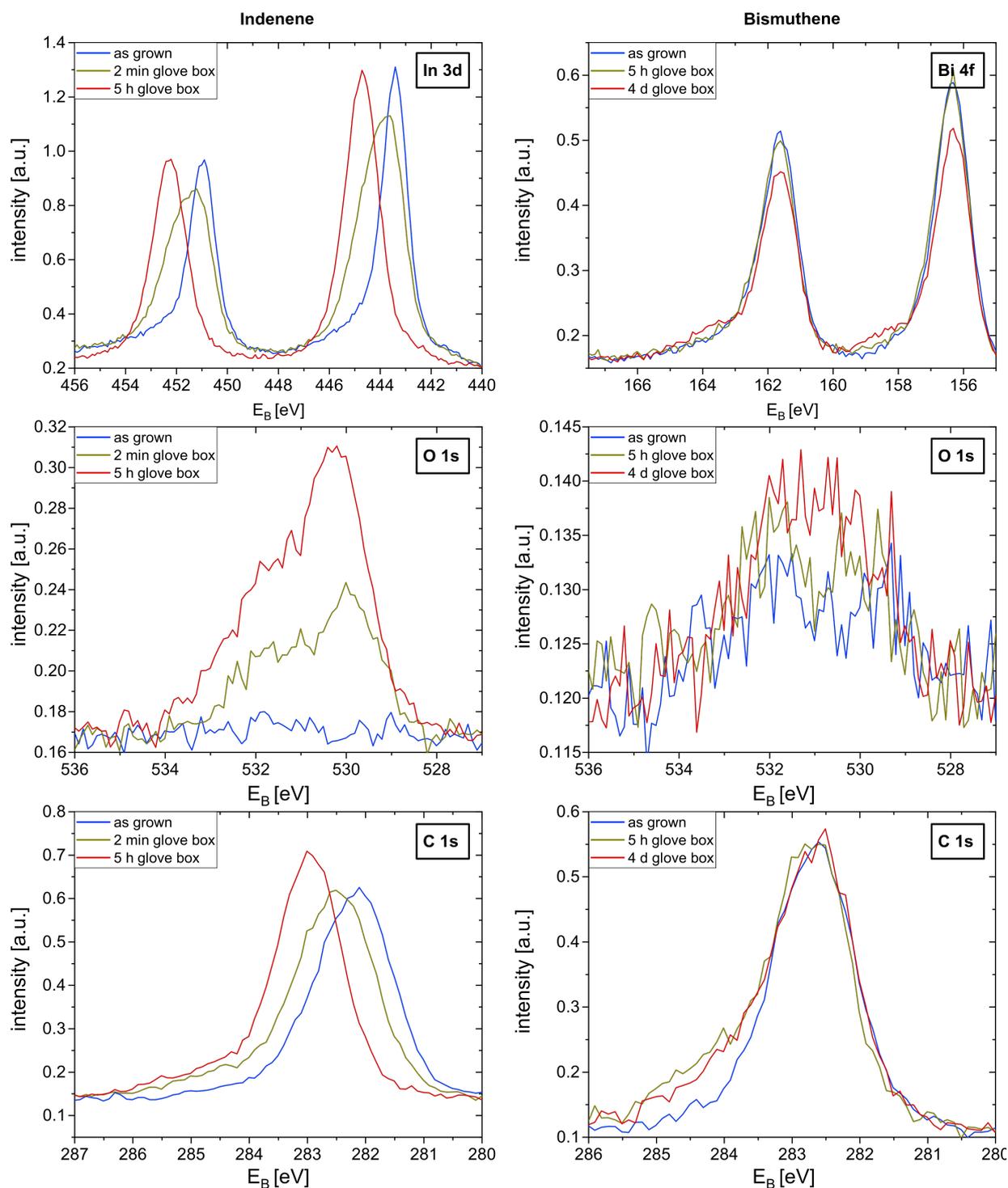
Figure 6.9: *Evolution of the core level spectra of the adsorbates and oxygen taken with XPS on indenene and bismuthene after storage in a dry nitrogen atmosphere for different periods of time. While indenene oxidizes within minutes despite the alleged protective atmosphere, bismuthene is protected from against oxidation for extended periods of time. A finite amount of O 1s signal was already detected on this bismuthene sample after growth, but did only increase insignificantly during a 4 day storage.*

atmosphere of the glove box can be expected to suppress the oxidation rate. While nitrogen molecules do not chemically react with the adsorbate layer, they nevertheless adsorb temporarily on the sample surface thereby reducing the number of available lattice sites for oxygen molecules. The longer the average nitrogen molecule stays on the surface, the lower the exchange rate of molecules on the surface which decreases the likelihood of oxidation. For indenene, the presence of nitrogen does not seem to have a significant protective effect as a considerable portion of the lattice is already oxidized after 2 min. The corresponding dosage of 9023 L is comparable to that required for the initial oxidation with pure oxygen. The oxidation of bismuthene, on the other hand, is strongly suppressed during under nitrogen atmosphere, albeit not completely prevented. This observation indicates a significantly longer adsorption time of nitrogen on the bismuthene surface compared to indenene.

Even though 78% of ambient atmosphere consists of nitrogen, it does not reproduce the protective effect observed inside the dry and almost oxygen-free environment of the glove box. Exposed to ambient conditions, bismuthene was found to be unstable by Felix Reis [143]. This can be attributed to the severely higher partial pressure of oxygen in ambient conditions (212 mbar) and to the presence of other reactive molecules, such as water, which themselves have the capability to oxidize or to catalyze oxidation [144].

All in all, a dry nitrogen atmosphere allows further and advanced processing of bismuthene outside an UHV setup whereas it does not suppress the oxidation of indenene. It deserves further studies to investigate if a protective effect for indenene might be achieved with other inert gases, e.g., with noble gases.

6.7.2 Surface capping

Instead of an inert atmosphere, substrate supported monolayers can also be protected against oxidation by an oxygen impenetrable capping layer. Ideal capping materials are chemically inert van der Waals compounds featuring a large band gap and do not alter or destroy the desired electronic properties of the underlying lattice, e.g., organic materials or hBN. In contrast to the stationary protection of a glove box, an adequate capping layer facilitates transport, storage and application of oxygen sensitive monolayer materials in devices under ambient conditions. It is therefore highly desirable to investigate and find potential candidates for suitable capping materials.

So far, first capping studies have been conducted on bismuthene with the organic materials tetratetracontane (TTC) and perylene by Johannes Weis within his master thesis [145]. Both were applied to the surface *in-situ* by thermal evaporation of the organic compound until a closed film was achieved. TTC was not deemed a suitable capping material as it was not possible to remove the capping layer without destroying the bismuthene lattice. For perylene, repeated cycles of capping and desorption have been performed without loosing the electronic properties of bismuthene. A protection against oxidation under ambient conditions was, however, only provided for a short amount of time, namely 6 min. After longer exposures to air, e.g. 60 min, a loss of most bismuth atoms was detected with XPS. Due to missing core level intensities for bismuth-oxide or oxygen, oxidation was ruled out as the reason for bismuth loss. However, taking into account that bismuth-oxide desorbs from the SiC surface at temperatures below the decomposition temperature of bismuthene, as seen in section 6.6, oxides molecules have most likely been removed during the thermal desorption of the capping layer. An insufficient protection of a perylene capping layer against the oxidation of bismuthene over a prolonged time period is therefore likely.

Additional to organic capping layers, first capping studies have been conducted with exfoliated hBN sheets on bismuthene and indenene within the master thesis of Jan Wittemann [146]. The hBN exfoliation and application took place under glove box conditions in a dry nitrogen atmosphere. First results indicate that hBN is not a suitable capping material as both surface materials degraded after exposure to ambient conditions. While for indenene, this observation might already be a consequence of the glove box atmosphere, the oxidation of bismuthene suggests a lack of protection.

So far, all attempts to achieve a long-lasting protective capping layer for indenene and bismuthene have not been successful. The perylene capping of bismuthene nevertheless provides a short term protection against oxidation and the possibility to recover the pristine surface. This finding encourages further studies with capping layers consisting of comparable organic compounds.

6.8 Conclusion

In summary, (sub-)monolayer lattices of indenene, bismuthene and Sb-SiC, are found to be unstable against oxidation by forming their native oxides In_2O_3, Bi_2O_3 and Sb_2O_5, respectively. A comparison between the atomic species regarding oxidation behavior reveals

differences in the oxidation sensitivity and speed. Indenene was found to be most sensitive to oxygen with first signs of oxidation after exposure to dosages of 1128 L and the highest oxygen adsorption speed of all materials under investigation. Despite being the least sensitive to oxygen with a threshold dosage of 22560 L and a significantly lower adsorption speed, even the Sb-SiC surface did not resist oxidation. STM images of partially oxidized indenene and bismuthene surfaces after annealing reveal a loss of adsorbate atoms. The lattices are therefore irrevocably destroyed by oxidation. These findings exclude the application of these surface materials in common devices without a proper protection against oxidation. For further processing, bismuthene was found to be stable outside UHV conditions in a dry nitrogen atmosphere for a prolonged period, unlike indenene. A protection against oxidation was additionally found for a removable organic capping layer of perylene, but its protective effect was only short-lived. Reliable protective measures to enable the implementation of these surface materials in everyday applications therefore require further extensive studies.

7 Conclusion

Within this thesis, structural and electronic properties of 2D antimony on different substrates have been investigated with a combined study of surface sensitive techniques (LEED, STM, ARPES, XPS, STEM). Depending on the substrate and its interaction with Sb, entirely different atomic lattices could be identified. Sb is incorporated into the surface layer of Ag(111) and forms a metallic $(\sqrt{3} \times \sqrt{3})R30°$ Ag_2Sb surface alloy. On InSb(111)A, Sb forms layered triangular islands down to the monolayer limit which do not adapt to the substrates lattice periodicity and but form a moiré superstructure at the interface. And lastly, the SiC(0001) substrate was found to host two different Sb-induced surface reconstructions. A buried triangular Sb-(1×1), similar to the topological insulator indenene/SiC(0001) [93], and an asymmetric surface kagome lattice. As diverse as the atomic lattices are the electronic properties associated with them. They range from metallic to insulating with interesting features such as flat bands and potential topological non-trivial Dirac cones. In addition, the stability of the Sb-SiC(0001) surface against oxidation was found to be superior to those of related materials bismuthene/SiC(0001) [13, 33] and indenene/SiC(0001) [93].

Ag_2Sb surface alloy

The Sb-induced surface of Ag(111) was proclaimed as a suitable substrate for the growth of antimonene by two different groups [41, 42] without them investigating the corresponding electronic properties. Within this work, we were able to reproduce the surface structure reported by Mao *et al.* [41] but did not find evidence for the formation of a buckled antimonene layer. Instead, ARPES measurements reveal two hole pockets centered around Γ that resemble those observed previously for the Ag_2Sb surface alloy. XSW measurements confirm the presence of a single adsorption site of Sb on the Ag(111) surface, further supporting the presence of an Ag_2Sb surface. Despite using similar growth parameter as those

reported by Shao *et al.* [42], we did not observe any indications for a planar antimonene lattice in STM or ARPES. The absence of experimental evidence for the formation of antimonene on Ag(111) is in agreement with a recent experimental study by Zhang *et al.* [147] which rules out the formation of antimonene on Ag(111). The Ag(111) is therefore not suitable for the investigation of structural or electronic properties of antimonene.

Moiré system Sb-InSb(111)A

The 7% mismatch of Sb(111) and InSb(111) lattices causes a 3D growth behavior of Sb islands on the In-terminated InSb(111) surface in which the Sb islands keep their bulk lattice periodicity. As a consequence of the lattice mismatch at the interface, a moiré superstructure arises with a unit cell size of 16.85 nm. The locally varying interaction between Sb layers and substrate manifests, on the one hand, in a periodic height modulation of the Sb films and, on the other hand, in a periodic modulation of the LDOS. Thickness-dependent electronic properties of the Sb surface state can be extracted by the investigation of interference patterns in between adjacent parallel terrace steps with STS. With decreasing thickness, the topologically non-trivial Dirac point of bulk Sb(111) is observed to shift towards lower binding energies. This shift is also prevalent in accompanying DFT calculations that tackle the moiré supercell with a local approach. Theoretical band structures thereby predict the opening of a band gap below 4 BL thickness which potentially indicates the transition of the Sb layers to a quantum spin Hall phase. Experimentally, the investigation of electronic properties is aggravated for thin Sb layers as the moiré situation at the interface increasingly influences measurements. It is therefore yet to be determined experimentally if such a topologically non-trivial phase is indeed established at low thicknesses, e.g., by searching for robust edge states. In addition, the influence of the moiré situation on the electronic properties of the system is so far unknown due to the local approach taken with DFT. Alternative theoretical approaches which consider the entire supercell, such as tight binding calculations, are therefore necessary for a better understanding of the global properties of this novel material.

Sb reconstructions on SiC(0001)

By means of ARPES and STEM measurements, a triangular Sb-(1×1) phase is identified on SiC(0001) which is buried below an inhomogeneous antimony adlayer. It is structurally

identical to the topological insulator indenene/SiC(0001) with Sb atoms sitting atop surface Si atoms on T1 adsorption sites. It is therefore expected to show similar features and properties in its electronic states, with bands shifted towards higher binding energies due to the higher electron count of Sb [107]. ARPES measurements confirm these predictions and reveal four linearly dispersing metallic bands around the Fermi level and a pronounced flat band at higher binding energies. The topologically non-trivial Dirac cone, however, could not be resolved experimentally due to a poor signal quality. Discrepancies between theory and experiment have been observed regarding the positioning of different bands in energy which might be attributed to the influence of the inhomogeneous adlayer. It remains unknown why this layer is unavoidably present and if it might even be required to stabilize the Sb-(1×1) lattice.

Upon annealing the buried Sb-(1×1) evolves into exposed domains with a 2×2 periodicity. Their lattice could be identified on the basis of its electronic structure. It consist out of an asymmetric kagome lattice of Sb atoms. The asymmetry is thereby owed to the reduced symmetry of the substrate which induces a size difference for neighboring triangles building up the kagome lattice. Due to the bonding with the substrate, pz states are strongly localized and pulled into the occupied states. The low-energy regime is therefore governed by in-plane states, similar to related systems indenene [93] and bismuthene [51]. Around the Fermi level, these states show a large hybridization band gap of about 650 meV rendering the material insulating. Due to the in- and out-of-plane symmetry breaking of the substrate, the presence of substrate bulk bands as well as the intrinsically large atomic SOC of Sb, the prototypical band structure of a kagome lattice cannot be readily identified for this system. The Sb lattice nevertheless represents the very first realized elemental surface kagome lattice and is therefore of interest for further investigations. The atomic structure has so far only been determined by a comparison of ARPES and DFT data and lacks a direct structural observation by, e.g., atomic force microscopy. Regarding the investigation of the electronic structure, it might be beneficial for the signal quality to investigate the material on an advanced light source with superior resolution and smaller beam spot size.

Oxidation behavior of elemental monolayers

By means of a controlled oxidation study inside of an UHV setup, the resilience against oxidation of related 2D monolayer materials on SiC(0001) (Sb-SiC, indenene and bismuthene) has been investigated. All materials are found to be sensitive to oxidation and become fully

oxidized if exposed to a sufficient dosage of pure oxygen. Indenene thereby exhibits the strongest vulnerability towards oxidation with a threshold dosage of 1128 L and a fast-paced oxidation of the entire monolayer. Bismuthene is only marginally more resistive against oxidation but was found to be stable in a dry nitrogen atmosphere. The most stable element of this series is Sb with a threshold dosage of 22560 L. Its oxidation behavior can, however, not be attributed to a certain Sb phase on SiC(0001) but to all phases combined, including the inhomogeneous adlayer of the Sb-(1×1). Attempts to recover the pristine monolayer after oxidation by providing thermal energy failed and irrevocably destroyed the adsorbate lattices. This study shows that an adequate protection is required to utilize these surface monolayer materials for future applications which is yet to be found.

Bibliography

[1] K. S. Novoselov, A. K. Geim, S. V. Morozov, D. Jiang, Y. Zhang, S. V. Dubonos, I. V. Grigorieva, and A. A. Firsov, "Electric field effect in atomically thin carbon films," *Science*, vol. 306, pp. 666–669, Oct. 2004.

[2] N. R. Glavin, R. Rao, V. Varshney, E. Bianco, A. Apte, A. Roy, E. Ringe, and P. M. Ajayan, "Emerging applications of elemental 2D materials," *Adv. Mater.*, vol. 32, p. 1904302, Feb. 2020.

[3] W. Gao, Z. Zheng, P. Wen, N. Huo, and J. Li, "Novel two-dimensional monoelemental and ternary materials: growth, physics and application," *Nanophotonics*, vol. 9, no. 8, pp. 2147–2168, 2020.

[4] L. Song, L. Ci, H. Lu, P. B. Sorokin, C. Jin, J. Ni, A. G. Kvashnin, D. G. Kvashnin, J. Lou, B. I. Yakobson, and P. M. Ajayan, "Large scale growth and characterization of atomic hexagonal boron nitride layers," *Nano Lett.*, vol. 10, pp. 3209–3215, Aug. 2010.

[5] C. R. Dean, A. F. Young, I. Meric, C. Lee, L. Wang, S. Sorgenfrei, K. Watanabe, T. Taniguchi, P. Kim, K. L. Shepard, and J. Hone, "Boron nitride substrates for high-quality graphene electronics," *Nature Nanotechnology*, vol. 5, no. 10, pp. 722–726, 2010.

[6] R. Mas-Ballesté, C. Gómez-Navarro, J. Gómez-Herrero, and F. Zamora, "2D materials: to graphene and beyond," *Nanoscale*, vol. 3, no. 1, pp. 20–30, 2011.

[7] M. Chhowalla, H. S. Shin, G. Eda, L.-J. Li, K. P. Loh, and H. Zhang, "The chemistry of two-dimensional layered transition metal dichalcogenide nanosheets," *Nature Chemistry*, vol. 5, no. 4, pp. 263–275, 2013.

[8] G. R. Bhimanapati, Z. Lin, V. Meunier, Y. Jung, J. Cha, S. Das, D. Xiao, Y. Son, M. S. Strano, V. R. Cooper, L. Liang, S. G. Louie, E. Ringe, W. Zhou, S. S. Kim, R. R. Naik, B. G. Sumpter, H. Terrones, F. Xia, Y. Wang, J. Zhu, D. Akinwande, N. Alem, J. A. Schuller, R. E. Schaak, M. Terrones, and J. A. Robinson, "Recent advances in two-dimensional materials beyond graphene," *ACS Nano*, vol. 9, pp. 11509–11539, Dec. 2015.

[9] J. Qiao, X. Kong, Z.-X. Hu, F. Yang, and W. Ji, "High-mobility transport anisotropy and linear dichroism in few-layer black phosphorus," *Nature Communications*, vol. 5, no. 1, p. 4475, 2014.

[10] H. Liu, A. T. Neal, Z. Zhu, Z. Luo, X. Xu, D. Tománek, and P. D. Ye, "Phosphorene: An unexplored 2D semiconductor with a high hole mobility," *ACS Nano*, vol. 8, pp. 4033–4041, Apr. 2014.

[11] P. Vogt, P. De Padova, C. Quaresima, J. Avila, E. Frantzeskakis, M. C. Asensio, A. Resta, B. Ealet, and G. Le Lay, "Silicene: Compelling experimental evidence for graphenelike two-dimensional silicon," *PRL*, vol. 108, p. 155501, Apr. 2012.

[12] J. Yuhara, B. He, N. Matsunami, M. Nakatake, and G. Le Lay, "Graphene's latest cousin: Plumbene epitaxial growth on a "nano watercube"," *Adv. Mater.*, vol. 31, p. 1901017, July 2019.

[13] F. Reis, G. Li, L. Dudy, M. Bauernfeind, S. Glass, W. Hanke, R. Thomale, J. Schäfer, and R. Claessen, "Bismuthene on a SiC substrate: A candidate for a high-temperature quantum spin hall material," *Science*, 2017.

[14] S. Dongre S, R. Shwetharani, C. Hunsur Ravikumar, C. Lavanya, and R. G. Balakrishna, "Review on 2D arsenene and antimonene: Emerging materials for energy, electronic and biological applications," *Adv. Mater. Interfaces*, vol. 9, p. 2200442, Aug. 2022.

[15] X. Qian, J. Liu, L. Fu, and J. Li, "Quantum spin hall effect in two-dimensional transition metal dichalcogenides," *Science*, vol. 346, pp. 1344–1347, Dec. 2014.

[16] C.-Z. Chang, J. Zhang, X. Feng, J. Shen, Z. Zhang, M. Guo, K. Li, Y. Ou, P. Wei, L.-L. Wang, Z.-Q. Ji, Y. Feng, S. Ji, X. Chen, J. Jia, X. Dai, Z. Fang, S.-C. Zhang, K. He, Y. Wang, L. Lu, X.-C. Ma, and Q.-K. Xue, "Experimental observation of the quantum anomalous hall effect in a magnetic topological insulator," *Science*, vol. 340, pp. 167–170, Apr. 2013.

[17] X. Jiang, Q. Liu, J. Xing, N. Liu, Y. Guo, Z. Liu, and J. Zhao, "Recent progress on 2D magnets: Fundamental mechanism, structural design and modification," *Applied Physics Reviews*, vol. 8, p. 031305, July 2021.

[18] D. Qiu, C. Gong, S. Wang, M. Zhang, C. Yang, X. Wang, and J. Xiong, "Recent advances in 2D superconductors," *Adv. Mater.*, vol. 33, p. 2006124, May 2021.

[19] C. L. Kane and E. J. Mele, "Z_2 topological order and the quantum spin hall effect," *Phys. Rev. Lett.*, vol. 95, p. 146802, Sep 2005.

[20] C. L. Kane and E. J. Mele, "Quantum spin hall effect in graphene," *Phys. Rev. Lett.*, vol. 95, p. 226801, Nov 2005.

[21] M. Z. Hasan and C. L. Kane, "Colloquium: Topological insulators," *Rev. Mod. Phys.*, vol. 82, pp. 3045–3067, Nov 2010.

[22] B. A. Bernevig, T. L. Hughes, and S.-C. Zhang, "Quantum spin hall effect and topological phase transition in HgTe quantum wells," *Science*, vol. 314, pp. 1757–1761, Dec. 2006.

[23] J. Haruyama, "Quantum-spin-hall phases and 2D topological insulating states in atomically thin layers," *Journal of Applied Physics*, vol. 129, p. 090902, Mar. 2021.

[24] K. Momma and F. Izumi, "Vesta: a three-dimensional visualization system for electronic and structural analysis," *Journal of Applied Crystallography*, vol. 41, pp. 653–658, Jun 2008.

[25] M. E. Dávila, L. Xian, S. Cahangirov, A. Rubio, and G. Le Lay, "Germanene: a novel two-dimensional germanium allotrope akin to graphene and silicene," *New Journal of Physics*, vol. 16, no. 9, p. 095002, 2014.

[26] F.-f. Zhu, W.-j. Chen, Y. Xu, C.-l. Gao, D.-d. Guan, C.-h. Liu, D. Qian, S.-C. Zhang, and J.-f. Jia, "Epitaxial growth of two-dimensional stanene," *Nature Materials*, vol. 14, no. 10, pp. 1020–1025, 2015.

[27] A. Molle, J. Goldberger, M. Houssa, Y. Xu, S.-C. Zhang, and D. Akinwande, "Buckled two-dimensional xene sheets," *Nature Materials*, vol. 16, p. 163, Jan. 2017.

[28] X.-L. Yu, L. Huang, and J. Wu, "From a normal insulator to a topological insulator in plumbene," *Phys. Rev. B*, vol. 95, p. 125113, Mar 2017.

[29] X.-L. Yu and J. Wu, "Evolution of the topological properties of two-dimensional group IVA materials and device design," *Phys. Chem. Chem. Phys.*, vol. 20, no. 4, pp. 2296–2307, 2018.

[30] J. L. Zhang, S. Zhao, S. Sun, H. Ding, J. Hu, Y. Li, Q. Xu, X. Yu, M. Telychko, J. Su, C. Gu, Y. Zheng, X. Lian, Z. Ma, R. Guo, J. Lu, Z. Sun, J. Zhu, Z. Li, and W. Chen, "Synthesis of monolayer blue phosphorus enabled by silicon intercalation," *ACS Nano*, vol. 14, pp. 3687–3695, Mar. 2020.

[31] P. Vishnoi, M. Mazumder, S. K. Pati, and C. N. R. Rao, "Arsenene nanosheets and nanodots," *New J. Chem.*, vol. 42, no. 17, pp. 14091–14095, 2018.

[32] T. Lei, C. Liu, J.-L. Zhao, J.-M. Li, Y.-P. Li, J.-O. Wang, R. Wu, H.-J. Qian, H.-Q. Wang, and K. Ibrahim, "Electronic structure of antimonene grown on Sb2Te3 (111) and Bi2Te3 substrates," *Journal of Applied Physics*, vol. 119, no. 1, p. 015302, 2016.

[33] R. Stühler, F. Reis, T. Müller, T. Helbig, T. Schwemmer, R. Thomale, J. Schäfer, and R. Claessen, "Tomonaga-luttinger liquid in the edge channels of a quantum spin hall insulator," *Nature Physics*, vol. 16, no. 1, pp. 47–51, 2020.

[34] A. Kuhn, "Adsorptionsverhalten von bismuthene unter O2-atmosphäre," bachelor thesis, Julius-Maximilians-Universität Würzburg, Sept. 2017.

[35] G. Yao, Z. Luo, F. Pan, W. Xu, Y. P. Feng, and X.-s. Wang, "Evolution of topological surface states in antimony ultra-thin films," *Scientific Reports*, vol. 3, no. 1, p. 2010, 2013.

[36] K.-H. Jin, H. W. Yeom, and S.-H. Jhi, "Band structure engineering of topological insulator heterojunctions," *PRB*, vol. 93, p. 075308, Feb. 2016.

[37] S. H. Kim, K.-H. Jin, J. Park, J. S. Kim, S.-H. Jhi, and H. W. Yeom, "Topological phase transition and quantum spin hall edge states of antimony few layers," *Scientific Reports*, vol. 6, p. 33193, Sept. 2016.

[38] C. Gibaja, D. Rodriguez-San-Miguel, P. Ares, J. Gómez-Herrero, M. Varela, R. Gillen, J. Maultzsch, F. Hauke, A. Hirsch, G. Abellán, and F. Zamora, "Few-layer antimonene by liquid-phase exfoliation," *Angewandte Chemie (International Ed. in English)*, vol. 55, pp. 14345–9, Nov 2016.

[39] X. Wu, Y. Shao, H. Liu, Z. Feng, Y. Wang, J. Sun, C. Liu, J. Wang, Z. Liu, S. Zhu, Y. Wang, S. Du, Y. Shi, K. Ibrahim, and H. Gao, "Epitaxial growth and air stability of monolayer antimonene on PdTe2," *Advanced Materials*, vol. 29, no. 11, p. 1605407, 2017.

[40] M. Fortin-Deschênes, O. Waller, T. O. Mente, A. Locatelli, S. Mukherjee, F. Genuzio, P. L. Levesque, A. Hébert, R. Martel, and O. Moutanabbir, "Synthesis of antimonene on germanium," *Nano Letters*, vol. 17, no. 8, pp. 4970–4975, 2017.

[41] Y.-H. Mao, L.-F. Zhang, H.-L. Wang, H. Shan, X.-F. Zhai, Z.-P. Hu, A.-D. Zhao, and B. Wang, "Epitaxial growth of highly strained antimonene on Ag(111)," *Frontiers of Physics*, vol. 13, p. 138106, Apr 2018.

[42] Y. Shao, Z.-L. Liu, C. Cheng, X. Wu, H. Liu, C. Liu, J.-O. Wang, S.-Y. Zhu, Y.-Q. Wang, D.-X. Shi, K. Ibrahim, J.-T. Sun, Y.-L. Wang, and H.-J. Gao, "Epitaxial growth of flat antimonene monolayer: A new honeycomb analogue of graphene," *Nano Letters*, vol. 18, no. 3, pp. 2133–2139, 2018.

[43] M. Pumera and Z. Sofer, "2D monoelemental arsenene, antimonene, and bismuthene: Beyond black phosphorus," *Advanced Materials*, vol. 29, no. 21, p. 1605299, 2017.

[44] M. Zhao, X. Zhang, and L. Li, "Strain-driven band inversion and topological aspects in antimonene," *Scientific Reports*, vol. 5, p. 16108, 11 2015.

[45] Z.-Q. Huang, C.-H. Hsu, F.-C. Chuang, Y.-T. Liu, H. Lin, W.-S. Su, V. Ozolins, and A. Bansil, "Strain driven topological phase transitions in atomically thin films of group IV and V elements in the honeycomb structures," *New Journal of Physics*, vol. 16, no. 10, p. 105018, 2014.

[46] F.-C. Chuang, C.-H. Hsu, C.-Y. Chen, Z.-Q. Huang, V. Ozolins, H. Lin, and A. Bansil, "Tunable topological electronic structures in Sb(111) bilayers: A first-principles study," *Applied Physics Letters*, vol. 102, no. 2, p. 022424, 2013.

[47] P. Zhang, Z. Liu, W. Duan, F. Liu, and J. Wu, "Topological and electronic transitions in a Sb(111) nanofilm: The interplay between quantum confinement and surface effect," *Phys. Rev. B*, vol. 85, p. 201410, May 2012.

[48] S. Sun, T. Yang, Y. Z. Luo, J. Gou, Y. Huang, C. Gu, Z. Ma, X. Lian, S. Duan, A. T. S. Wee, M. Lai, J. L. Zhang, Y. P. Feng, and W. Chen, "Realization of a buckled antimonene monolayer on Ag(111) via surface engineering," *J. Phys. Chem. Lett.*, vol. 11, pp. 8976–8982, Nov. 2020.

[49] S.-Y. Zhu, Y. Shao, E. Wang, L. Cao, X.-Y. Li, Z.-L. Liu, C. Liu, L.-W. Liu, J.-O. Wang, K. Ibrahim, J.-T. Sun, Y.-L. Wang, S. Du, and H.-J. Gao, "Evidence of topological edge states in buckled antimonene monolayers," *Nano Lett.*, vol. 19, pp. 6323–6329, Sept. 2019.

[50] K. Holtgrewe, S. K. Mahatha, P. M. Sheverdyaeva, P. Moras, R. Flammini, S. Colonna, F. Ronci, M. Papagno, A. Barla, L. Petaccia, Z. S. Aliev, M. B. Babanly, E. V. Chulkov, S. Sanna, C. Hogan, and C. Carbone, "Topologization of β-antimonene on Bi2Se3 via proximity effects," *Scientific Reports*, vol. 10, no. 1, p. 14619, 2020.

[51] G. Li, W. Hanke, E. M. Hankiewicz, F. Reis, J. Schäfer, R. Claessen, C. Wu, and R. Thomale, "Theoretical paradigm for the quantum spin hall effect at high temperatures," *Phys. Rev. B*, vol. 98, p. 165146, Oct 2018.

[52] G. Binnig, H. Rohrer, C. Gerber, and E. Weibel, "Surface studies by scanning tunneling microscopy," *Phys. Rev. Lett.*, vol. 49, pp. 57–61, Jul 1982.

[53] R. Wiesendanger, *Scanning Probe Microscopy and Spectroscopy*. The Press Syndicate of the University of Cambridge, 1994.

[54] L. Jones, S. Wang, X. Hu, S. Ur Rahman, and M. R. Castell, "Maximising the resolving power of the scanning tunneling microscope.," *Advanced structural and chemical imaging*, vol. 4, p. 7, 2018.

[55] A. M. J. den Haan, G. H. C. J. Wijts, F. Galli, O. Usenko, G. J. C. van Baarle, D. J. van der Zalm, and T. H. Oosterkamp, "Atomic resolution scanning tunneling microscopy in a cryogen free dilution refrigerator at 15 mK," *Review of Scientific Instruments*, vol. 85, p. 035112, Mar. 2014.

[56] R. J. Hamers, "Atomic-resolution surface spectroscopy with the scanning tunneling microscope," *Annual Review of Physical Chemistry*, vol. 40, no. 1, pp. 531–559, 1989.

[57] H. Hertz, "Ueber einen Einfluss des ultravioletten Lichtes auf die electrische Entladung," *Ann. Phys.*, vol. 267, pp. 983–1000, Jan. 1887.

[58] W. Hallwachs, "Ueber den Einfluss des Lichtes auf electrostatisch geladene Körper," *Ann. Phys.*, vol. 269, pp. 301–312, Jan. 1888.

[59] A. Einstein, "Über einen die Erzeugung und Verwandlung des Lichtes betreffenden heuristischen Gesichtspunkt," *Ann. Phys.*, vol. 322, pp. 132–148, Jan. 1905.

[60] S. Huefner, "Photoelectron spectroscopy," *Springer Verlag*, 2003.

[61] M. P. Seah and W. A. Dench, "Quantitative electron spectroscopy of surfaces: A standard data base for electron inelastic mean free paths in solids," *Surface and Interface Analysis*, vol. 1, no. 1, pp. 2–11, 1979.

[62] D. A. Shirley, "High-resolution X-ray photoemission spectrum of the valence bands of gold," *PRB*, vol. 5, pp. 4709–4714, June 1972.

[63] A. Damascelli, "Probing the electronic structure of complex systems by ARPES," *Physica Scripta*, vol. T109, p. 61, 2004.

[64] L. De Broglie, "Recherches sur la théorie des quanta," *Ann. Phys.*, vol. 10, no. 3, pp. 22–128, 1925.

[65] E. Bauer, "M. a. van hove, w. h. weinberg and c.-m. chan: Low-energy electron diffraction, experiment, theory, and surface structure determination, springer verlag, berlin, heidelberg, new york, london, paris, tokyo 1986. 603 seiten, preis: Dm 124,–," *Berichte der Bunsengesellschaft für physikalische Chemie*, vol. 91, pp. 1402–1402, Dec. 1987.

[66] L. H. Thomas, "The calculation of atomic fields," *Mathematical Proceedings of the Cambridge Philosophical Society*, vol. 23, no. 5, pp. 542–548, 1927.

[67] E. Fermi, "Eine statistische Methode zur Bestimmung einiger Eigenschaften des Atoms und ihre Anwendung auf die Theorie des periodischen Systems der Elemente," *Zeitschrift für Physik*, vol. 48, no. 1, pp. 73–79, 1928.

[68] P. Hohenberg and W. Kohn, "Inhomogeneous electron gas," *PR*, vol. 136, pp. B864–B871, Nov. 1964.

[69] W. Kohn and L. J. Sham, "Self-consistent equations including exchange and correlation effects," *PR*, vol. 140, pp. A1133–A1138, Nov. 1965.

[70] A. D. Becke, "Perspective: Fifty years of density-functional theory in chemical physics," *J. Chem. Phys.*, vol. 140, p. 18A301, Apr. 2014.

[71] J. P. Perdew, K. Burke, and M. Ernzerhof, "Generalized gradient approximation made simple," *PRL*, vol. 77, pp. 3865–3868, Oct. 1996.

[72] L. Moreschini, A. Bendounan, I. Gierz, C. R. Ast, H. Mirhosseini, H. Höchst, K. Kern, J. Henk, A. Ernst, S. Ostanin, F. Reinert, and M. Grioni, "Assessing the atomic contribution to the rashba spin-orbit splitting in surface alloys: Sb/Ag(111)," *Phys. Rev. B*, vol. 79, p. 075424, Feb 2009.

[73] I. Gierz, B. Stadtmüller, J. Vuorinen, M. Lindroos, F. Meier, J. H. Dil, K. Kern, and C. R. Ast, "Structural influence on the rashba-type spin splitting in surface alloys," *Phys. Rev. B*, vol. 81, p. 245430, Jun 2010.

[74] H. A. van der Vegt, H. M. van Pinxteren, M. Lohmeier, E. Vlieg, and J. M. C. Thornton, "Surfactant-induced layer-by-layer growth of Ag on Ag(111)," *PRL*, vol. 68, pp. 3335–3338, June 1992.

[75] S. Oppo, V. Fiorentini, and M. Scheffler, "Theory of adsorption and surfactant effect of Sb on Ag(111)," *Phys. Rev. Lett.*, vol. 71, pp. 2437–2440, Oct 1993.

[76] J. Vrijmoeth, H. A. van der Vegt, J. A. Meyer, E. Vlieg, and R. J. Behm, "Surfactant-induced layer-by-layer growth of Ag on Ag(111): Origins and side effects," *PRL*, vol. 72, pp. 3843–3846, June 1994.

[77] B. W. Batterman, "Effect of dynamical diffraction in X-ray fluorescence scattering," *PR*, vol. 133, pp. A759–A764, Feb. 1964.

[78] J. Zegenhagen, "X-ray standing waves technique: Fourier imaging active sites," *Japanese Journal of Applied Physics*, vol. 58, no. 11, p. 110502, 2019.

[79] E. A. Soares, C. Bittencourt, V. B. Nascimento, V. E. de Carvalho, C. M. C. de Castilho, C. F. McConville, A. V. de Carvalho, and D. P. Woodruff, "Structure determination of $Ag(111)(\sqrt{3} \times \sqrt{3})r30° -$ Sb by low-energy electron diffraction," *Phys. Rev. B*, vol. 61, pp. 13983–13987, May 2000.

[80] S. A. de Vries, W. J. Huisman, P. Goedtkindt, M. J. Zwanenburg, S. L. Bennett, I. K. Robinson, and E. Vlieg, "Surface atomic structure of the $(3 \times 3) - r30° -$ Sb reconstructions of Ag(111) and Cu(111)," *Surface Science*, vol. 414, no. 1, pp. 159–169, 1998.

[81] D. P. Woodruff, B. C. C. Cowie, and A. R. H. F. Ettema, "Surface structure determination using X-ray standing waves: a simple view," *Journal of Physics: Condensed Matter*, vol. 6, no. 49, pp. 10633–10645, 1994.

[82] P. Zhang, C. Ma, S. Sheng, H. Liu, J. Gao, Z. Liu, P. Cheng, B. Feng, L. Chen, and K. Wu, "Absence of topological β-antimonene and growth of α-antimonene on noble metal ag(111) and cu(111) surfaces," *PRMATERIALS*, vol. 6, p. 074002, July 2022.

[83] J. A. Meyer, H. A. van der Vegt, J. Vrijmoeth, E. Vlieg, and R. J. Behm, "Reversible place-exchange during film growth: a mechanism for surfactant transport," *Surface Science*, vol. 355, no. 1, pp. L375–L380, 1996.

[84] H. A. van der Vegt, J. Vrijmoeth, R. J. Behm, and E. Vlieg, "Sb-enhanced nucleation in the homoepitaxial growth of Ag(111)," *PRB*, vol. 57, pp. 4127–4131, Feb. 1998.

[85] P. D. Quinn, D. Brown, D. P. Woodruff, P. Bailey, and T. C. Q. Noakes, "Structural study of the adsorption of Sb on Ag(111) using medium energy ion scattering," *Surface Science*, vol. 511, pp. 43–56, June 2002.

[86] T. C. Q. Noakes, D. A. Hutt, and C. F. McConville, "Adsorption of Sb on Ag(111) studied using LEED, AES and XPS," *Surface Science*, vol. 307-309, pp. 101–106, Apr. 1994.

[87] T. C. Q. Noakes, D. A. Hutt, C. F. McConville, and D. P. Woodruff, "Structural investigation of ordered Sb adsorption phases on Ag(111) using coaxial impact collision ion scattering spectroscopy," *Surface Science*, vol. 372, pp. 117–131, Feb. 1997.

[88] S. A. de Vries, W. J. Huisman, P. Goedtkindt, M. J. Zwanenburg, S. L. Bennett, and E. Vlieg, "Floating stacking fault during homoepitaxial growth of Ag(111)," *PRL*, vol. 81, pp. 381–384, July 1998.

[89] D. P. Woodruff and J. Robinson, "Sb-induced surface stacking faults at Ag(111) and Cu(111) surfaces: density-functional theory results," *Journal of Physics: Condensed Matter*, vol. 12, no. 35, pp. 7699–7704, 2000.

[90] C. L. Littler and D. G. Seiler, "Temperature dependence of the energy gap of InSb using nonlinear optical techniques," *Appl. Phys. Lett.*, vol. 46, pp. 986–988, May 1985.

[91] A. Proessdorf, P. Rodenbach, F. Grosse, M. Hanke, W. Braun, H. Riechert, W. Hu, S. Fujikawa, M. Kozu, and M. Takahasi, "The physical origin of the InSb(111)A surface reconstruction transient," *Surface Science*, vol. 606, no. 17, pp. 1458–1461, 2012.

[92] F. Owman and P. Mårtensson, "STM study of the SiC(0001) $\sqrt{3} \times \sqrt{3}$ surface," *Surface Science*, vol. 330, no. 1, pp. L639–L645, 1995.

[93] M. Bauernfeind, J. Erhardt, P. Eck, P. K. Thakur, J. Gabel, T.-L. Lee, J. Schäfer, S. Moser, D. Di Sante, R. Claessen, and G. Sangiovanni, "Design and realization of topological dirac fermions on a triangular lattice," *Nature Communications*, vol. 12, no. 1, p. 5396, 2021.

[94] B. Liu, T. Wagner, S. Enzner, P. Eck, M. Kamp, G. Sangiovanni, and R. Claessen, "Moiré pattern formation in epitaxial growth on a covalent substrate: Sb on insb(111)a," *Nano Lett.*, vol. 23, pp. 3189–3195, Apr. 2023.

[95] J. Bohr, R. Feidenhans'l, M. Nielsen, M. Toney, R. L. Johnson, and I. K. Robinson, "Model-independent structure determination of the InSb(111) (2×2) surface with use of synchrotron X-ray diffraction," *PRL*, vol. 54, pp. 1275–1278, Mar. 1985.

[96] M. Volmer and A. Weber, "Keimbildung in übersättigten Gebilden," vol. 119U, no. 1, pp. 277–301, 1926.

[97] M. Nishizawa, T. Eguchi, T. Misima, J. Nakamura, and T. Osaka, "Structure of the InSb(111)A $- (2\sqrt{3} \times 2\sqrt{3}) - r30°$ surface and its dynamical formation processes," *PRB*, vol. 57, pp. 6317–6320, Mar. 1998.

[98] C. Zhang, C.-P. Chuu, X. Ren, M.-Y. Li, L.-J. Li, C. Jin, M.-Y. Chou, and C.-K. Shih, "Interlayer couplings, moiré patterns, and 2D electronic superlattices in MoS2/WSe2 hetero-bilayers," *Science Advances*, vol. 3, p. e1601459, Feb. 2017.

[99] K. Kim, A. DaSilva, S. Huang, B. Fallahazad, S. Larentis, T. Taniguchi, K. Watanabe, B. J. LeRoy, A. H. MacDonald, and E. Tutuc, "Tunable moiré bands and strong correlations in small-twist-angle bilayer graphene," *Proc Natl Acad Sci USA*, vol. 114, p. 3364, Mar. 2017.

[100] C. Liu, Y. Zhou, G. Wang, Y. Yin, C. Li, H. Huang, D. Guan, Y. Li, S. Wang, H. Zheng, C. Liu, Y. Han, J. W. Evans, F. Liu, and J. Jia, "Sierpiński structure and electronic topology in Bi thin films on InSb(111)B surfaces," *PRL*, vol. 126, p. 176102, Apr. 2021.

[101] O. U. Aktürk, V. O. Özçelik, and S. Ciraci, "Single-layer crystalline phases of antimony: Antimonenes," *PRB*, vol. 91, p. 235446, June 2015.

[102] G. Bian, X. Wang, Y. Liu, T. Miller, and T.-C. Chiang, "Interfacial protection of topological surface states in ultrathin Sb films," *Phys. Rev. Lett.*, vol. 108, p. 176401, Apr 2012.

[103] C. R. Ast and H. Höchst, "Fermi surface of Bi(111) measured by photoemission spectroscopy," *PRL*, vol. 87, p. 177602, Oct. 2001.

[104] K. Sugawara, T. Sato, S. Souma, T. Takahashi, M. Arai, and T. Sasaki, "Fermi surface and anisotropic spin-orbit coupling of Sb(111) studied by angle-resolved photoemission spectroscopy," *Phys. Rev. Lett.*, vol. 96, p. 046411, Feb 2006.

[105] J. Seo, P. Roushan, H. Beidenkopf, Y. S. Hor, R. J. Cava, and A. Yazdani, "Transmission of topological surface states through surface barriers," *Nature*, vol. 466, pp. 343–346, July 2010.

[106] C.-H. Hsu, Z.-Q. Huang, F.-C. Chuang, C.-C. Kuo, Y.-T. Liu, H. Lin, and A. Bansil, "The nontrivial electronic structure of Bi/Sb honeycombs on SiC(0001)," *New Journal of Physics*, vol. 17, no. 2, p. 025005, 2015.

[107] Y. Wang and V. H. Crespi, "Atlas of 2D metals epitaxial to SiC: filling-controlled gapping conditions and alloying rules." arXiv, 2011.01914, https://arxiv.org/abs/2011.01914, 2020.

[108] T. Seyller, "Electronic properties of Sic surfaces and interfaces: some fundamental and technological aspects," *Applied Physics A*, vol. 85, no. 4, pp. 371–385, 2006.

[109] J. Ji, X. Song, J. Liu, Z. Yan, C. Huo, S. Zhang, M. Su, L. Liao, W. Wang, Z. Ni, Y. Hao, and H. Zeng, "Two-dimensional antimonene single crystals grown by van der Waals epitaxy," *Nature Communications*, vol. 7, p. 13352, Nov. 2016.

[110] S. Glass, F. Reis, M. Bauernfeind, J. Aulbach, M. R. Scholz, F. Adler, L. Dudy, G. Li, R. Claessen, and J. Schäfer, "Atomic-scale mapping of layer-by-layer hydrogen etching and passivation of SiC(0001) substrates," *The Journal of Physical Chemistry C*, vol. 120, no. 19, pp. 10361–10367, 2016.

[111] N. Sieber, T. Seyller, L. Ley, D. James, J. D. Riley, R. C. G. Leckey, and M. Polcik, "Synchrotron X-ray photoelectron spectroscopy study of hydrogen-terminated $6H-$ $SiC0001$ surfaces," *PRB*, vol. 67, p. 205304, May 2003.

[112] J. Erhardt, M. Bauernfeind, P. Eck, M. Kamp, J. Gabel, T.-L. Lee, G. Sangiovanni, S. Moser, and R. Claessen, "Indium epitaxy on SiC(0001): A roadmap to large scale growth of the quantum spin hall insulator indenene," *J. Phys. Chem. C*, vol. 126, pp. 16289–16296, Sept. 2022.

[113] J. Heyd, G. E. Scuseria, and M. Ernzerhof, "Hybrid functionals based on a screened Coulomb potential," *J. Chem. Phys.*, vol. 118, pp. 8207–8215, Apr. 2003.

[114] K. Iyakutti, E. M. Kumar, I. Lakshmi, R. Thapa, R. Rajeswarapalanichamy, V. J. Surya, and Y. Kawazoe, "Effect of surface doping on the band structure of graphene: a DFT study," *Journal of Materials Science: Materials in Electronics*, vol. 27, no. 3, pp. 2728–2740, 2016.

[115] J. A. Stroscio, R. M. Feenstra, and A. P. Fein, "Electronic structure of the Si(111) 2×1 surface by scanning-tunneling microscopy," *PRL*, vol. 57, pp. 2579–2582, Nov. 1986.

[116] R. M. Feenstra, J. A. Stroscio, and A. P. Fein, "Tunneling spectroscopy of the Si(111) (2×1) surface," *Surface Science*, vol. 181, no. 1, pp. 295–306, 1987.

[117] S. Glass, G. Li, F. Adler, J. Aulbach, A. Fleszar, R. Thomale, W. Hanke, R. Claessen, and J. Schäfer, "Triangular spin-orbit-coupled lattice with strong coulomb correlations: Sn atoms on a SiC(0001) substrate," *Phys. Rev. Lett.*, vol. 114, p. 247602, Jun 2015.

[118] S. Yi, H. Lee, J.-H. Choi, and J.-H. Cho, "Nature of the insulating ground state of the two-dimensional Sn atom lattice on SiC(0001)," *Scientific Reports*, vol. 6, no. 1, p. 30598, 2016.

[119] B. Liu, L. Huang, Q. Zhu, F. Qin, and D. Wang, "Chemical and electronic passivation of $4H-SiC$ surface by hydrogen-nitrogen mixed plasma," *Appl. Phys. Lett.*, vol. 104, p. 202101, May 2014.

[120] S. Kumar, D. M. Phase, S. Porwal, and T. K. Sharma, "Surface photovoltage and photoelectron spectra of GaP," *Solid State Communications*, vol. 141, no. 5, pp. 284–287, 2007.

[121] R. Weihrich, I. Anusca, and M. Zabel, "Halbantiperowskite: Zur Struktur der Shandite M3/2AS (M = Co, Ni; A = In, Sn) und ihren Typ-Antitypbeziehungen," *Z. anorg. allg. Chem.*, vol. 631, pp. 1463–1470, June 2005.

[122] T. Björkman, V. Skakalova, S. Kurasch, U. Kaiser, J. C. Meyer, J. H. Smet, and A. V. Krasheninnikov, "Vibrational properties of a two-dimensional silica kagome lattice," *ACS Nano*, vol. 10, pp. 10929–10935, Dec. 2016.

[123] L. Zhi, Z. Jincheng, W. Li, F. Haifeng, G. Qian, X. Xun, H. Weichang, W. Xiaolin, Z. Chao, W. Kehui, D. S. Xue, C. Lan, H. Zhenpeng, and D. Yi, "Realization of flat band with possible nontrivial topology in electronic kagome lattice," *Science Advances*, vol. 4, p. eaau4511, June 2018.

[124] C. Wagner and K. Grünewald, "Beitrag zur theorie des anlauf vorganges. III," *Zeitschrift für Physikalische Chemie*, vol. 40B, no. 1, pp. 455–475, 1938.

[125] N. Cabrera and N. F. Mott, "Theory of the oxidation of metals," *Reports on Progress in Physics*, vol. 12, no. 1, pp. 163–184, 1949.

[126] F. P. Fehlner and N. F. Mott, "Low-temperature oxidation," *Oxidation of Metals*, vol. 2, no. 1, pp. 59–99, 1970.

[127] M. Martin and E. Fromm, "Low-temperature oxidation of metal surfaces," *Journal of Alloys and Compounds*, vol. 258, no. 1, pp. 7–16, 1997.

[128] A. Castellanos-Gomez, L. Vicarelli, E. Prada, J. O. Island, K. L. Narasimha-Acharya, S. I. Blanter, D. J. Groenendijk, M. Buscema, G. A. Steele, J. V. Alvarez, H. W. Zandbergen, J. J. Palacios, and H. S. J. van der Zant, "Isolation and characterization of few-layer black phosphorus," *2D Materials*, vol. 1, no. 2, p. 025001, 2014.

[129] A. E. Naclerio, D. N. Zakharov, J. Kumar, B. Rogers, C. L. Pint, M. Shrivastava, and P. R. Kidambi, "Visualizing oxidation mechanisms in few-layered black phosphorus via in situ transmission electron microscopy," *ACS Appl. Mater. Interfaces*, vol. 12, pp. 15844–15854, Apr. 2020.

[130] J. Gao, B. Li, J. Tan, P. Chow, T.-M. Lu, and N. Koratkar, "Aging of transition metal dichalcogenide monolayers," *ACS Nano*, vol. 10, pp. 2628–2635, Feb. 2016.

[131] Q. Chen, Y. Zhong, Z. Zhang, X. Zhao, M. Huang, Z. Zhen, Y. He, and H. Zhu, "Long-term electrical conductivity stability of graphene under uncontrolled ambient conditions," *Carbon*, vol. 133, pp. 410–415, 2018.

[132] L. H. Li, J. Cervenka, K. Watanabe, T. Taniguchi, and Y. Chen, "Strong oxidation resistance of atomically thin boron nitride nanosheets," *ACS Nano*, vol. 8, pp. 1457–1462, Feb. 2014.

[133] "Specslab prodigy v4.67.1-r91102." SPECS Surface Nano Analysis GmbH, https://www.specs-group.com/nc/specs/products/detail/prodigy/, Apr. 2020.

[134] J. C. Fuggle and N. Mårtensson, "Core-level binding energies in metals," *Journal of Electron Spectroscopy and Related Phenomena*, vol. 21, no. 3, pp. 275–281, 1980.

[135] "Nist x-ray photoelectron spectroscopy database." NIST Standard Reference Database Number 20, National Institute of Standards and Technology, Gaithersburg MD, 2000 (retrieved august 2022).

[136] F. Amy, Y. Hwu, C. Brylinski, and P. Soukiassian, "Room temperature initial oxidation of 6H- and $4\mathrm{H} - \mathrm{SiC}(0001)3 \times 3$," *Materials Science Forum*, vol. 353-356, pp. 215–218, 2001.

[137] S. Doniach and M. Sunjic, "Many-electron singularity in X-ray photoemission and X-ray line spectra from metals," *Journal of Physics C: Solid State Physics*, vol. 3, no. 2, pp. 285–291, 1970.

[138] D. G. Bills and N. P. Carleton, "Adsorption of activated gases," *Journal of Applied Physics*, vol. 29, pp. 692–697, Apr. 1958.

[139] A. Krönig, "GrundzügeeinerTheoriederGase," *Ann. Phys.*, vol. 175, pp. 315–322, Jan. 1856.

[140] P. Kisliuk, "The sticking probabilities of gases chemisorbed on the surfaces of solids," *Journal of Physics and Chemistry of Solids*, vol. 3, no. 1, pp. 95–101, 1957.

[141] P. Sen, M. S. Hegde, and C. N. R. Rao, "Surface oxidation of cadmium, indium, tin and antimony by photoelectron and Auger spectroscopy," *Applications of Surface Science*, vol. 10, no. 1, pp. 63–74, 1982.

[142] R. B. dos Santos, R. Rivelino, G. K. Gueorguiev, and A. Kakanakova-Georgieva, "Exploring 2D structures of indium oxide of different stoichiometry," *CrystEngComm*, vol. 23, no. 38, pp. 6661–6667, 2021.

[143] F. Reis, "Realization and spectroscopy of the quantum spin hall insulator bismuthene on silicon carbide," phd thesis, Julius-Maximilians-Universität Würzburg, Mar. 2022.

[144] W. R. Dunstan, H. A. D. Jowett, and E. Goulding, "CLIII.–the rusting of iron," *J. Chem. Soc., Trans.*, vol. 87, no. 0, pp. 1548–1574, 1905.

[145] J. Weis, "Photoelectron spectroscopy studies on the wide-gap two-dimensional topological insulator bismuthene on $4\mathrm{H} - \mathrm{SiC}(0001)$ & perylene as a removable organic capping," master thesis, Julius-Maximilians-Universität Würzburg, Aug. 2019.

[146] J. Wittemann, "Growth and encapsulation of bismuthene for nanodevices," master thesis, Julius-Maximilians-Universität Würzburg, Mar. 2022.

[147] G. Zhang, H. Wu, L. Zhang, L. Yang, Y. Xie, F. Guo, H. Li, B. Tao, G. Wang, W. Zhang, and H. Chang, "Two-dimensional van der Waals topological materials: Preparation, properties, and device applications," *Small*, vol. n/a, p. 2204380, Sept. 2022.